2012

Nanostructured Columnar Thin Films Using Oblique Angle Deposition: Growth, SERS Characterization and Lithographic Processing

Piyush J. Shah
Wright State University

NANOSTRUCTURED COLUMNAR THIN FILMS USING OBLIQUE ANGLE DEPOSITION: GROWTH, SERS CHARACTERIZATION AND LITHOGRAPHIC PROCESSING

A dissertation submitted in partial fulfillment of the
requirements for the degree of
Doctor of Philosophy

By
Piyush J. Shah
M.S., Wright State University, 2005

2012

Wright State University

WRIGHT STATE UNIVERSITY

SCHOOL OF GRADUATE STUDIES

May 30, 2012

I HEREBY RECOMMEND THAT THE DISSERTATION PREPARED UNDER MY SUPERVISION BY Piyush Jayant Shah ENTITLED Nanostructured Columnar Thin Films using Oblique Angle Deposition: Growth, SERS Characterization and Lithographic Processing BE ACCEPTED IN PARTIAL FULFILLMENT OF THE REQUIREMENTS FOR THE DEGREE OF Doctor of Philosophy.

_____
Kefu Xue, Ph.D.
Dissertation Director

_____
Ramana V. Grandhi, Ph.D.
Director, Ph.D. in Engineering Program

_____
Andrew Hsu, Ph.D.
Dean, School of Graduate Studies

Committee on Final Examination

_____
Kefu Xue, Ph.D.

_____
Andrew M. Sarangan, Ph.D.

_____
Saiyu Ren, Ph.D.

_____
Yan Zhuang, Ph.D.

_____
Ronald A. Coutu, Ph.

Abstract

Shah, Piyush Jayant. Ph.D; Engineering Ph.D. Program
Wright State University, 2012. Nanostructured Columnar Thin Films using Oblique Angle Deposition: Growth, SERS Characterization and Lithographic processing

Oblique angle physical vapor deposition technique has led to the evolution of new class of nanostructured thin films. These films posses' novel anisotropic electrical, magnetic, optical, properties which could be potentially engineered based on the growth conditions and the deposition parameters. The technique is based on the atomistic level self-shadowing principle. In the oblique angle deposition (OAD) technique, the substrate is held at an oblique angle with respect to the incoming vapor flux. As the vapor atoms condense and nucleate on the substrate, the shadowed regions behind each site stop receiving the subsequent vapor atoms. Instead, they land on the previously formed droplets, resulting in the evolution of a columnar morphology.

In this dissertation research, three aspects of nanostructured thin films grown using this method are investigated. When grown at room temperatures, soft metals such as silver (Ag), copper (Cu), gold (Au) etc; generally produce low aspect ratio collapsed columnar structures compared to high melting temperature metals such as titanium (Ti), chromium (Cr), nickel (Ni), etc. Using e-beam evaporation and a custom built cryogenic substrate cooling apparatus; we investigate the growth of nanostructured thin films made from soft metals at near 100 K and 300 K side-by-side. Growth of these films at cryogenic substrate temperatures has resulted in high aspect ratio nanocolumns thin film morphology.

Ag nanorods (AgNRs) thin films are known to have surface enhanced Raman scattering (SERS) response. In this study, AgNRs thin films are incubated in liquid and vapor phase with SERS test probe molecules. The SERS response of AgNRs thin films grown at room and cryogenic substrate temperature is compared. The hypothesized improved SERS response of cryogenically grown AgNRs is attributed to the morphological differences and higher surface of AgNRs at this growth conditions. Rigorous SERS enhancement factor (SEF) calculations are discussed by estimating the number of molecules absorbed on the surface of AgNRs through the use of fluorescence spectrophotometer measurements.

The third aspect of this research is to investigate the effect of liquids exposure and lithographic processing of these films. It is known that exposure of nanorods thin films to liquids and solvents, permanently changes the physical structure of these films. This prevents conventional lithographic patterning of such thin films since it involves wet processing. In this study, we show the use of CO_2 based critical point drying (CPD) technique to mitigate the structural collapse of nanorods thin films after liquids exposure. Further, we discuss dry lift-off based lithographic process to pattern these thin films.

Table of Contents

List of Figures

List of Tables

Acknowledgements

First, I would like to specially thank my academic advisor Dr. Kefu Xue for his academic guidance and support during all these years of my Masters and Ph. D. program. His openness for collaboration outside Wright State and letting me pursue and utilize the right research resources was instrumental for my ability to pursue this research at University of Dayton under the guidance of Dr. Andrew M. Sarangan in his Nano-Fabrication Laboratory. Getting to know Dr. Sarangan and working with him for this research was an unforgettable experience that I will cherish for life. I enjoyed all the freedom as I was growing as researcher and this was solely possible due to Dr. Sarangan's openness to explore things. This is evident from that the fact that something which started as a class project in his course on Nano-Fabrication has resulted into a Ph.D research subject for my dissertation. He is by far the best teacher I ever had throughout my graduate school experience and I was fortunate to have him guide through my Ph.D. research. His suggestions and encouragement has helped me during this research and even writing this dissertation. Not only did I learn the technical aspects of academic research, but working with him in the lab with different equipment for various issues also broadened my insights and hands on skills which are never taught in schools anywhere.

I would also like to thank Dr. Ioana Pavel and Adam Stahler at Wright State University for all your guidance and support for measurements using the Raman tool. Without your help, I couldn't have pursued the SERS portion of this research. It has been a pleasure to work with my Nano-Fab peers on research and lab related efforts. I am especially grateful to Xiaoxu Niu, Zhi Wu, and Alex Watson for their academic

advice and friendship. I would like to thank my committee members Dr. Yan Zhuang, Dr. Saiyu Ren and Dr. Ron Coutu for taking the time to serve on my committee and for offering constructive criticism. I would also like to thank Dr.LaVern Starman for helpful advice during the early stages when I joined the Ph.D. program.

Also, very special thanks to my wife for her patient love and support during my good days and encouragement through my bad ones. Finally, I would like to thank our parents and families for their love and continuous support during all these years.

Chapter 1 Introduction

Structured thin films (STF) or nanorods thin films with engineered microstructure is grown using OAD or glancing angle deposition (GLAD) technique [1 - 5]. Earlier in 1950, Konig and Helwig recognized the role of atomistic level self-shadowing principle for the formation of micro columnar structure using physical vapor deposition (PVD) methods [6]. The PVD methods that have been successfully applied to this technique include sputtering [7, 8], laser ablation [9], e-beam [10, 11] and thermal evaporation [12] however e-beam evaporation is the most commonly used method. Unlike in normal incidence thin film deposition, in this technique, the substrate is held at an oblique angle with respect to the vapor source. When the incoming vapor flux condenses and nucleates on the substrate, the sites in the shadow of the nuclei stops receiving new incoming flux. Eventually as the thickness of the deposited film increases, majority of the flux lands on the nucleus (minimal or no flux lands in the shadow of nuclei) and the columnar structured thin film morphology evolves.

Figure 1 shows the schematic and SEM results showing the difference in the morphology of thin films grown using normal incidence and oblique incidence deposition technique.

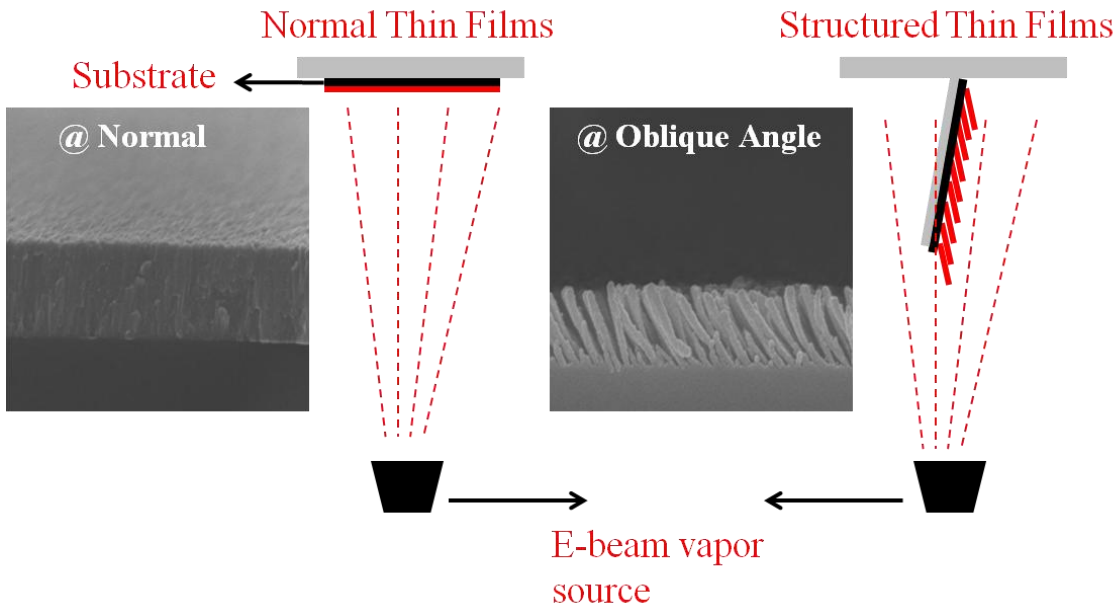

Figure 1 Schematic and SEM images showing the difference between normal incidence thin film and OAD thin film deposition techniques

The evolution of this film is based on the random initial nucleation during the early stages of film growth since the process of nucleation of atoms on the substrate is an uncontrolled random stochastic process. OAD technique has even been applied to pre-patterned substrates with so called "seeds" made from polymer, metal etc. The seeds are lithographically patterned on the substrates [3, 5, 13 - 18]. The spatial distribution, height, periodicity of these seeds, and the deposition oblique angle can be engineered to result in the columnar structure growth only on the pre-patterned seeds. This is referred as the periodic nucleation.

Figure 2 shows SEM images of SiO_2 STF grown based on random and periodic nucleation. Periodic 1-D grating structure was lithographically pre-patterned using interference lithography technique [21] prior to OAD.

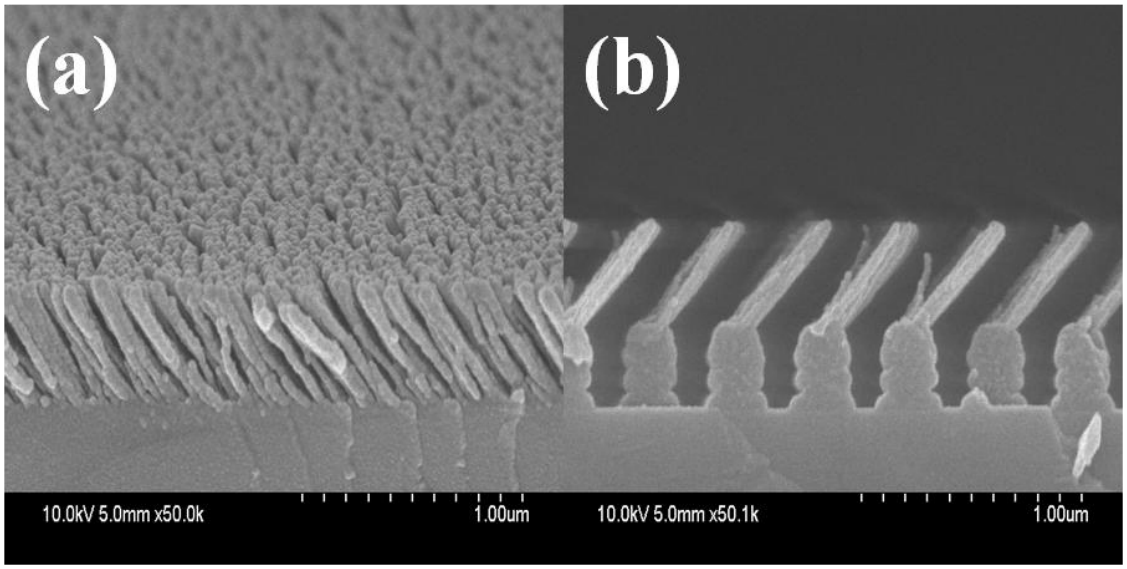

Figure 2 SEM images showing SiO_2 STF grown using OAD based on (a) random nucleation (b) periodic nucleation.

In addition to the substrate being held at an oblique angle, simultaneous periodic or continuous slow rotation of the substrate leads to the growth of various novel morphologies including vertical rods, coils, helices, zig-zag structures etc. Figure 3 shows the schematic representing growth of nanostructured thin films using this technique. Brett et. al. provides a comprehensive review on the state of the art in thin films grown using this technique, its properties, and their potential applications [3, 5].

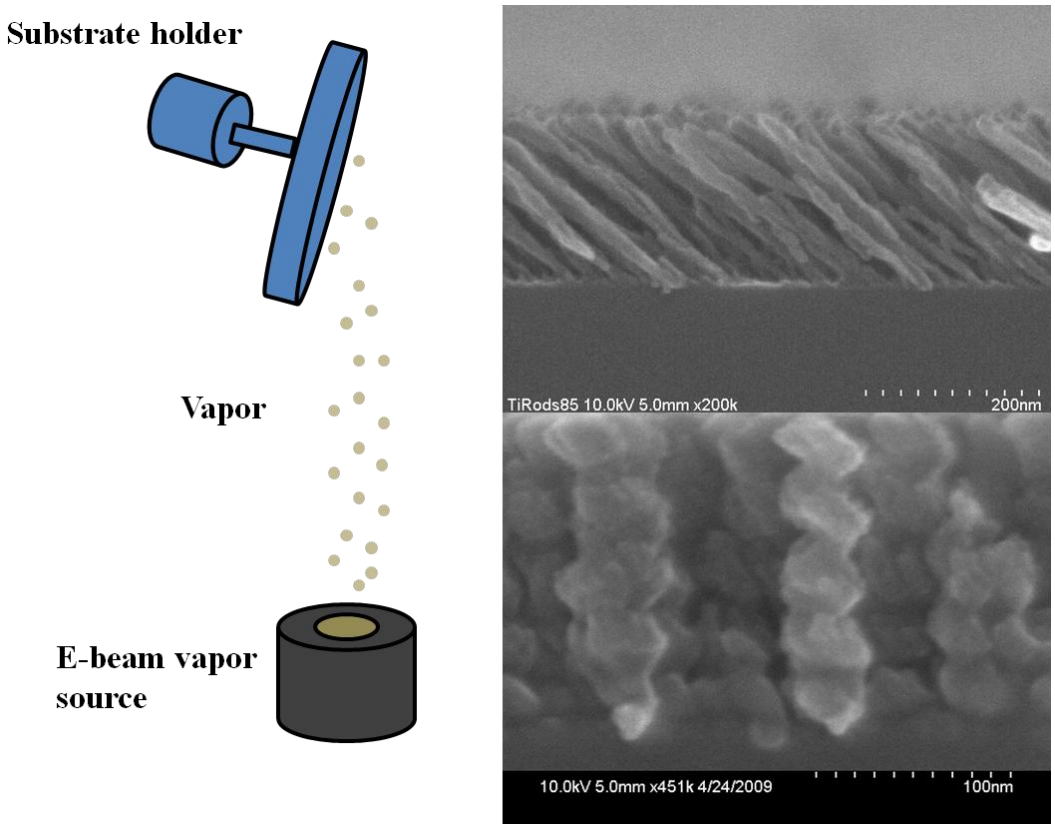

Figure 3 Schematic showing GLAD scheme and resultant difference in morphology of thin films (a) tilted nanorods (b) spiral nanorods

1.1 Dissertation research

In this dissertation research, three aspects of nanorods thin films are investigated. These are growth, surface enhanced Raman scattering (SERS) characterization and lithographic processing of these films.

1.1.1 Growth

Even OAD has been demonstrated by us and others to work very well in high melting temperature metals like Ti, Cr, Ni etc; it has had limited success with soft metals like Ag, Au, and Cu. The latter metals generally exhibit larger diameter rods and significantly smaller aspect ratios, and in many cases result in diffused and collapsed rods [22 - 25]. Former metals generally show distinctly separate, high aspect ratio columnar morphology [10, 11]. Based on the structure zone model (SZM) theory discussed by Movchan and Demchishin in 1969, the ratio of substrate temperature to the melting temperature of material deposited has an influence on the surface mobility of atoms on the substrate surface [26 - 29]. Based on this theory (details discussed in Chapter 2), we hypothesize that the growth of STF at cryogenic substrate temperature will influence the nano-columnar morphology of high conductivity, low melting temperature soft metals. In this dissertation research, we cryogenically cooled the substrate during the growth phase and examined its influence on the film structure. All the films were grown on crystalline silicon (Si) substrates, where the surface mobility is high and generally more difficult to grow OAD films. Our results indicate the formation of distinctly separate, high aspect ratio, individual nanorods thin films which are in contrast to the low aspect ratio and collapsed physical structure of nanorods thin films grown at room temperature. The difference in morphology of these films is attributed to the reduction in surface mobility

of the incident atoms on the substrate surface. This theory and hypotheses was verified by studying the early nucleation stage of thin films growth process. Chapter 2 provides further details on the motivation, experimental methods, results and discussion of this study.

This study has led to be the following journal and conference publications –

Piyush J. Shah, Xiaoxu Niu, Andrew M. Sarangan, "Effect of substrate temperature on the growth of silver nanorod thin films using oblique angle deposition" *(under review), Journal of Vacuum Science & Technology B, March 2012*

Andrew M. Sarangan Piyush J. Shah, Xiaoxu Niu, "Effect of cryogenic substrate temperature on the growth of Ag and Cu nanostructured optical metamaterials" *Symposium of Photonics and Optoelectronics 2012, China, May 2012*

1.1.2 SERS characterization

Ag nanostructured thin films grown using OAD are known to have surface enhanced Raman scattering (SERS) response [22, 23, 30 – 40]. In fact, most prior literature on Ag STF has been published for its SERS response and optical properties. Based on the observed morphological differences in the physical nanostructure of AgNRs grown at 100 K versus 300 K, we hypothesized that the SERS signal intensity of 100 K grown AgNRs would be stronger than in 300 K grown AgNRs. This hypothesis was based on the observed differences among the two thin films in spatial distribution of nanorods, increase in estimated nanostructured surface area and the number of Ag nanorods per μm^2. In this study we characterize and compare the SERS response of 100 K and 300 K grown AgNRs. Varying concentrations (10^{-6} M, 10^{-7} M, and 10^{-8} M) of Rhodamine 6G (R6G) molecules in aqueous solution was used as the SERS test probe. Due to the increased surface area and distinctly improved morphology of AgNRs grown at 100 K, we find an average of 91 %, 445 % and 441 % increase in the SERS signal intensity from these films. A method for extensive SERS EF calculations is discussed by experimentally estimating the number molecules absorbed on the surface of AgNRs using fluorescence spectrophotometer measurements. Results discussed here also indicate the level of uniformity and reproducibility of these SERS substrates. This is an important attribute required for any new SERS substrates.

Furthermore, these AgNRs were also characterized for its effectiveness in SERS based chemical vapor sensing application. The results indicate increased SERS signal intensity for 100 K AgNRs compared to 300 K grown. Increase in SERS signal intensity implies the potential for these substrates to detect the presence of analyte molecules in

vapor pahse at ultra low concentrations. This study shows the effectiveness and versatility of 100 K grown AgNRs based SERS substrates for liquid and gas phase sensing applications. Chapter 3 provides further details on motivation, experimental methods, results and discussion of this study.

This study has led to be the following journal and conference publications –

Piyush J. Shah, Adam Stahler, Andrew M. Sarangan, Ioana Pavel, "Comparative SERS response of silver nanorods thin films fabricated at room and cryogenic temperature with Rhodamine 6G molecules" *(to be submitted) Journal of American Chemical Society Communications, May 2012*

Andrew M. Sarangan Piyush J. Shah, Xiaoxu Niu, Dongquan Ju, "Vapor phase sensing using metal nanorods thin films grown using oblique angle deposition" *IEEE Nano 2012, UK, August 2012*

1.1.3 Lithographic processing

The high surface area of STF provides a conducive platform for chemical, biological and environmental sensing applications including electrodes for fuel cells [45 – 48]. It has, however, been noted that these films, especially high aspect ratio nanocolumns are easily deformed after exposure to liquids or moist environments [48 - 52]. This is due to the high capillary forces acting between neighboring nanocolumns which collapse the structures during the drying process. The capillary pressure acting on the nanorods depends on the surface tension of the fluid and the spacing between the nanorods. However, wet processing is an inevitable step in most lithographic patterning. If STF are to be successfully used in practical devices, techniques need to be developed to allow them to withstand wet processes.

In this study, we investigated SiO_2 tilted nanorods thin films in two different solvents (ethanol and acetone) for comparing the effect of evaporative room temperature drying and CO_2 CPD. Acetone is a common chemical solvent used in photolithography to strip photo resist and also for lift-off processes. Ethanol is another common cleaning solvent and transitional fluids used in critical point dryers. Hence these were chosen as representatives for our study. The results of our study indicate that CO_2 CPD can be used to prevent these thin films from permanent collapse after exposure to liquids. Alternatively, also shown is a dry lift-off based lithographic technique where the nanorods thin films exposure to liquids is prevented using pre-patterned polymer layer which is subsequently mechanically peeled-off from the substrate after film deposition. Chapter 4 further provides the details on motivation, experimental methods, results and discussion of this study.

This study has led to be the following journal and conference publications –

Piyush J. Shah, Zhi Wu, Andrew M. Sarangan, "Effect of CO2 critical point drying on nanostructured thin films after liquids exposure" *(accepted) Thin Solid Films, Nov 2011*

Piyush J. Shah, Howard Knachel, Andrew M. Sarangan, "Lithographic Processing of Nanostructured Thin Films Grown using Oblique Angle Deposition Technique" *International AVS Symposium, USA, 2011*

1.2 Dissertation contributions

- Demonstrated the growth of nanorods thin films made from low melting temperature soft metals such as Ag, Cu and Au on crystalline substrates. The results have led to the growth of high aspect ratio nanorods thin films with columnar morphology which has never been shown before [53, 54]. (Chapter 2)
- Verified our proposed theory on the evolution of these metal nanorods thin films by studying the early nucleation stage of thin films growth by terminating the growth at 100 Å and 300 Å [53, 54]. (Chapter 2)
- Explained the surface adsorption behavior of high and low melting temperature metal atoms and how it affects the columnar morphology formation [53, 54]. (Chapter 2)
- Demonstrated the Surface enhanced Raman scattering (SERS) characterization of 100 K and 300 K grown Ag nanorods thin films for chemical sensing in liquids. Results indicate 100 K grown Ag nanorods thin films as significantly effective and ultra sensitive SERS substrate over 300 K grown Ag nanorods thin films for chemical sensing applications [55, 56]. (Chapter 3)
- Post analyte incubation effects on the Ag nanorods thin films has been studied for the first time which explains the increase in SERS signal intensity in 100 K versus 300 K grown nanorods thin films [55, 56]. (Chapter 3)
- Rigorous enhancement factor calculations are reported based on the first use of fluorescence spectrophotometer measurements to estimate the number of molecules adsorbed on the surface of Ag nanorods thin films. Unlike assuming molecular coverage (monolayer or sub monolayer) in estimation of enhancement

factors, we believe using fluorescence measurements to determine the molecular coverage will result in more accurate enhancement factor estimation [55, 56]. (Chapter 3)

- Demonstrated the first use of nanorods thin films as an effective SERS substrate for chemical vapor sensing [55, 56]. (Chapter 4)
- Demonstrated the first use of CO_2 based critical point drying technique as an effective method to preserve the physical structure and morphology of nanorods thin films after liquids exposure. This result is significant because, preserving the physical structure of nanorods thin films after liquids exposure enables the use of conventional lithographic techniques for patterning nanorods thin films [57]. (Chapter 5)
- Lithographic patterning of nanorods thin films has been demonstrated for the first time using dry lift-off technique. (Chapter 6)

Chapter 2 Growth

2.1 Introduction

High electrical conductivity, soft metals such as Ag, Au and Cu have shown the potential for use in plasmonic and optical metamaterials research. Also Ag nanostructured thin films have been studied extensively for chemical and biological sensing applications using SERS, surface enhanced vibrational spectroscopy (SEVS) and surface enhanced infrared absorbance (SERIA) [22, 23, 31, 40]. The nanometer scale spatial arrangement of the metallic nanostructures has a strong influence on the plasmonic and other optical properties. Therefore a reliable, low-cost and scalable fabrication technique to achieve metallic nanostructures is highly desirable [23].

Over the years, OAD technique has evolved as an inexpensive and scalable method for the growth of nanostructured columnar thin films. Unlike in normal incidence physical vapor deposition of thin films, in this technique the substrate is held at an oblique angle with respect to the evaporating vapor source. As the vapor atoms condense and nucleate on the substrate, the shadowed regions behind each nucleating site stop receiving the subsequent vapor atoms. Instead, they land on the previously formed

droplets, resulting in the evolution of a columnar morphology. The atoms on the substrate provide geometrical shadowing which prevents newly arriving atoms to land in the shadowed areas. Atomistic level self shadowing phenomenon leads to the growth of nanorods columns in the direction of vapor source. The factor that influences the columnar morphology includes the oblique angle of the substrate, substrate temperature, deposition rate etc. These factors have a strong influence on the shape and arrangement of the columnar thin films. A comprehensive review of these thin films, their properties, and potential applications is discussed by Brett group [3, 5]. Even though OAD has shown to work very well with high melting temperature metals like Ti, Cr, Ni etc., it has had limited success with soft metals like Ag, Au and Cu. These softer metals generally exhibit larger diameter rods and significantly smaller aspect ratios, and in many cases result in collapsed rods [22 – 25]. Despite the collapsed nanorods structure, prior literature published on this subject claim to have successfully demonstrated the growth columnar morphology thin films from these soft metals [22 - 25]. In reality, the aspect ratios of the individual nanocolumns made from soft metals is lower by at least a factor of 3 or more compared to the aspect ratios of nanorods thin films grown from high melting temperature metals.

Figure 4 shows the comparison of physical morphology of nanorods thin films grown using Ti, Ni, Cr, SiO_2 (high melting temperature) versus Ag and Cu (low melting temperature).

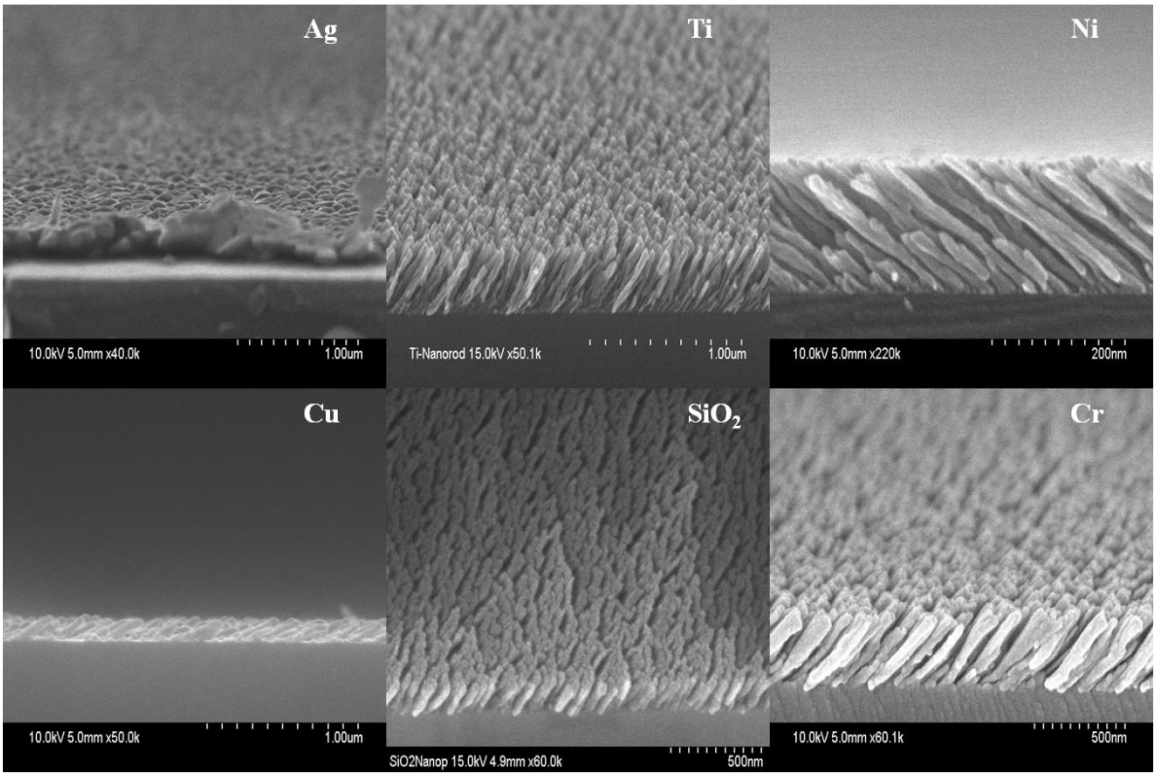

Figure 4 Comparative SEM results showing the physical morphology of nanorods thin films deposited using low and high melting materials. Figure shows near collapsed or small aspect ratio nanocolumns grown from Ag and Cu versus distinctly separate, high aspect ratio nanorods thin films from Ti, Ni, SiO_2 and Cr

Substrate temperature and surface diffusion play an important role in the formation of columnar structured thin films [58 – 62]. The structure zone model (SZM) developed by Movchan and Demchishin in 1969 uses the ratio of substrate temperature to the melting temperature of the element (T_s/T_m) to identify three distinct growth zones: zone I, zone II and zone III. The effect of thin film morphology was studied on the substrate with different three growth zones viz. Zone I, Zone II and Zone III [26, 27, 63]. The result of the study led to the following three observations:

Zone I – The film morphology appeared porous with tapered columns with overall rough film surface due to relatively low surface diffusion of atoms.

Zone II – Here the substrate temperature was higher than in Zone I which leads to higher surface diffusion and mobility. As a result, the film morphology is relatively smooth and flat than in Zone I.

Zone III – The substrate temperature was highest compared to Zone I and II, which led to bulk diffusion being dominant and leads to film morphology which is smooth and bright.

Based on these results, it implies that the surface diffusion limited Zone I with T_s/T_m smaller than 0.3 is most conducive for the formation of nanorods thin films [26, 62, 63].

Table 1 shows the T_s/T_m ratios for several common metals. Metals with low melting temperatures such as Ag, Au and Cu etc. have higher T_s/T_m ratios compared to Ti, Ni, Cr, etc.

Element	T_m (K)	T_s/T_m
Al	933	0.319
Ag	1235	0.241
Au	1337	0.222
Cu	1356	0.219
Ni	1726	0.172
Co	1768	0.168
Ti	1933	0.154
Cr	2130	0.139

T_s = 298K

Table 1 Melting temperature of metals and respective substrate temperature (T_s) to melting temperature (T_m) ratio. T_s = 298 K

Using OAD technique, the growth of nanorods thin films made from several metals and metal oxides was studied by Deniz et. al. They found that the elements with melting temperatures lower than 933 K (which corresponds to the melting temperature of aluminum) failed to evolve into columnar morphology [61]. However these conclusions were based on the analysis of average grain sizes using top-view scanning electron images of normal incidence thin films grown from these materials. Besides SZM model by Movchan and Demchishin, this study is another example which relates the melting

temperature of the element and the materials ability to form columnar morphology thin films.

Another important aspect is the choice of substrate on which the columnar thin films are grown. Most prior literature on Ag films grown using OAD at room temperature were deposited on non-crystalline substrates, where the surface mobility is significantly smaller compared to crystalline substrates [59]. Knowing the Arrhenius type temperature dependent surface diffusion behavior of atoms, these prior results clearly provide the motivation for growing soft and low melting temperature metal nanorods thin films on a cold substrate. At a low enough substrate temperature, the surface mobility and the ratio T_s/T_m can be significantly lowered. In this study, the substrate is cooled using liquid nitrogen during the deposition and the influence of temperature on the evolution and morphology of columnar thin films is examined. The films were grown on crystalline silicon substrates, where the surface mobility is high and generally more difficult to grow Ag nanorods thin films. The most commonly used substrate for semiconductor and device applications is crystalline silicon and also for making test coupons of thin film samples. The ability to grow them on silicon is important for these nanocolumns integration with useful devices. Few early reports have been published on the influence of substrate temperature for the growth of Fe and Co thin films; however the objective of these papers were to investigate the temperature influence on the magnetic and reflective properties of these thin films [4, 44, 64]. The study discussed in this chapter is one of the first investigation on growing OAD films from soft metals at cryogenic substrate temperatures for truly studying the growth behavior and how metal nanorods films evolves with temperature. To understand and observe the actual morphology of these

films, it is important to analyze the films with cross-section SEM images. This analysis quantifies the aspect ratio of these thin films. Top view images alone, as used in earlier studies, presents an exaggerated view of the film morphology and lead to claims of distinct nanocolumns formation even when the columns are only partially developed or collapsed. Table 2 shows a comparative study of previously reported Ag nanorods thin films grown using OAD technique. As shown in the table, only few previously published papers report the side view SEM images which are revealing of the physical structure of the thin film.

Substrate	Barrier layer thickness (nm)	SEM (Top, Side)	Year	Ref.
Glass slide	-	Top	2006	[101]
Fused Silica	-	Top	2009	[102]
Glass slide, CaF_2	-	Top	2006	[39]
Glass slide	Ag (50)	Top	2005	[22]
Optical fiber	-	Top	2005	[103]
Si	Ag (500)	Top, Side	2008	[23]
Glass slide	Ag (500)	Top, Side	2008	[104]
Glass slide	Ti/Ag (50/500)	Top	2009	[105]

Table 2 Summary of previously reported Ag nanorods thin films grown using OAD technique on various substrates

Since the initial nucleated droplets which catalyze the growth of nanocolumns, the evolution of the early stage nucleation in these films was also studied by terminating the growth after a few mono layers. The density and size distribution of the nucleated droplets provide several revealing insights on the physical evolution of the film, and useful for validating the observations and results.

2.2 Surface diffusion theory and analytical modeling

The vapor atoms from the evaporation source travel towards the substrate surface and condense. During condensation, they can either bounce back or adsorb on the substrate surface. These adsorbed atoms are termed as adatoms. Vapor atoms posses higher energy than the atoms in the film and therefore the excess energy of the vapor atoms are dissipated to the atoms in the film. After the energy transfer, the atoms randomly migrate over the film or substrate surface. This random motion of atoms is known as surface diffusion. While the atoms are in motion, they may hop from site to site on the substrate or films surface and randomly diffuse away from the initial condensation site. The energy required for the adatom to hop from site to site is defined as the hop energy. Mean hop time is defined as the time between adatoms hop from one site to another and is influenced by the films temperature (or substrate temperature), hop energy and lattice vibration frequency [59].

Adatoms may re-evaporate if they posses enough activation energy to leave the film or substrate surface, if the motion of adatoms is not impeded by the new flux of incoming vapor atoms. This activation energy is defined as the escape energy of the adatom. Hop and escape energies of adatoms depends on their surroundings which means that the adatoms motion and the associated energies are different depending on their interaction with the substrate or among themselves. Atoms interaction is mostly with the substrate during the initial nucleation stage. Therefore the required activation energies for the random motion is lower which results in higher surface diffusion during the nucleation stage. The nucleation stage is crucial and determines the film properties like defects, column size, stress, etc. After this stage, adatoms interaction is mainly with the

same type of atoms during the film growth stage since more than a monolayer of atoms has condensed on the substrate surface [59].

The motion of adatoms is eventually impeded and stopped by the flux of new incoming vapor atoms or if they delivered all its energy to the atoms in the film. As the deposition rate increases, adatoms on the film or substrate surface will be buried under the newly arriving atoms. This implies that the average surface diffusion distance travelled is also governed by the deposition rate. Burial rate of adatoms is defined as the rate at which atomic layer formation equals the mean hop time of adatoms.

Surface diffusion and mobility of atoms has been extensively studied by Abelmann in Ref. 59. A set of analytical expressions are proposed by Abelmann which explains the relationship of process conditions such as deposition rate, influence of substrate temperature and background gases on the surface diffusion behavior of atoms. In this study, we model the behavior of Ag atoms on Ag surface and cobalt (Co) atoms on Co surface to understand the surface diffusion phenomena of low (Ag) and high (Co) melting temperature metals. Behavior of Co atoms on Co surface was discussed by Abelmann in the paper. Average surface diffusion distance and the mean adatom hop time as a function of substrate temperature and deposition rate is calculated based on the analytical expressions proposed by Abelmann [59].

2.2.1 Results and discussion

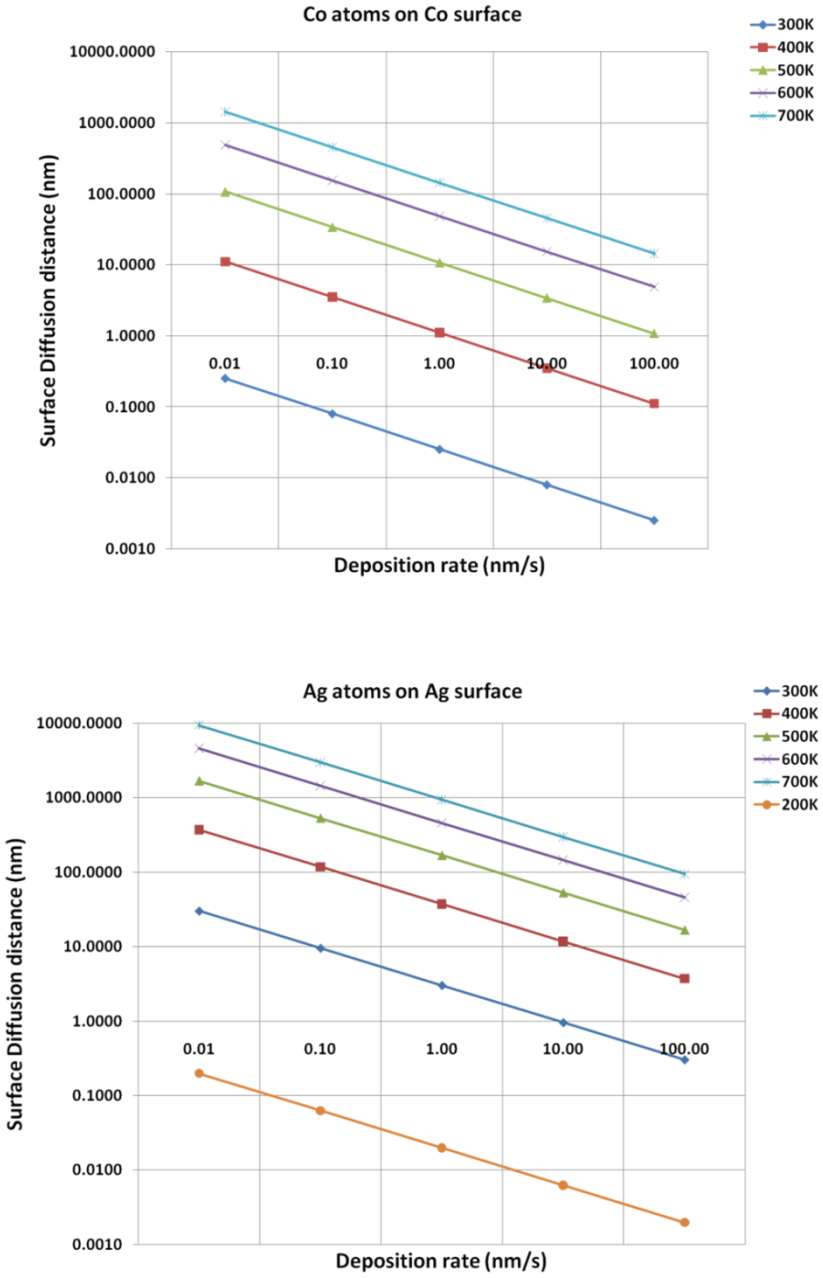

Figure 5 Average surface diffusion distance as a function of substrate temperature and deposition rate

Figure 5 shows the behavior of Co atoms on Co surface and Ag atoms on Ag surface as a function of substrate temperature and deposition rate. The activation energies required for the Arrhenius type behavior of adatom motion on the substrate surface is estimated using the heat of vaporization energies for the respective metal. The plot shows a linear decrease in the average diffusion distance travelled by the adatom on the respective metallic surface. As the film temperature decreases and the deposition rate increases, the average diffusion distance decreases. At 300 K, the average diffusion distance is significantly higher for Ag atoms than Co atoms. For OAD technique to work for a specific material, it is imperative that the diffusion of the atoms be as small as possible. Higher surface diffusion will cause the atoms to land in the shadow areas of the previously nucleated sites. This will eventually result in collapsed and low aspect ratio columnar thin film structure. We observe this effect in the SEM results of Co and Ag nanorods thin films grown on silicon substrate. Co nanorods thin films appear to have high aspect ratio columnar structure compared to Ag nanorods thin films grown at room temperature.

It should be noted that the behavior of metal atoms on metallic surface discussed by Abelmann is based on the estimation of activation energies using the heat of vaporization of the metal. In reality, the behavior of depositing atoms on the silicon or glass substrates is more realistic to understand the surface diffusion behavior. However the challenge is to estimate the activation energies of atoms on the substrate (silicon or glass) surface. This fact has been acknowledged by Abelmann as well. Further explanation on this aspect is discussed in Section 2.4.1.

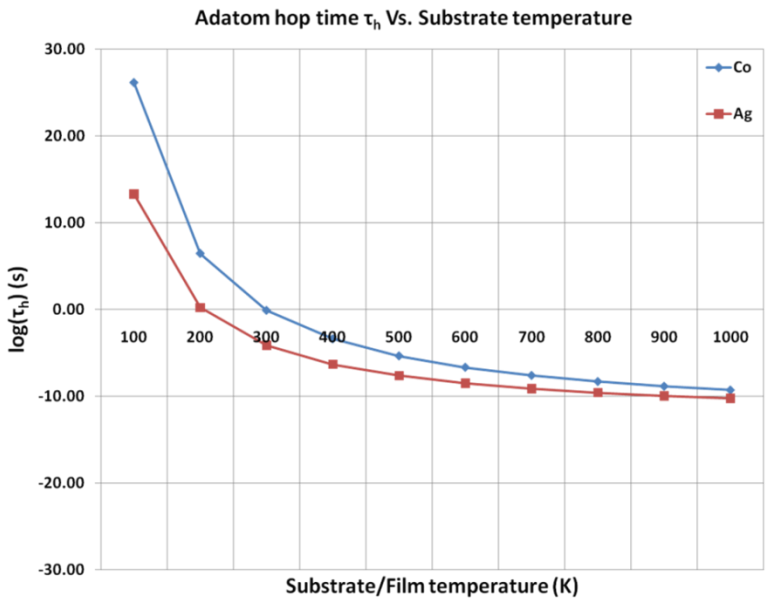

Figure 6 Co and Ag adatom hop time on Co and AG surface respectively as a function of substrate temperature

Figure 6 shows the mean hop time of Ag and Co atoms on Ag and Co surface respectively. It is clear that at room temperature Co atoms are hopping less frequently compared to Ag atoms. The behavior also predicts the effect of substrate temperature in reducing the adatom hopping. As the substrate temperature decrease down to 100 K and 200 K, the mean hop times increase exponentially. It implies that the adatom may not have enough energy at low substrate temperature to frequently hop and diffuse away on the substrate. Table 3 shows the discrete adatom hop time values at different substrate temperatures.

Substrate temperature (K)	Co τ_h (s)	Ag τ_h (s)
100	1.41e+26	2.02e+13
200	2.80e+06	1.64e+00
300	7.59e-01	7.08e-05
400	3.95e-07	4.66e-07
700	2.37e-08	7.29e-10

Table 3 Mean adatom hop times for Co atoms on Co surface and Ag atoms on Ag surface as a function of substrate temperature

2.3 Experimental details

2.3.1 Custom built cryogenically cooled substrate holder

In order to cryogenically cool the substrates to near liquid nitrogen (LN_2) temperature (77 K), a custom built substrate mounting plate was designed in house. Figure 7 shows the schematic of this cooling setup.

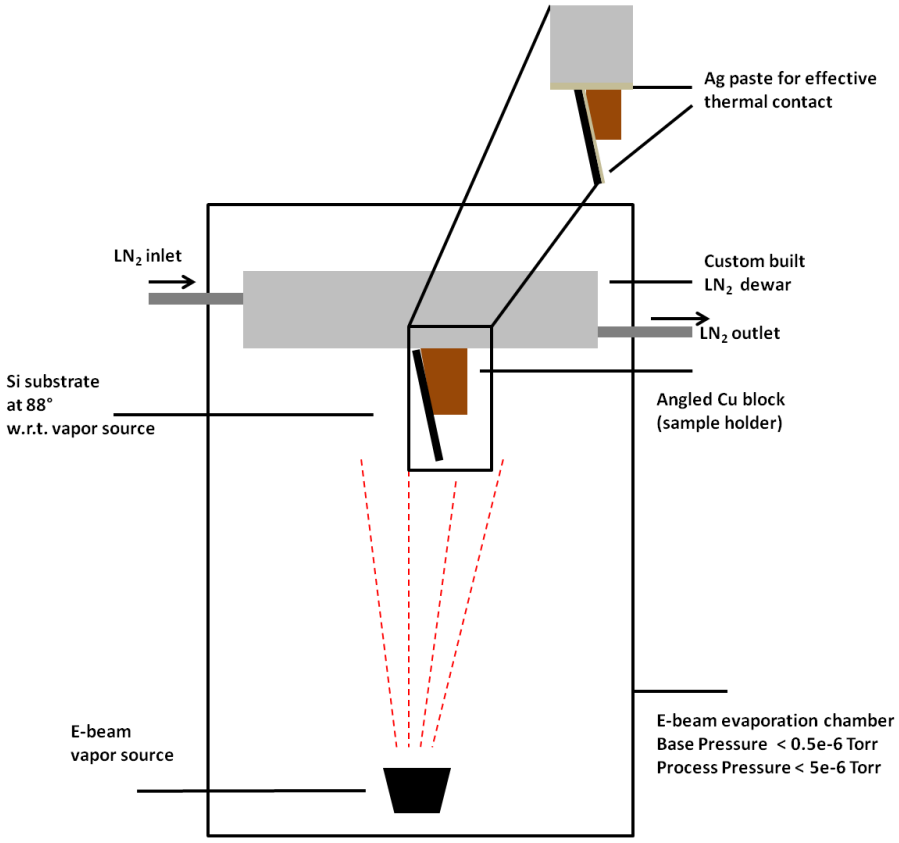

Figure 7 Schematic shows custom built cryogenic substrate cooling setup. The setup allows concurrent fabrication of STF at 100 K and 300 K substrate temperature.

The steel plate is a two-piece sandwich construction with milled flow channels inside in the bottom plate which is welded together to the top plate. The substrate mounting plate was designed to carry LN_2 in an open-cycle dewar configuration. LN_2 feed-through was

installed in the deposition chamber for the delivery of LN_2 without dissipating the heat to the chamber side walls. Stainless steel flexible hose were used for connecting the feed-through to the substrate mounting plate. Copper and Teflon angled blocks with a preset angle of 88° were fabricated and mounted side-by-side on the LN_2 carrying plate. Therefore all depositions in this study were done at an oblique angle of 88°.The high and low thermal conductivities of the copper and Teflon blocks enable simultaneous growth of two samples under identical conditions except for their substrate temperatures. Si substrates were held with a mechanical clip on the angled face of the copper and Teflon blocks. To ensure good thermal contact between the mounting plate - copper blocks and Si - copper block, silver paste was used. Two type-K thermocouples were used for temperature measurement of the copper and Teflon blocks near the substrates. The temperature reading of the copper and Teflon blocks were approximately 100 K and 300 K respectively during deposition. These temperatures are indicative of the substrate temperature. Due to the thermal load present during the evaporation process, the copper and Teflon temperature increased by approximately 15 K during the deposition process.

Entire cooling setup was leaked checked several times prior to deposition of thin films to verify the absence of any leaks from the substrate mounting plate carrying LN_2.

This experimental setup is novel and unique for the fact that it allows concurrent side-by-side fabrication of nanorods thin films at near room and cryogenic substrate temperatures. Except for the difference in substrates temperatures, all other deposition parameters such as the effect background gases, deposition conditions, etc. are held constant during the deposition. Therefore, the current study should result in true comparison of cryogenic and room temperature growth of nanorods thin films.

Figure 8 shows the custom-built cryogenic substrate cooling setup.

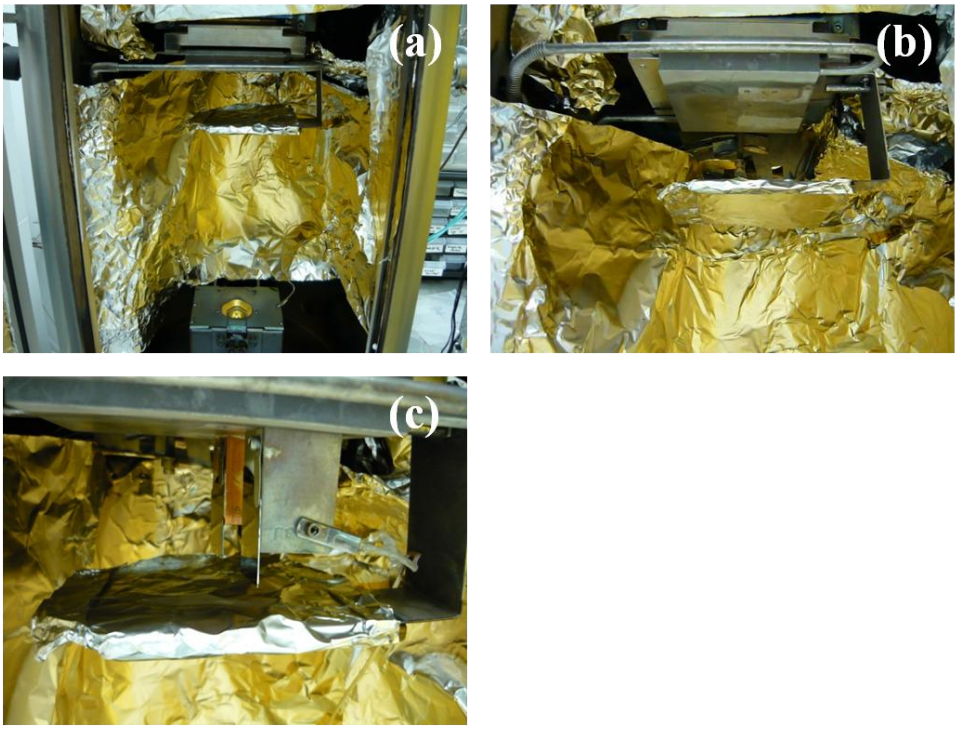

Figure 8 Image of custom built cryogenic substrate cooling setup. (a) Inside of e-beam deposition chamber and (b) cryogenic cooling setup (c) Copper and Teflon sample mounting stage for concurrent fabrication of nanorods thin films at near 100 K and 300 K temperature

2.3.2 Fabrication of nanorods thin films using OAD technique

Depositions were done in a MDC evap-4000 e-beam evaporator which is a generic vacuum chamber designed by Torr International. The chamber is not equipped with special glancing angle or oblique angle deposition apparatus. OAD apparatus (copper and Teflon blocks) was integrated with the substrate mounting plate carrying LN_2 as shown in Figure 8. The vapor source to substrate distance is 0.5 meter. Prime grade Si <100> wafers cleaned with acetone, methanol and isopropyl alcohol were used in all depositions. Ag, Au and Cu evaporation pellets were 99.99 % purity (Kurt J. Lesker Company) and the chamber base pressure was less than $66x10^{-6}$ Pa (~ $0.5x10^{-6}$ Torr) prior to each deposition. After the initial film conditioning ramp, the deposition rate was maintained at 0.3 nm/s for a total film thickness of 300 nm using a quartz crystal sensor coupled with Sigma SQC-310 thin film deposition controller with a tooling factor calibrated from prior depositions. For the early nucleation stage study, the growth was prematurely terminated at 100 Å and 300 Å. The deposition rate was maintained at 0.05 nm/s. Before the start of the deposition, LN_2 was allowed to flow through the mounting plate to ensure the temperature of the copper block reads approximately 100 K. LN_2 is allowed to flow continuously during the deposition.

2.3.3 SEM and Image analysis

SEM images were acquired using a Hitachi S-4800 high resolution SEM to characterize the nanostructured thin films with cross sectional and top views. ImageJ software was used to analyze the density and size distribution of nucleated droplets formed in the early stage nucleation study [83]. Top view SEM images shown in Figure 14 were used for size and spacing distribution analysis. For spacing distribution study, pixel intensity data from the randomly drawn horizontal lines (N = 10) across the SEM images were used to generate space distribution data. For each experimental condition, data points ranging from 400 to 1600 were used depending on the particle size of different samples.

2.4 Results and discussion

2.4.1 Physical morphology

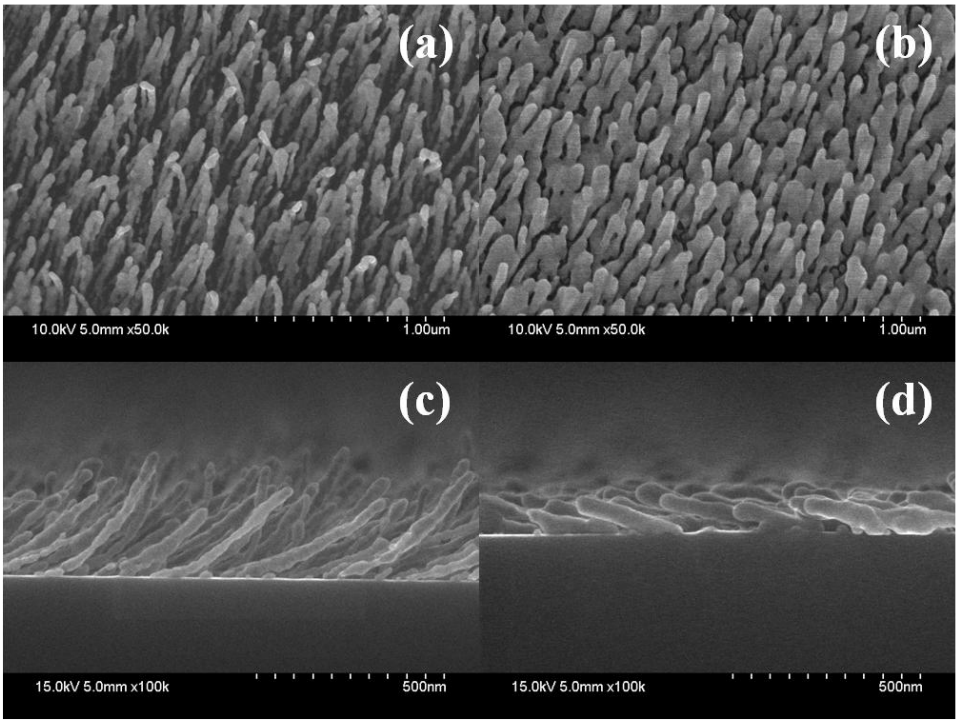

Figure 9 Top and side view SEM results showing Ag nanorods thin films grown at 300 K and 100 K substrate temperature. Film thickness is 300 nm. (a) top view at 100 K (b) top view at 300 K (c) side view at 100 K (d) side view at 300 K

Substrate Temperature (K)	Length (nm)	Diameter (nm)	Tilt Angle (°)	Nanorods density (rods/μm^2)
100	428 ± 20	36 ± 10	43 ± 10	55 ± 5
300	273 ± 21	50 ± 3	18 ± 1	32 ± 4

Table 4 Physical differences in the nanostructure of Ag nanorods thin film grown at 100 K and 300 K

Figure 9 shows the SEM results (cross-section and top view) of the Ag nanorod thin films grown at 100 K and 300 K. Both side view and top view images reveal the differences in the morphology between the two films. 300 K grown nanorods appear to have 28 % larger diameter and are less distinctly separated from each other. The top view image (Figure 9 (b)) also shows the merged and diffused adjacent nanorods. Also the nanorods inclination angle with the substrate surface was also much smaller for 300 K than 100 K grown films. This lower angle at 300 K is indicative of the collapsed physical structure of the films grown at this temperature. On the other hand, the nanorods grown at 100 K appear to have much smaller diameters and are more distinctly separated from each other, as seen in the cross section and top view images. Therefore these differences between 100 K and 300 K grown films will influence the aspect ratios of these films. Estimated aspect ratio was in the range of 14 to 15 for 100 K compared to 5 to 6 for 300 K grown films. In addition, the estimated numbers of nanorods within a square micron area using the top view images were approximately 55 for 100 K compared to 32 nanorods for 300 K. Unlike in high melting temperature metal nanorods thin films, the Ag nanorods grown

at 100 K have shown a curvature, or a sag, in their structure. This effect is most likely due to the softness of the metal and the high aspect ratio of these rods which has an influence on the spring constant of the individual nanorods. With high aspect ratio and softness of the metal, the mechanical spring constant of nanorods grown at 100 K might be very small compared to that of the low aspect ratio nanorods grown at 300 K. Similar sag has also been observed with Cu nanorods (Figure 11) grown at 100 K. Table 4 summarizes the physical structural differences of Ag nanorods thin films. The surface area of the Ag nanorods thin film grown at 100 K was estimated to be 1.6 times higher than that of 300 K grown. These differences in the spatial arrangement of nanorods at two temperatures and the physical differences will likely have an influence on their optical, plasmonic, mechanical and electrical properties.

The knowledge of how the metal atoms behave on the substrate is important to speculate on its ability to form high aspect nanorods. In order to identify the temperature at which the diffusion and mobility of metal atoms would be low enough to result in high aspect ratio nanocolumns, one has to know the metal atom's activation energy on the substrate surface. Previous studies have the investigated the kinetics behavior and self-diffusion of adatoms on different substrate surfaces [65 – 68]. However the kinetic properties of Ag and of several other soft metals on silicon substrates have not been quantified. The reason is due to numerous factors such the dangling bonds of the crystal surface, surface impurities, deposition conditions, adsorbed gases etc. Abelmann et. al. studied the behavior of Co atoms on Co surface using a set of analytical expressions that denotes the surface diffusion behavior of Co atoms on Co surface, however it's behavior on Si or glass substrate is not well understood to result in any reliable model [59].

Therefore the motivation for this study was based on the Arrhenius type surface diffusion behavior of atoms diffusion on the substrate. Based on the surface diffusion formula it is clear that at low substrate temperatures the surface diffusion of atoms will also decrease. At such low enough cryogenic substrate temperatures, a noticeable difference in the growth mechanism of metal nanorod thin films was expected, especially for softer metals such Ag, Au and Cu which generally exhibit higher surface mobility. Therefore, in this study the influence of substrate temperature was done at near LN_2 temperature (100K) and room temperature (300K). To attain low enough substrate temperatures in a vacuum chamber during the deposition, LN_2 based cooling has shown to be an effective method LN_2 is a commonly used refrigerant and therefore was a viable choice for substrate cooling. Thermoelectric based cooling is an alternative however it is limited by how low a substrate temperature can be attained.

Since it was not clear at what substrate temperature high aspect ratio metal nanocolumns starts to evolve, the growth of Ag nanocolumns at 180 K was also investigated as an intermediate data point. Figure 10 shows the top and side view SEM results of the Ag nanorods thin films grown at 180 K. The SEM results are very similar to the ones grown at 100 K. Similar curvature of individual nanocolumns was also observed. Such sag or curvature of nanocolumns is not observed in SiO_2 nanorods thin films grown at similar temperatures. This indicates that this behavior is material dependent and mostly observed in softer metals (Ag and Cu).

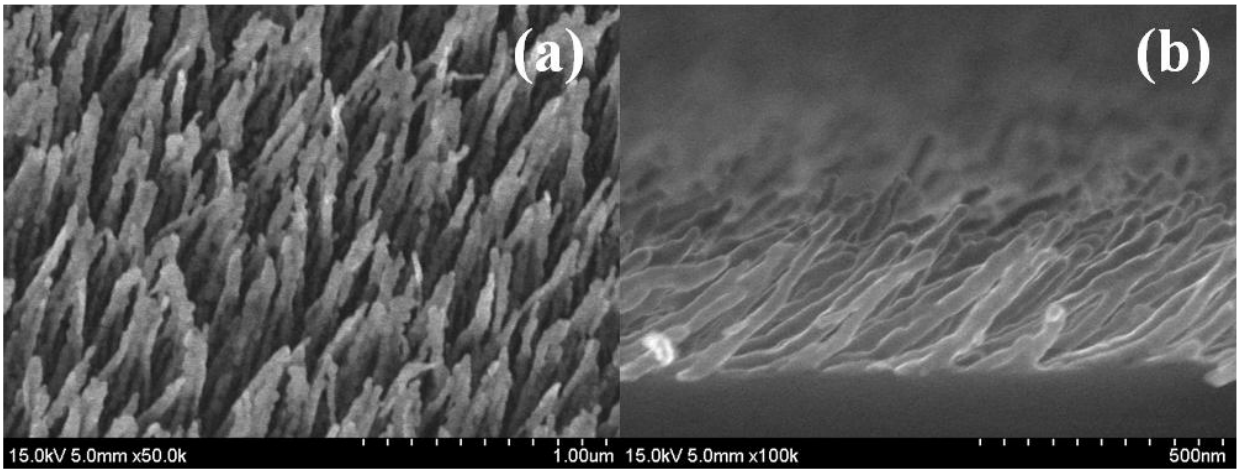

Figure 10 Top and side view SEM results showing Ag nanorods thin films grown at 180 K substrate temperature. Film thickness is 300 nm. (a) Top view (b) side view

It should be noted that the above observations are only discernable from the cross section images, and are not so obvious from the top view images. This is despite the fact that most prior publications on Ag nanorods have used the top views to characterize the morphology. The top-view images in Figure 9 (a) and 9 (b) both show evidence of column-like structures, and the fact that most of the nanorods grown at 300 K are laying nearly flat on the substrate is not evident until the cross section is examined.

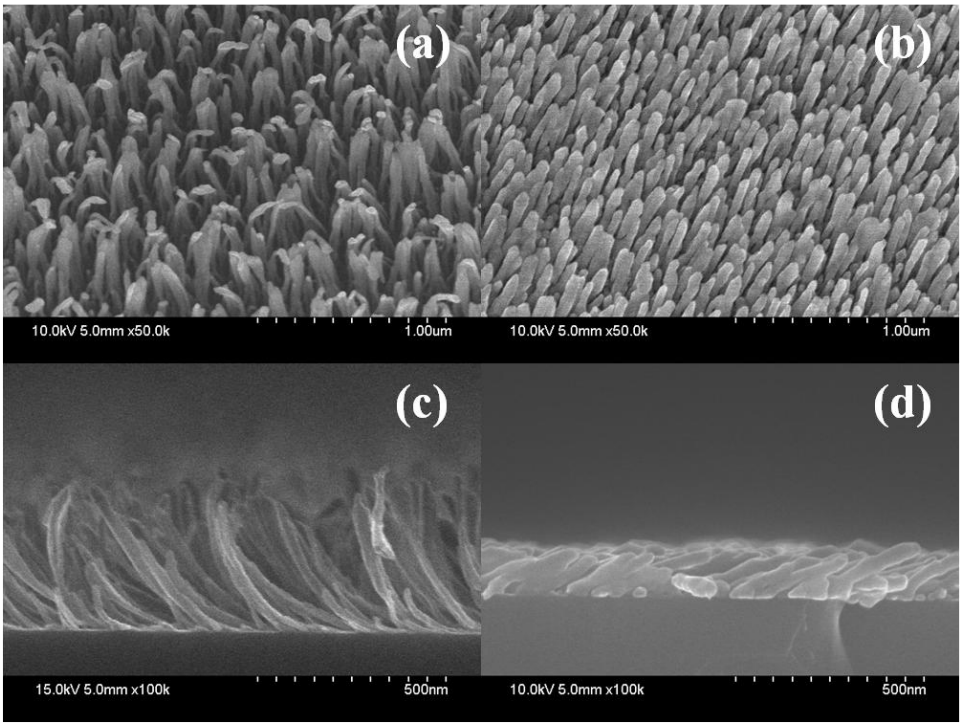

Figure 11 Top and side view SEM results showing Cu nanorods thin films grown at 300 K and 100 K substrate temperature. Film thickness is 300 nm. (a) top view at 100 K (b) top view at 300 K (c) side view at 100 K (d) side view at 300 K

Substrate Temperature (K)	Length (nm)	Diameter (nm)	Titl Angle (°)	Nanorods density (rods/μm^2)
100	475 ± 47	31 ± 6	62 ± 5	88 ± 11
300	239 ± 39	41 ± 8	24 ± 4	77 ± 3

Table 5 Physical differences in the nanostructure of Cu nanorods thin film grown at 100 K and 300 K

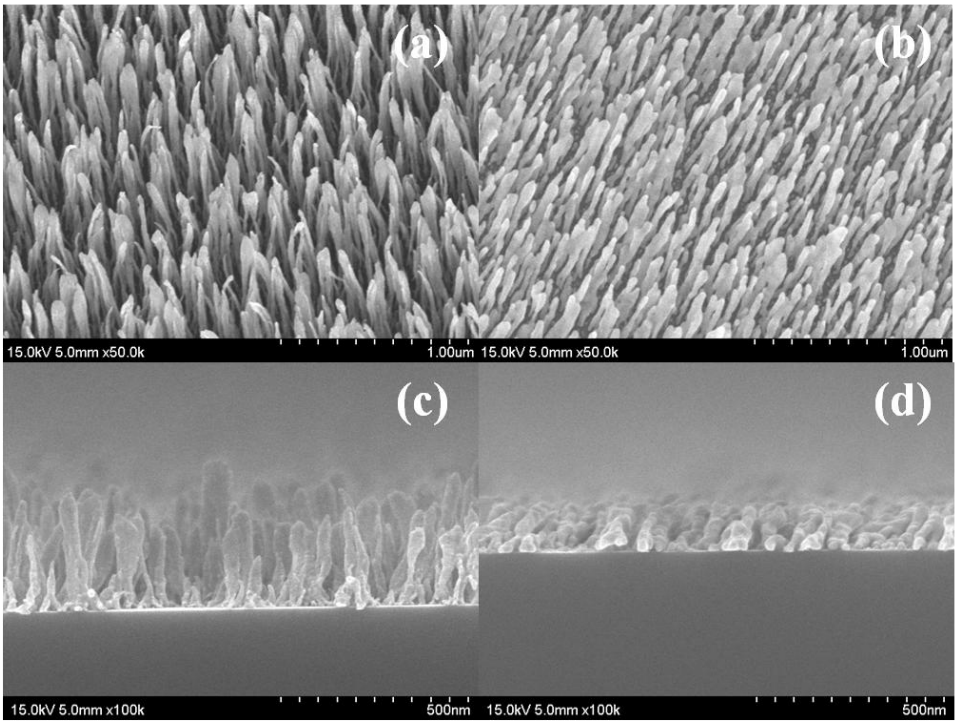

Figure 12 Top and side view SEM results showing Au nanorods thin films grown at 300 K and 100 K substrate temperature. Film thickness is 300 nm. (a) top view at 100 K (b) top view at 300 K (c) side view at 100 K (d) side view at 300 K

Substrate Temperature (K)	Length (nm)	Diameter (nm)	Titl Angle (°)	Nanorods density (rods/μm^2)
100	265 ± 81	45 ± 9	89 ± 2	76 ± 4
300	106 ± 13	48 ± 27	88 ± 11	78 ± 8

Table 6 Physical differences in the nanostructure of Au nanorods thin film grown at 100 K and 300 K

Figure 11 and 12 shows the SEM imaging results indicating the difference in columnar morphology of Cu and Au nanorods thin films grown at 100 K and 300 K substrate temperature. The side view SEM images for Au nanorods reveal near straight nanocolumns formation unlike the tilted nanocolumns growth as seen in most other metals (Figure 1). It is known that nanorods angular orientation is material dependent and the inclination angle is different than the oblique deposition angle. Models have been proposed to predict the nanocolumns tilt angle as a function of deposition angle [3, 5]. Typically for the formation of straight vertical nanorods thin films, the substrate is held at an oblique angle and simultaneously rotated fast enough to result in vertical nanorods. The behavior of Au nanorods as found in this study needs further investigation to identify the cause for the evolution of this morphology.

2.4.2 Surface diffusion and nucleation study

The improvement and the observed differences in the nanorod formation at cryogenic temperatures can be attributed to the reduction in surface mobility of Ag, Au and Cu atoms on the Si surface. Surface diffusion and mobility of the atoms on the substrate surface has a strong influence in the growth of nanostructured thin films [2, 8, 26, 58 – 61]. The diffusing distance of each atom from the initial landing site is a function of the incident energy of the vapor atoms and the substrate temperature. At low substrate temperatures, the incident atoms are likely to be almost frozen on impact and the diffusion away from the landing site will be significantly minimized. As a result, the shadow regions of the previously nucleated atoms on the substrate remain "dark" and free of atoms. Such conditions are highly favorable for the growth of nanorods thin films. At higher incident energy or substrate temperatures, the atoms will diffuse away from their initial landing sites into the shadow areas, which will undermine the essential mechanism that contributes to nanorod growth in OAD. For this reason, sputter deposition technique is not highly favorable for the growth of nanorods thin films, since sputter atoms are likely to have nearly 100 times higher incident energy than the evaporated vapor atoms.

Another important aspect of the current study is the growth of nanorods films on crystalline substrate. Previous studies have demonstrated Ag nanorods on amorphous substrates (glass, CaF_2) or on Si substrate with polycrystalline thin film deposited at normal incidence prior to OAD [23, 31 - 42]. A summary of this is provided in Table 2. It is believed that the surface diffusion of atoms is higher on crystalline substrates than on non-crystalline or polycrystalline surfaces, which increases the chances for the formation of columnar metal films on non-crystalline surfaces [59]. In the context of this

discussion, the presence of a polycrystalline thin film deposited at normal incidence is referred as the barrier layer. The schematic in Figure 13 illustrates this concept for Ag OAD films demonstrated by other authors.

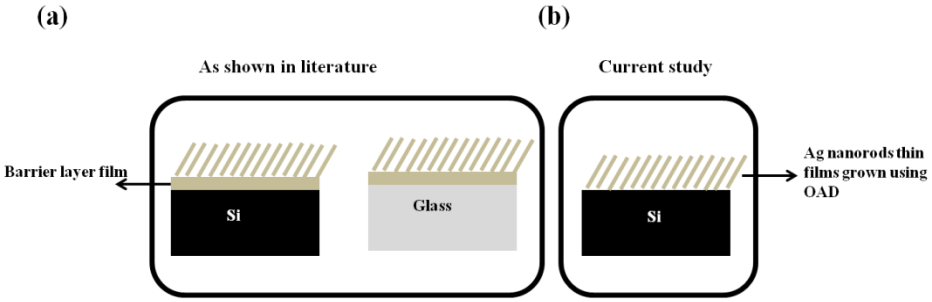

Figure 13 Schematic showing Ag nanorods grown on Si and glass substrates (a) with normal incidence deposited barrier layer thin film (as seen in literature) (b) without barrier layer thin film (current study).

Polycrystalline thin films deposited at normal incidence will most likely have nanometer scale granular structure and have so called “grain boundaries”. These grain boundaries will impede the free random motion of atoms and therefore reduce the diffusion distance which prevents the vapor atoms from entering the shadowed areas. Contrary to this behavior, on the crystalline substrates, the surface diffusion during the early nucleation stage is much higher than during the subsequent film growth stage because the atoms mostly interact with the smooth substrate during the early stage. After the initial nucleation, as the film thickness increases, the interaction with the substrate decreases and grain boundaries start to dominate. Hence, the choice of substrate has a great influence on the ability to grow OAD nanorods. Despite the successful use of barrier layers to grow Ag nanorods, it is not without significant compromises. The introduction of a barrier layer is an additional interface which will influence the inherent

anisotropic optical and electrical properties of these nanorod thin films. The flexibility of being able to grow Ag, Au, and Cu nanorods on either crystalline or non-crystalline surfaces undoubtedly has attraction.

In order to more carefully examine the effects of substrate temperature on the diffusion and distribution of nucleation islands we terminated the OAD growth at 100 Å and 300 Å to have snapshots of their evolution. Figure 14, 15 and 16 show the top view SEM images, size distribution and particle spacing between the nucleated Ag islands grown at 100 K and 300 K respectively. Table 7 shows the size and spacing distribution data from the nucleation study.

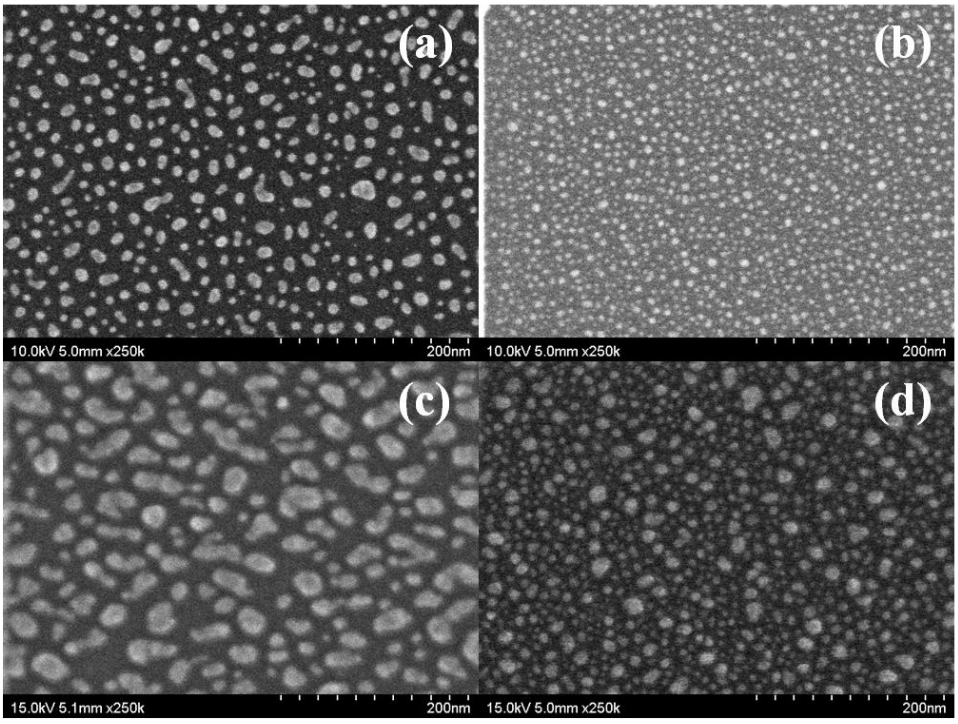

Figure 14 Top view SEM results showing early stage nucleation study by terminating the Ag nanorods thin films growth at 100 Å (top row) and 300Å (bottom row) at 300 K and 100 K substrate temperatures. (a) 100 Å at 100 K(b) 100 Å at 300 K (c) 300 Å at 100 K (d) 300 Å at 300 K.

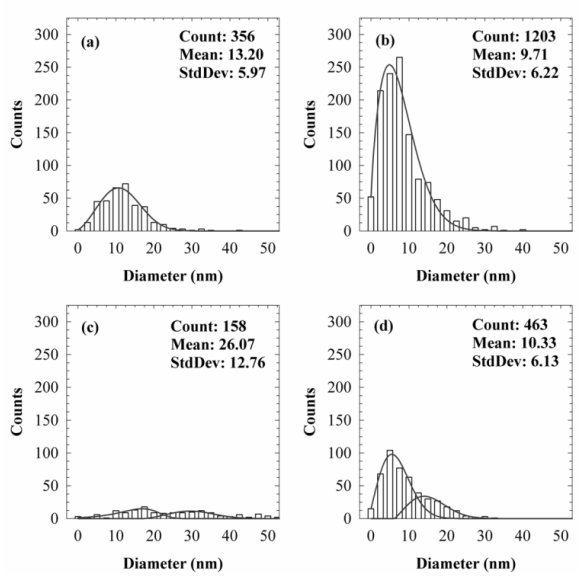

Figure 15 Plot showing particle size distribution of nucleated Ag islands from the SEM results shown in Figure 14. (a) 100 Å at 100 K (b) 100 Å at 300 K (c) 300 Å at 100 K (d) 300 Å at 300 K

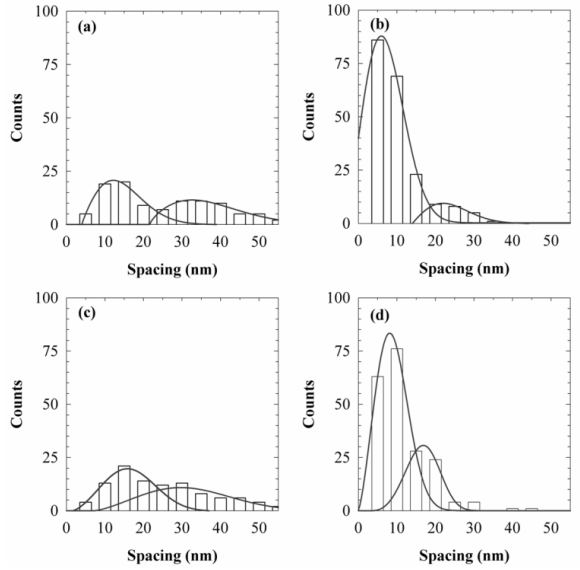

Figure 16 Plot showing adjacent particle spacing distribution of nucleated Ag islands from the SEM results as shown in Figure 14. (a) 100 Å at 100 K (b) 100 Å at 300 K (c) 300 Å at 100 K (d) 300 Å at 300 K

	100 Å		300 Å	
	100 K	300 K	100 K	300 K
Counts	416	1608	412	804
Size	13.2 ± 5.97	9.71 ± 6.22	26.07 ± 12.76	10.33 ± 6.13
Spacing	18.25 ± 17.72	5.94 ± 5.48	21.43 ± 16.97	7.14 ± 5.97

Table 7 Size and spacing distribution data based on the SEM result analysis as shown in Figure 14

Figure 15 and 16 show a much smaller average particle size, smaller spacing's and a smaller size distribution at 100 K than at 300 K. At first, this may seem counter-intuitive because one might expect that freezing all atoms at their initial landing site should lead to a denser distribution of tiny droplets. While this is in fact what is observed with normal incidence films, the apparently unusual behavior here is due to the inclination angle used in OAD. At the 88° inclination, assuming the intercept diameter is the same as the Ag atomic diameter of 3.2 Å, each atom that lands on the substrate will create a shadow spanning roughly 9 nm behind that atom. Since there is likely to be some mechanical variability in our 88° substrate mount, the shadow length could also have a deviation around 9 nm. For the purpose of illustration, we will assume that surface diffusion is negligible at 100 K compared to 300 K. This means subsequent atoms can either condense on top of the first atom, or condense further than 9 nm behind the first atom. They can also land in front of the first atom closer than 9 nm, assuming it is not closer than 9 nm behind another atom. When two atoms happen to land closer than 9 nm, only

one can survive and receive further atoms to continue its growth into a collection of atoms, or islands. This competition will be determined by the stochastic distribution of the atoms in the vapor flux. The result can be seen in Figure 14, where the growth was terminated after 100 Å and 300 Å of thickness. The Ag islands grown at 100 K showed an average island size around 13.2 nm with an average spacing of 15 nm or greater. At 300 K the maximum spacing was about 5 nm, with some smaller islands in the valleys. The smaller islands were the ones that have lost the competition and no longer receive any new incoming vapor atoms. The average island size at 300 K was 9.71 nm and the standard deviation was 6.22 nm. For the islands grown at 300 K the incident atoms had sufficient energy to diffuse randomly on the surface before coming to a rest. The 9 nm shadow behind an atom would not be static, but rather a moving shadow for the duration of the diffusion time. The subsequent atoms can land on the initial atoms and form islands, or land outside the shadows of the initial atoms to form their own nucleation centers. However, since the shadows themselves were moving and the subsequent atoms would also randomly diffuse after landing, this effectively allowed the incident atoms to come to a rest at random locations, at much finer intervals than the shadow distance of 9 nm. This was in agreement with the observed average spacing value of 5 nm at 300 K, which can be seen in Figures 14 (b) and 16 (b), where the islands were much smaller and more densely packed than that of 100 K.

As growth continued to 300 Å, Figure 14 shows larger islands forming with a mean size of 13.2 nm at 100 K and 9.71 nm at 300 K. The largest of these will continue to become the nanorods. At 100 K, the average island size at 300 Å thicknesses seems to have doubled from that of 100 Å. This could be a result of coalescence of adjacent islands

which will cause the islands to grow in size with irregular non-spherical shapes as seen the Figure 14 (c). Also the mean spacing at 300 K has doubled from 5 nm at 100 Å to 10 nm at 300 Å.

Based on the size distribution and the mean spacing between adjacent particles, it is clear that at 300 K, Ag atoms were diffusing over the substrate surface and moving into the shadowed areas. This conclusion was based on the fact that average shadow distance for Ag atoms was ~ 9 nm and the observed spacing between Ag atoms at 300 K was ~ 5 nm. However as the thickness of film increases, clusters of Ag atoms starts to coalesce and form bigger Ag particles. This was observed in the SEM image at 300 K with 300 Å film thickness. As the film thickness continued to increase, several of these bigger Ag particles can coalesce further and formed even bigger particles and eventually started to form bigger diameter columnar structure. On the other hand, for 100 K, the spacing between adjacent particles was much larger than the shadow distance (~ 15 nm), indicating very few Ag particles have diffused in the shadowed areas. These phenomena minimized the increase in Ag particle cluster size and the extent of coalescence was much smaller compared to that of 300 K. This behavior explains why diameter of nanorods at 100 K was smaller than that of 300 K.

By lowering the substrate temperature to 100 K, we have reduced the T_s/T_m ratio for Ag from 0.24 to 0.08, which has clearly led to the observed improvement in their columnar morphology. T_s/T_m is clearly indicative of the quality of the nanorods, but unlike as indicated in Deniz's report, its numerical value cannot be taken as a hard threshold for determining if nanorods will grow or not. Other metals with low melting temperature such as Al, Sn, and Cu etc. can also be improved by lowering the substrate temperature,

although the T_s/T_m values where significant improvement will be seen may vary from that of Ag.

2.4.3 Chemisorption theory

During the early stages of this research, our motivation for studying the growth phenomena in OAD technique was based on the morphological differences observed in the columnar morphology of low and high melting temperature elements (Figure 1). Elements with low melting temperature like Ag, Cu, Au and Al etc. consistently have shown to form collapsed low aspect ratio nanorods thin films compared to film grown using high melting temperature metals like Ti, Cr, Ni, and Co etc. In fact Au and Al nanorods thin films have not been reported in literature, despite relatively long existence of OAD technique. Researchers have even claimed that nanorods thin films made from elements with melting temperature lower than that of aluminum may not evolve with columnar morphology [61]. This behavior is attributed to the high surface mobility of atoms from low melting temperature metals on the substrate surface. As explained earlier, surface diffusion and mobility is even greater on crystalline substrates than on polycrystalline substrates. In the current study, we have shown how the substrate temperature will influence the columnar morphology of Ag, Cu and Au nanorods thin films.

However our results were not indicative to establish the influence of melting temperature of material to its diffusion and surface mobility behavior i.e.

1. Why high melting temperature elements tend to have lower surface mobility than low melting temperature elements?
2. How melting temperature of the element influences the mobility of the atom on the substrate surface.

In this section, we attempt to explain this behavior. Our explanation relies on the nucleation and condensation behavior of atoms on the substrate surface.

In the evaporation process, vapor atoms impinge on the substrate surface and either condense or re-evaporate after some residence time. This process depends on how the atoms react with the substrates and among themselves, the substrate temperature and flux of diffusing atoms on the substrate. During condensation process atoms lose their energy by bonding to other atoms or the substrate. The energy lost to the surface could be a combination of processes which includes, atoms chemical reaction with the adsorbed species on the surface, interaction with the defects, impurities etc. on the surface and collision with diffusing atoms on the surface. Mobility of the atoms on the surface mainly depends on the following

- Energy of the atoms
- Atom – surface interaction
- Substrate temperature
- Crystallography of the surface

The type of chemical bonding (metallic, columbic, electrostatic or van der Waals) the atoms undergo affects the surface mobility. If the atoms interaction with the substrate is strong, surface mobility would be low and each atom on the surface could be a potential nucleation site. This explains why most high melting temperature elements form small diameter, high aspect ratio nanorods. Atoms are said to be chemically adsorbed (chemisorbed) if they chemically react with the surface atoms. On the contrary, they are said to be physioadsorbed on the surface, if the atoms are just weakly held by the van der

Waals forces. Typically chemical bond energies are in the range of 1 eV compared to physisorption energies which is in the range of 0.3 – 0.4 eV. If the atom – surface interaction is weak, mobility will be high and atoms tend to condense at surface defect sites, impurities other preferential sites [69 - 72].

In most cases, silicon (or other) substrates are likely to have a native layer of oxide or adsorbed O_2 and other gaseous atoms on the surface. Despite efforts to remove the oxide layer using wet or dry etching techniques; monolayer of silicon dioxide exists prior to deposition. Even the vacuum chamber pump down time is enough to allow O_2 and other gaseous atoms to adsorb on the surface which are potential sites for chemical reaction between the incoming vapor atoms. Most depositions are typically done in the presence of adsorbed gases on the silicon substrate surface, unless special efforts are made for the removal of native oxide. These adsorbed O_2 atoms are free to react with the metal atoms during the condensation process. The bonding between the metal atom and adsorbed O_2 on the substrate surface is proportional to the metal – O_2 free energy of formation. This metal – O_2 reaction form an interfacial region on the substrate surface. The interfacial region in the film influences the adhesion of metal film on the substrate. Most refractory metals have high heat of formation, which indicates highly favorable reaction that allows formation of chemical bond in the interfacial region [69 - 72]. Table 8 shows the heat of formation for common low and high melting temperature metals.

Metal	Heat of formation (kcal/mole)
Ti	-218
Cr	-270
Ag	-7
Au	+ 19
Cu	-40

Table 8 Heat of formation of some common low and high melting temperature metals [69]

This behavior justifies why most high melting temperature metals adhere well to the substrates. For e.g. Ti, Cr metal films are typically used as adhesion layers prior to depositing Au, Cu thin film deposition, because Ti and Cr, both are oxygen active metals which will form an interfacial region and adhere well to the substrate prior to deposition of Au or Cu.

It also implies that most high melting temperature elements will have relatively small surface mobility over the substrate surface due metals atoms strong interaction with adsorbed O_2 on the substrate surface.

Another factor that favors the chemical reaction of high melting temperature elements on the substrate is the binding energy of the atoms. Higher binding energy of the atoms

suggests more external energy is required to separate the atoms from solid to liquid or vapor phase. This implies Ti or Cr atoms will have relatively more energy at the time of condensation on the substrate surface. Higher energy is favorable for the chemical reaction with the adsorbed species on the substrate surface.

In summary, melting temperature of the metal has influence over the condensation energy of the atoms on the substrate surface and how the condensing atoms react with the adsorbed substrate atoms. This implies low heat of formation for low melting temperature metal will result in relatively higher surface mobility than high melting temperature metals.

Chapter 3 SERS characterization – Liquid phase sensing

3.1 Raman and SERS spectroscopy

Raman effect is the inelastic scattering of photons from an atom or molecule. Raman effect was originally discovered by Indian physicist C V Raman in 1928. The incident photons are elastically scattered from the atom or molecule where the scattered photons have the same energy and wavelength as the incident photons. A small fraction of the scattered photons have a different frequency from the incident photons. This shift in wavelength of the inelastically scattered photons provides the chemical and structural information of the molecule. Therefore this is used as a spectroscopic technique in chemistry to study and analyze the vibrational, rotational modes of the molecules in solids, liquids and gases [73].

In the Raman spectroscopy, the sample is illuminated with a monochromatic laser source. The scattered photons close to the incident source are filtered out and the

remainder of the light is collected using a charge coupled detector (CCD) sensor. Raman setup usually consists of optical microscope, excitation laser source, monochromator, and a CCD sensor. A typical Raman spectrum is a plot of Raman scattering intensity versus Raman shift in wave numbers [73].

Surface enhanced Raman scattering or spectroscopy (SERS) technique provides the same information and molecular fingerprint information as the conventional Raman spectroscopy technique, except with much greater signal intensity and sensitivity. A weak Raman the analyte molecules at low concentration of could be greatly enhanced using SERS technique. SERS effect was originally accidentally discovered by Fleischmann, Hendra and Mcquillan in 1974 by observing greatly enhanced Raman signal from Pyridine (Py) on roughened silver electrode [19]. Later in 1977, Van Duyne observed similar effect and concluded that surface area is not the only aspect responsible for the increased Raman signal [20]. There are two possible theories that are attributed to this increase. One is based on the electromagnetic effect causing electric field enhancement. It is based on the excitation of localized surface Plasmon's on the metallic nanostructured surface. The choice of metal dictates the Plasmon resonance frequency. Even though several metals such as platinum, palladium, iron, cobalt, nickel have shown this effect, silver, gold, and copper have shown the best response [23]. The other theory proposed by Creighton is based on the chemical charge transfer by complex formation of the adsorbed molecules on the metallic surface [74]. SERS activity strongly depends on the nanometer scale metal morphology and spatial arrangement of nanostructured metal surface. Metal colloidal nanoparticles, roughened silver thin films substrates, nanorods, nanowires etc. have shown to be effective SERS substrates. Due to its higher detection sensitivity down

to single molecule, SERS technique has gained attraction in several chemical and biosensing applications [23].

3.2 Introduction

SERS was originally discovered in 1970's and since then has gained popularity. SERS possesses the same molecular fingerprint capabilities as Raman spectroscopy does but it offers much higher sensitivity and is capable of detecting analyte molecules presence at extremely low concentrations [75 - 77]. Because of this ability, SERS based substrates have shown to be effective for chemical and biological sensing applications [31 – 44].

Free electron metals such Ag, Au, and Cu have shown SERS response, however Ag is the most attractive metal due to its unique electrical and optical properties [78]. The theory that explains the SERS effect is based on localized surface Plasmon resonance (LSPR) effect. The interaction of visible light with free electron metals at nanometer scale satisfies the Plasmon requirements. The enhancement is due to the strong amplification of the localized electromagnetic fields produced by specific nanometer scale morphology of metallic structures [78]. According to Zhu charge transfer among molecules adsorbed on the metallic nanostructures also contributes to the overall enhancement [78]. Ag based nanostructures has been studied extensively as substrates for SERS, surface enhanced vibrational spectroscopy (SEVS) and surface enhanced infrared absorbance (SERIA) based techniques [22]. Ag based SERS substrates has shown the ability to detect chemical agent [32], viruses [35, 36], food borne bacteria [31] etc. at ultra-low concentration levels [32]. However the ability to produce repeatable and low-cost fabrication technique to develop specific morphology of metallic nanostructures is challenging. This fact has been acknowledged by several other people [22, 23, 40]. Shape, size, and spatial arrangement of the metal at nanometer scale greatly influences

SERS effect [23]. Several methods have been reported in literature for the growth and synthesis of nanostructured material for SERS applications. These includes aggregates of Ag colloidal nanoparticles [79], Ag nanorods (AgNRs) [31 - 45] and nanowires derived using chemical and electrochemical methods [80], lithographically patterned nanoparticles arrays [81] and roughened Ag thin films [82]. Most of these methods are either expensive, time consuming and are not scalable. Therefore its widespread use is not common. Another challenge is the uniformity and reproducibility of these methods. OAD technique has emerged as a potential solution to overcome these challenges. It is an inexpensive and scalable method for fabricating nanostructured thin films. In this technique the substrate is held at an oblique angle with respect to the incoming vapor flux. As the vapor atoms condense and nucleate on the substrate, the shadowed regions behind each site stop receiving the subsequent vapor atoms. Instead, they land on the previously formed droplets, resulting in the evolution of a columnar morphology. Brett *et. al.* provides a comprehensive review on state of the art in thin films grown using OAD technique, its properties, and other potential applications [3, 5]. Numerous papers have been published that discuss the use of OAD technique for Ag nanostructured thin films as SERS substrates [31 – 44]. This technique offers flexibility to change the morphological parameters such shape, size and spatial density of Ag nanorods structures. The influence of morphological parameters on the SERS performance has been studied by Zhao [23].

In Chapter 2 of this study, we investigated the effect of cryogenic substrate temperature on the growth of Ag nanorods thin films using OAD technique. SEM results revealed significant morphological differences (*e.g.*, length, diameter, spatial density, and

overall nanostructured surface area) between AgNRs grown at 100 K and 300 K. Based on the observed differences, it was hypothesized that the SERS-based sensing capabilities of 100 K grown AgNRs would be higher than 300 K grown. Therefore in this study, the SERS response of these thin films grown at these temperatures is characterized and compared. Varying concentrations (10^{-6} M, 10^{-7} M, and 10^{-8} M) of Rhodamine 6G (R6G) molecules in aqueous solution was used as the SERS test probe molecule. Comparison of SERS sensing abilities of AgNRs and widely-used Creighton colloidal Ag nanoparticles (AgNPs) is also addressed. Finally, extensive SERS enhancement factor (EF) calculations are discussed by estimating the number molecules absorbed on the surface of AgNRs through the use of fluorescence spectrophotometer measurements.

3.3 Experimental details

3.3.1 Fabrication of Ag nanorods thin films using OAD technique

All depositions were done using an MDC evap-4000 e-beam evaporator in a generic vacuum chamber (Torr International, Inc.). The melt to substrate distance was 0.5 m. A substrate mounting plate was designed to carry LN_2 in an open-cycle Dewar configuration. The plate had a two-piece sandwich construction with interior milled flow channels inside that were welded together and leak checked. Copper and Teflon angled blocks of a preset angle of 88° were in-house fabricated and mounted side-by-side on the LN_2 carrying plate. The high and low thermal conductivities of the copper and Teflon blocks enabled the simultaneous growth of two samples under identical conditions except for the substrate temperature. Si substrates were held with a mechanical clip on the angled face of the copper and Teflon blocks. Silver paste was utilized to ensure good thermal contact between the Si substrate, the copper block, and the LN_2 carrying plate. Two type-K thermocouples were employed for the temperature measurement of the copper and Teflon blocks near the substrates. The temperature reading of the copper and Teflon blocks were approximately 100 K and 300 K, respectively, during deposition.

Prime grade Si <100> wafers were pre-cleaned with acetone, methanol and isopropyl alcohol (IPA) before AgNRs deposition. The Ag evaporation pellets had 99.99 % purity (Kurt J. Lesker Company), and the chamber base pressure was less than 66.0 x 10^{-6} Pa (~ 0.5 x 10^{-6} Torr). After the initial film conditioning ramp, the deposition rate was maintained at 0.3 nm s^{-1} for a total film thickness of 300 nm. This was achieved using a quartz crystal sensor coupled with a Sigma SQC-310 thin film deposition controller equipped with a tooling factor that was pre-calibrated.

3.3.2 SEM measurements

SEM images of the nanostructured thin films were acquired using a Hitachi S-4800 high resolution SEM with cross-sectional and top views. Image J software was used to estimate the density and size of AgNRs (*i.e.*, length, diameter, and nanostructured surface area) [83].

3.3.3 SERS substrates incubation with R6G molecules

100 K and 300 K AgNR substrates (approximately 1 cm x 1 cm) were immersed for 24 h in 2.0 mL aqueous solution of R6G at varying concentrations (10^{-6} M, 10^{-7} M, and 10^{-8} M). The AgNR substrates were then removed and allowed to dry under ambient conditions before SERS measurements.

3.3.4 Micro-Raman and SERS measurements

Raman and SERS spectra were obtained using a LabRamHR 800 system (Horiba Jobin Yvon Inc.) and the LabSpec v.5 software. A 632.8 nm HeNe laser was used as the excitation source and the confocal hole was set at 300 μm. The backscattered Raman and SERS signals were collected using thermo-electric cooled CCD detector. The focused laser beam spot size on the sample surface was about 1 μm in diameter. Under these experimental conditions, the spectral resolution was about 1 cm^{-1}. SERS maps (50 μm × 50 μm) were collected at two random locations on each substrate of AgNRs prior to and post-exposure in R6G solution using a long working distance Olympus objective (100x)

with a step size of 5 μm. The optimized parameters were determined prior to SERS map data acquisition and these are

a) 3 s acquisition time, 2 spectral cycles and 0.015 mW laser power at 10^{-6} M of R6G,

b) 3 s acquisition time, 2 spectral cycles and 0.15 mW laser power at 10^{-7} M of R6G,

c) 10 s acquisitions time, 5 spectral cycles and 0.015 mW laser power at 10^{-8} M of R6G.

3.3.5 Fluorescence measurements

For an accurate determination of the surface enhancement factors (SEFs), fluorescence emission measurements were performed on the R6G dye solutions prior- and post-immersion. The fluorescence emission spectra of all R6G solutions were collected in a quartz cuvette using a Cary Eclipse fluorescence spectrophotometer (Agilent Technologies, Inc.). The excitation wavelength was 530 nm and the emission spectra were collected in the 545-700 nm range for the R6G aqueous solutions at three different concentrations. 100 K and 300 K AgNRs films of varying dimensions (n = 6) were immersed in 2 mL of each concentration R6G aqueous solution and removed after 24 h. Fluorescence emission spectra were then obtained from the remaining solutions post-immersion.

3.3.6 Raman and SERS data analysis

Raman and SERS data analyses were conducted using MATLAB R2010b [84]. All SERS maps were normalized with respect to the integration time and the laser power. A local baseline was then subtracted from the spectral region of interest (1625 – 1675 cm^{-1}) and

the integrated peak area of the xanthine breathing mode at 1650 cm^{-1} was calculated. SERS images for the AgNRs substrates exposed to varying R6G concentrations were constructed using these integrated area values for each pixel spectrum. Peak area values were further normalized to the maximum pixel value within the SERS map collected from the 100 K AgNRs substrate exposed to 10^{-6} M R6G for visual clarity of SERS map images.

3.4 Results and Discussion

3.4.1 Quantitative and qualitative SERS response comparison

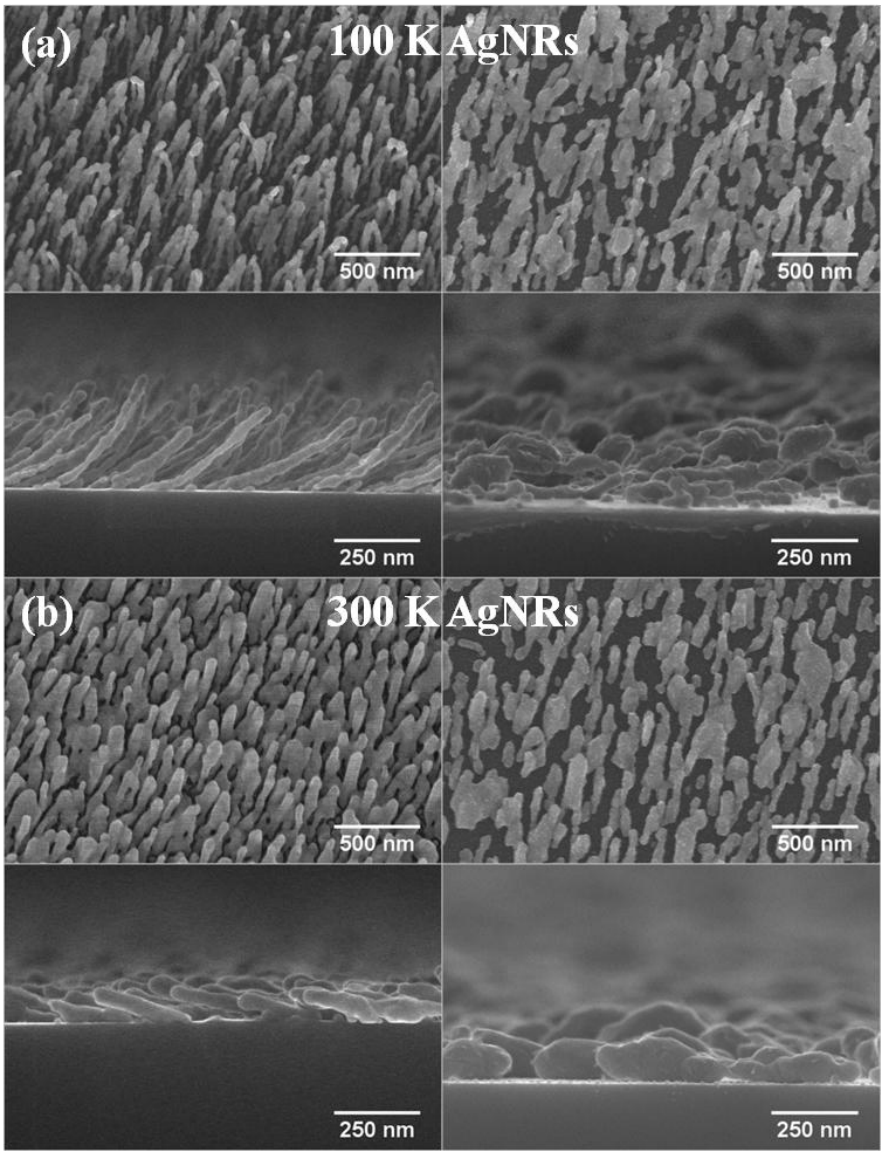

Figure 17 SEM images showing morphology of (a) 100 K AgNRs and (b) 300 K AgNRs pre (left column) and post (right column) incubation in R6G aqueous solution

Figure 17 shows the top and cross section SEM images of 100 K and 300 K AgNRs films prior- and post-incubation in the R6G aqueous solutions respectively. Morphological

differences were observed between the two AgNRs samples due to the reduction in surface diffusion and the mobility of adsorbed atoms on the substrate surface. A detailed explanation of this behavior is discussed in Chapter 2. These differences were quantified using Image J software by analyzing the SEM images and are discussed in Table 4, Chapter 2. These differences may influence magnitude of the SERS enhancement and the spatial performance of the SERS platforms.

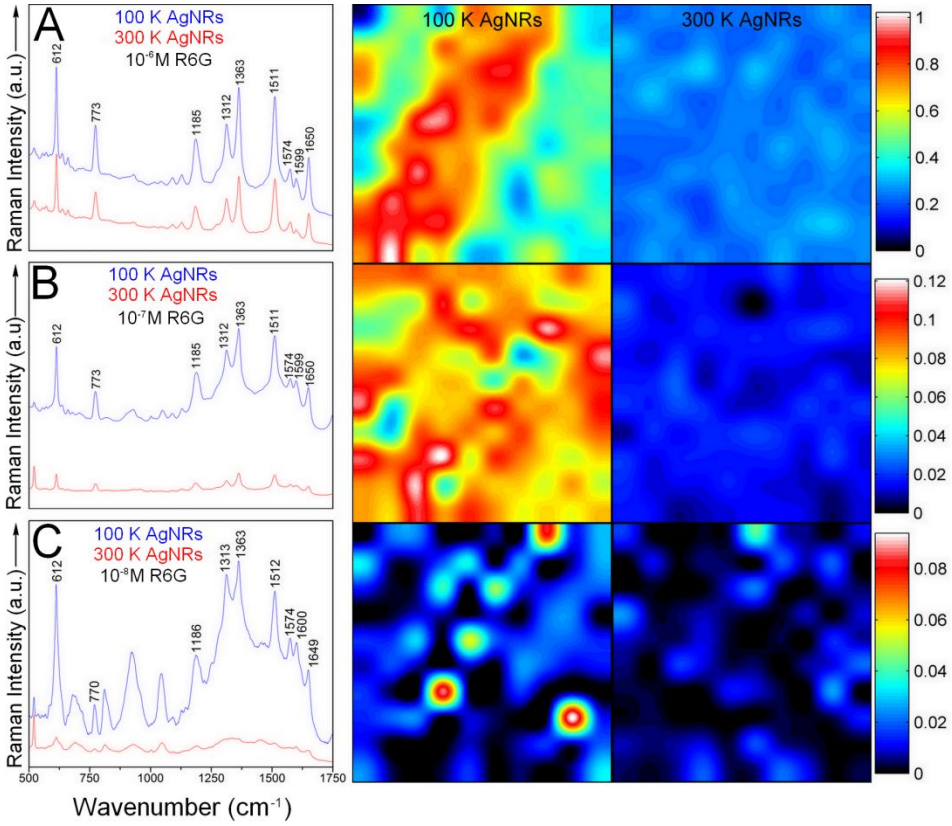

Figure 18 SERS images (Sample # 1) created using maps collected over 50 µm x 50 µm areas with 5 µm pixel size on post incubated 100 K and 300 K AgNRs samples. Incubation was done in R6G aqueous solution at different concentrations (A) 10^{-6} M (B) 10^{-7} M (C) 10^{-8} M

Figure 18 shows the SERS images (Sample # 1) that were collected from 50 µm x 50 µm random areas on the 100 K and 300 K AgNRs films after incubation with R6G at 10^{-6}, 10^{-7}, and 10^{-8} M. Similar SERS maps (Sample # 2) were obtained on a second set of AgNRs samples by exciting with the same laser line of 632.8 nm These results are shown in Figure 19.

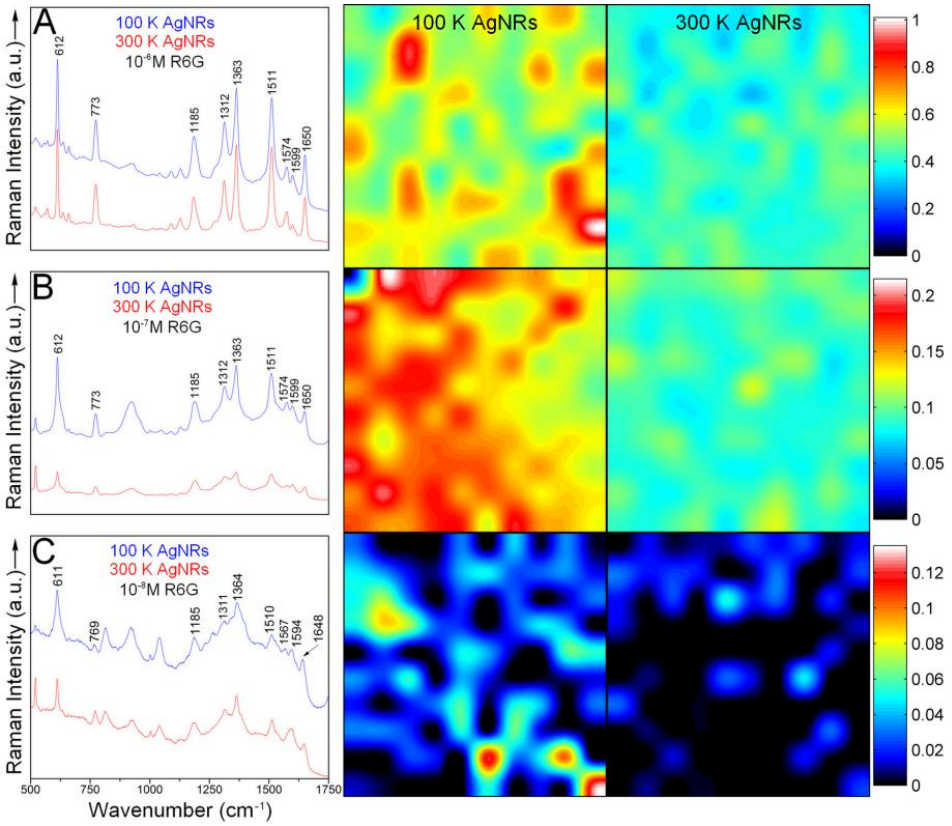

Figure 19 SERS images (Sample # 2) created using maps collected over 50 µm x 50 µm areas with 5 µm pixel size on post incubated 100 K and 300 K AgNRs samples. Incubation was done in R6G aqueous solution at different concentrations (A) 10^{-6} M (B) 10^{-7} M (C) 10^{-8} M

These images were created in MATLAB using the integrated area values of a base-line corrected R6G marker band, namely the xanthene breathing mode at 1625-1675 cm^{-1} [85]. Images were then color coded according to the integrated area values. White and red pixels (5 µm pixel size) in the SERS images correspond to large integrated area values of the xanthene band (*i.e.*, extremely active SERS regions), while the dark blue and black pixels are indicative of very small or zero integrated area values of the same peak (*i.e.*, regions of minimum or no SERS activity). For quantitative and qualitative comparisons, all SERS maps in Figure 18 and 19 were normalized with respect to the largest integrated area value within the maps, the acquisition time and the laser power.

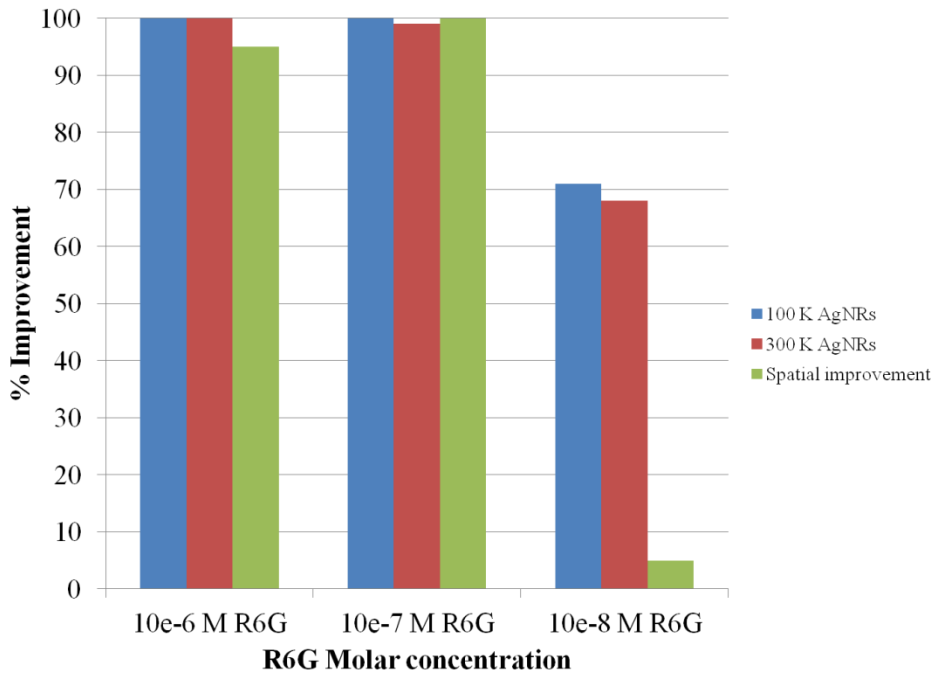

Figure 20 Plot showing % SERS active regions (shown in Figure 18) and % spatial improvement (green bar) in 100 K AgNRs (blue bar) over 300 K AgNRs (red bar) at different R6G concentrations

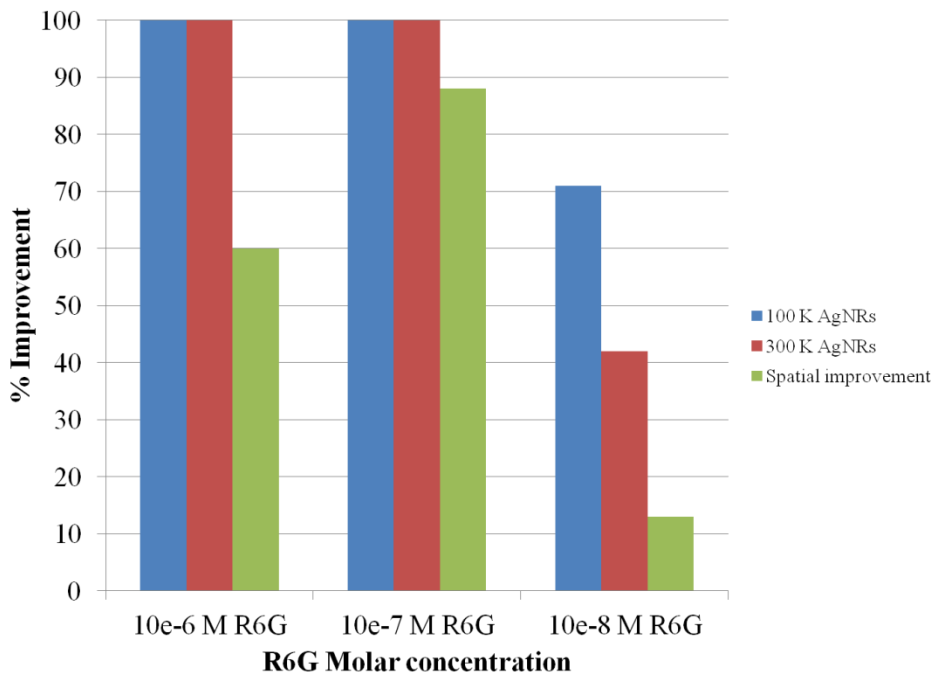

Figure 21 Plot showing % SERS active regions (shown in Figure 19) and % spatial improvement (green bar) in 100 K AgNRs (blue bar) over 300 K AgNRs (red bar) at different R6G concentrations

The qualitative examination of the normalized maps shows that the 100 K AgNRs film has significantly improved SERS-based sensing capabilities compared to the 300 K grown at all R6G concentrations. It shows that all map pixels were SERS active at 10^{-6} and 10^{-7} M of R6G for both the films. Figure 20 & 21 shows the spatial improvement in 100 K AgNRs films over 300 K. The cryogenically grown AgNRs film exhibited a percent spatial improvement in SERS signal of 95% and 100% at 10^{-6} M and 10^{-7} M of R6G, respectively. These values were estimated by determining the number of SERS pixels in the 100 K AgNRs map that possessed a greater integrated area than the maximum integrated area in the 300 K AgNRs map. Approximately 71% and 68% of the

total pixels were SERS active at 10^{-8} M of R6G in the 100 K and 300 K AgNRs maps, respectively. At this analyte concentration, the percent spatial improvement was estimated to be 5%. This is probably due to the small number of R6G molecules that are available at 10^{-8} M. At this concentration the R6G molecules are sparsely adsorbed on the surface of the 100 K AgNRs films and therefore majority of the pixels are either non-SERS active and weak response. This fact is evident in Figure 18 (C).

To quantify the overall percent increase in the signal for the 100 K AgNRs, the SERS active pixels of each map were averaged in MATLAB. The average SERS spectra are shown in Figure 18 for each R6G concentration. Compared to 300 K, 100 K AgNRs films were found to have an average signal enhancement of approximately 91, 445 and 411 % at different R6G concentrations respectively. The smaller increase in signal at 10^{-6} M (91 %) may be justified by the nanosurface saturation with R6G at 10^{-6} M

Several possible explanations justify the significant improvement in the SERS signal for the 100 K AgNRs. It was hypothesized that the higher density and larger surface area of the 100 K AgNRs would accommodate a greater number of R6G molecules. An additional contribution to the signal enhancement is associated with the permanent collapse of the AgNRs structures as a result of aqueous immersion and ambient drying. It is known that nanorods thin films exposed to liquids undergo permanent, structural changes (*e.g.*, Ag and SiO_2) [48 – 52, 57]. Both AgNRs films appeared uniform prior to immersion but had a different morphology during the acquisition of the SERS spectra, post-immersion (Figure 17). The 100 K AgNRs were more severely damaged than the 300 K AgNRs probably due to their fragile nature. The 100 K AgNRs are much thinner and longer than the 300 K AgNRs, and possess a steeper angle with respect to the silicon

substrate. As a result, the mechanical spring constant of individual 100 K AgNRs is much smaller compared to that of 300 K AgNRs. Therefore, the capillary forces associated with the high surface tension of water are likely to easily damage the 100 K AgNRs. The SEM images illustrated the random collapse of the 100 K AgNRs post-immersion. Numerous 100 K AgNRs were bundled together as a result of the structural damage and/or the aggregation promoted by the R6G analyte. Top view SEM images showed that the 100 K film was entirely covered with AgNRs prior to the immersion. However, exposed silicon areas were detected post-immersion in all substrates. The 100 K AgNRs had a greater polydispersity in size and shape than the 300 K AgNRs post-immersion. These factors may have also contributed to the large SERS enhancement due to the formation of several hot spots regions on the substrate. The 300 K AgNRs appeared semi-collapsed prior to incubation but better withstood the capillary forces due to the much thicker diameter, shorter lengths and more acute angle with respect to the silicon holder.

The Creighton synthesis is a common fabrication method for aqueous colloids of moderately polydispersed AgNPs (diameters of 1-140 nm) through the reduction of silver nitrate with sodium borohydride. It is widely-used in numerous SERS applications because of its low cost and simplicity. In this study, the SERS-based sensing capability of 100 K AgNRs films was compared to that of Creighton AgNPs (15.3 μg mL^{-1} of silver, average diameter of 10.4 nm) [74]. Synthesis and SERS characterization of AgNPs was done at Wright State University by Adam Stahler.

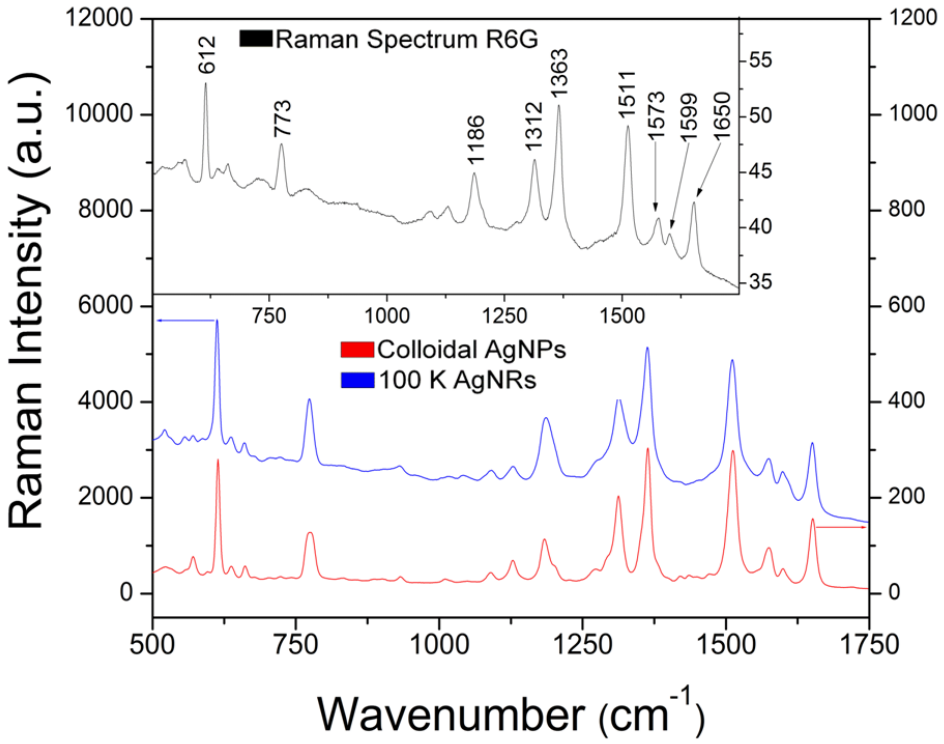

Figure 22 Comparison of SERS signals intensity of 15.3 ppm colloidal AgNPs (red) versus 100 K AgNRs (blue). Inset (black) shows Raman spectrum of 10^{-3} M R6G solution

Figure 22 shows the comparative SERS spectra. The average SERS signal from the 100 K AgNRs was found to be ~10-fold stronger than the one collected from AgNPs. At concentrations smaller than 10^{-6} M, SERS spectrum of good signal-to-noise ratio could not be measured on the AgNPs. Nevertheless, AgNPs and AgNRs have their own advantages and disadvantages. Colloidal AgNPs are one of the "cleanest" SERS substrates, for which air exposure and contamination may be minimized or eliminated. On the other hand, AgNRs films may be easily contaminated during ambient exposure. In fact, a few vibrational modes associated with organic impurities (*e.g.*, 813, 920, 1002, and 1040 cm^{-1}) were detected in the SERS spectra from both AgNRs at 10^{-8} M of R6G.

One of the most important requirements for versatile SERS substrates is the ability to detect low analyte concentrations in liquids as well as in vapor/gaseous form. AgNRs thin films have this potential but colloidal AgNPs are in general unsuitable for gas/vapor phase sensing.

3.4.2 Analysis of fluorescence emission spectra

The percent of R6G molecules adsorbed on the AgNRs substrates was estimated by calculating the percent difference of the fluorescence intensity of the R6G peak at 551 nm. Fluorescence intensity from the R6G solution prior to and post-immersion of the AgNRs thin was measured and the percent molecules adsorbed was calculated using equation 1

$$\%\ \text{R6G Adsorbed molecules} = \frac{\text{Intensity}_{\text{pre-immersion}} - \text{Intensity}_{\text{post-immersion}}}{\text{Intensity}_{\text{pre-immersion}}} \times 100\%$$

Eqn 1

The quenching in fluorescence intensity was due to the inability of R6G molecules to fluoresce because of their adsorption on the AgNRs surface.

After the R6G incubation of SERS substrates, optical image of the immersed AgNRs samples were acquired using Raman microscope. These images were used to determine the planar surface area of the substrates. This value and the morphological parameters of 100 K and 300 K AgNRs were used for the calculation of the total nanostructured Ag surface area available for R6G binding.

Figure 23 (left) shows the fluorescence spectra of 10^{-6} M R6G prior and post-immersion with 100 K AgNRs film samples of three different dimensions. A near linear increase (R^2 = 0.9401) was observed for the percent R6G molecules adsorbed on the AgNRs films with the increase in the total nanostructured surface area of the substrate (Figure 23, right). This method was duplicated for all R6G concentrations. This allows for the estimation of the percent R6G molecules adsorbed onto AgNRs at each concentration. The second set of AgNRs samples exhibited a larger degree of contamination than the

first set and resulted in larger deviations from linearity at 10^{-7} and 10^{-8} M of R6G. Contamination on the AgNRs substrates prevents R6G molecules to bind on its surface effectively.

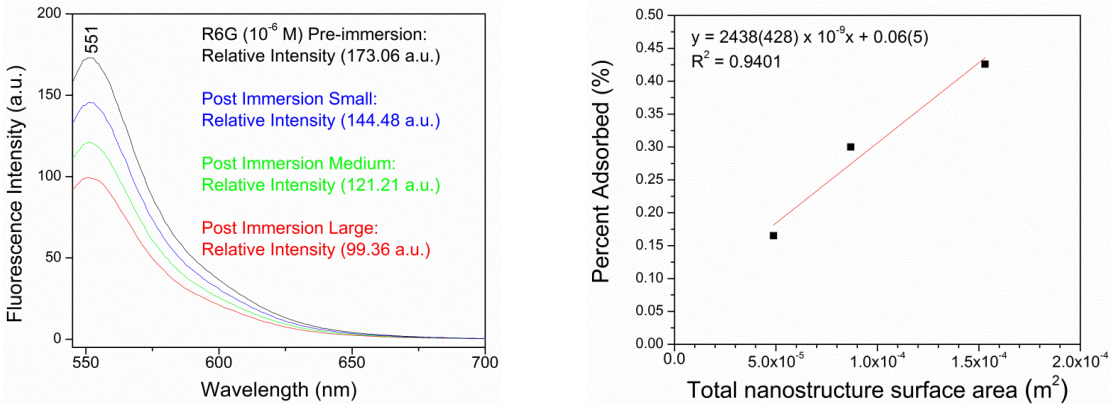

Figure 23 (Left) Fluorescence emission spectra of R6G aqueous solution (10^{-6} M) prior- and post-immersion of 100 K AgNRs substrates of three different dimensions (denoted small, medium and large). (Right) Percent R6G molecules adsorbed on the 100 K AgNRs films versus the total nanostructured surface area of each substrate.

Table 9 shows the average surface area of AgNRs samples and the percent of R6G molecules adsorbed onto these substrates (n = 6).

AgNRs Film	Surface Area (m^2)	Adsorption (%)
100 K AgNRs with R6G (10^{-6} M)	$(1.0 \pm 0.5) \times 10^{-4}$	29 ± 9
300 K AgNRs with R6G (10^{-6} M)	$(6.0 \pm 3.0) \times 10^{-5}$	25 ± 13
100 K AgNRs with R6G (10^{-7} M)	$(1.0 \pm 0.5) \times 10^{-4}$	45 ± 18
300 K AgNRs with R6G (10^{-7} M)	$(6.0 \pm 4.0) \times 10^{-5}$	41 ± 20
100 K AgNRs with R6G (10^{-8} M)	$(9.0 \pm 3.0) \times 10^{-5}$	84 ± 9
300 K AgNRs with R6G (10^{-8} M)	$(6.0 \pm 3.0) \times 10^{-5}$	73 ± 18

Table 9 Average surface area of AgNRs samples and the percent of R6G molecules adsorbed onto these substrates

3.4.3 Estimation of the SERS enhancement factors

SERS enhancement factors were calculated using the following formula:

$$SEF = \frac{\text{Int. Area}_{SERS}}{\text{Int. Area}_{Raman}} \times \frac{N_{Vol}}{N_{Surf}} \qquad \text{Eqn. 2}$$

Where N_{Vol} is the number of R6G molecules in the focal volume for the ordinary Raman measurement and N_{Surf} is the real number of molecules adsorbed on the SERS substrate and present under the laser beam. The focal volume (*FV*) was estimated by the equation [96].

$$FV = \pi \times \left(\frac{1.22 \times \lambda}{2 \times \text{N.A.}} \right)^2 \times \left(\frac{4 \times \lambda}{\text{N.A.}^2} \right) \qquad \text{Eqn. 3}$$

where *N.A.* is the numerical aperture and λ is the excitation wavelength. The $\left(\frac{1.22 \times \lambda}{\text{N.A.}} \right)$ term gives the waist diameter (0.965 μm) of the laser spot size. This resulted in a focal volume of ~1.896×10^{-17} m^3. The number of R6G molecules present in the focal volume during the Raman measurement of 10^{-3} M solution was estimated to be 1.14×10^7 (N_{vol}).

The total nanosurface area available for R6G binding was estimated by calculating the surface area of an individual rod as a cylinder having only the top exposed. This value was then multiplied by the density of rods per μm^2, and proportionally scaled to the laser spot size area.

The number of molecules adsorbed on the AgNRs surface (N_{Surf}) which are excited by the laser are estimated via fluorescence spectrophotometer measurements as discussed in the previous section. The planar area of the AgNRs substrate allowed for the

determination of the total nanostructured surface area, to which the calculated number of R6G molecules was bound. This value was then scaled to size area of the laser spot.

The SEFs as described in equation 2 were calculated using, the baseline corrected, integrated area values of the xanthene breathing mode (1625 cm^{-1} – 1675 cm^{-1}) in the Raman spectra of R6G (10^{-3}M) and the average SERS spectra. The SERS spectrum were normalized with respect to laser power and acquisition time.

The binding surface area of a R6G molecule was reported to be 222.0 Å by Gupta & Weimer and this allows for the estimation of percent layer coverage on the AgNRs [97]. Most prior literature that discusses SEF estimation typically assumes monolayer or sub-monolayer molecular coverage on the nanostructured surface area. Assuming lower molecular coverage than what the actual coverage is results in magnified values of SEF's. In this study we find that the coverage is far more than a monolayer especially for higher concentration R6G. Only at 10^{-8} M we start to get sub-monolayer coverage. Therefore the SEF's number appears smaller at 10^{-6} M than usually reported in literature. However we believe this method of estimation offers more realistic view of the SEF values.

	Sample # 1		Sample # 2	
	100 K	300 K	100 K	300 K
10^{-6} M	4.8×10^{2}	2.8×10^{2}	8.1×10^{2}	6.9×10^{2}
10^{-7} M	3.2×10^{2}	6.0×10^{2}	3.6×10^{2}	3.6×10^{2}
10^{-8} M	1.2×10^{4}	1.1×10^{3}	3.6×10^{3}	1.3×10^{3}

Table 10 Estimated SEF values on Sample # 1 and Sample # 2 at varying R6G concentrations

Table 10 shows the SEF's values for both samples. The SEF values of the Sample# 2 were similar to those obtained for the first set of samples at 10^{-6} and 10^{-7} M of R6G (> monolayer coverage). The SEFs (3.6×10^{2}) of the two substrates were identical at 10^{-7} M. This is probably due to the fact that the 100 K AgNRs film sample was ~45% smaller than the 300 K AgNRs sample, and resulted in a smaller total nanostructured surface area (*i.e.*, a much larger number of R6G molecules under the laser beam).

Chapter 4 SERS characterization – Vapor phase sensing

4.1 Introduction

The detection and identification of hazardous chemical and biological agents is important for several areas of national security as well as in manufacturing industries that deal with hazardous chemicals [30]. Gas chromatography has the advantage of providing quick and accurate detection capability; however cost, size and lack of portability in the field limits its widespread use [86]. Ion-mobility spectrometer is another popular technique for chemical sensing; however the level of information that can be extracted through this is not comparable to most vibrational spectroscopy techniques [87]. Surface enhanced Raman scattering (SERS) based techniques have shown the ability to detect the presence of low concentration of chemical agents quickly [22, 23]. Several papers have demonstrated a portable Raman probe setup for such chemical and bio sensing applications [32, 88]. Colloidal silver nanoparticles are commonly used as SERS substrates but they are only effective in detecting the presence of toxic chemicals in

liquids [79]. However, physical method such as the OAD technique for the growth of nanorods SERS substrate has the flexibility to detect toxins in liquid or vapor form.

In the previous chapter, we discussed the performance improvement of 100 K grown AgNRs over 300 K grown that were incubated in R6G aqueous solutions. Even though significant SERS signal intensity increased was observed in 100 K AgNRs, the morphology of the AgNRs is collapsed and altered post incubation. This behavior is partially attributed to the observed increase in SERS signal strength in 100 K AgNRs. Some of the earlier literature on SERS-based vapor sensing includes simulants for highly toxic chemicals such as nerve and mustard agents [88]. Most of these used electrochemically roughened silver oxide substrates or silver film over nanosphere substrates. Such substrate synthesis and fabrication methods result in SERS substrates that are limited by the available surface area of silver for the vapor molecules to bind and adsorb on to. On the other hand, nanorods thin films based substrates offer significantly greater surface area and scalability.

Therefore the aim of this preliminary investigation is to study the use of AgNRs based SERS substrates to detect an effective Raman scatterer molecule (4-aminobenzenthiol (4-ABT)) that is vapor deposited on the surface of AgNRs. This process of detecting the presence of analyte molecules on AgNRs substrates simulates vapor phase sensing capabilities of AgNRs based SERS substrates. Furthermore, SERS performance of 100 K and 300 K AgNRs is also compared using a chemical warfare agent simulant 2-chloroethyl ethyl sulfide (half-mustard agent**,** CEES) in vapor form. Results indicate significantly higher detection sensitivity of 100 K grown AgNRs.

4.2 Experimental details

4.2.1 Vapor phase incubation using 4-ABT

4-ABT molecule has sulphur component which binds very effectively with the silver surface. The molecule is highly volatile due to the presence of thiol and amino groups. In the exposure setup shown in Figure 24, approximately 10 milligrams powder of 4-ABT was loaded in a 10 ml glass beaker. A microscope glass slide with double sided tape was used to attach the AgNRs samples. A plain untreated silicon sample was also incubated with the 4-ABT vapor as the background control sample. The samples were incubated for different time periods to vary the concentration of the vapor being deposited on the substrate. Due of the sensitivity of the 4-ABT molecule to the ambient moisture, the incubation was done in a glove box setup which was purged three times with high purity N_2 prior to exposure of samples. The samples were exposed to the 4-ABT vapor for different times starting with 60 min exposure followed by 30, 20 and 5 min exposure.

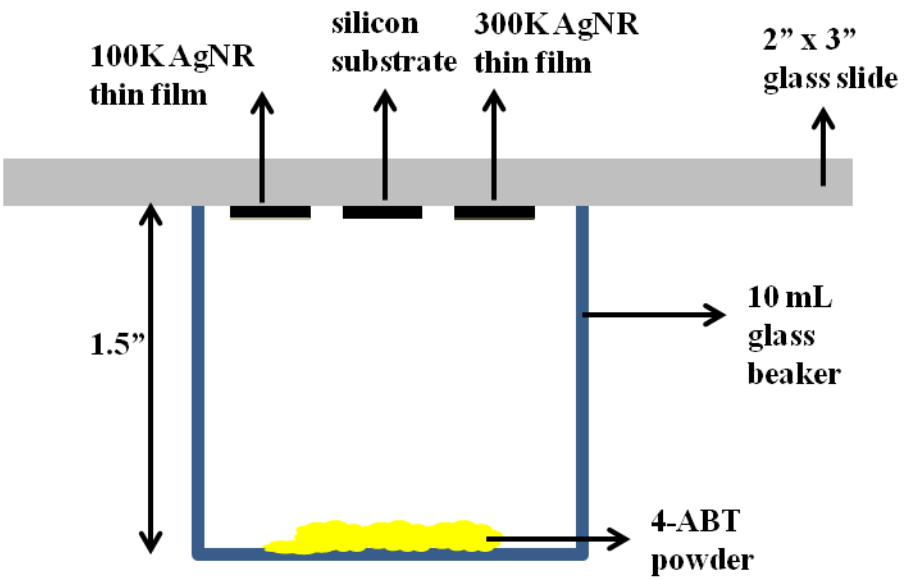

Figure 24 Schematic showing experimental setup for SERS vapor sensing study

4.2.2 Vapor phase incubation using CEES vapors

Similar to 4-ABT vapor exposure setup, AgNRs samples were adhered to a glass microscope slide, which was placed on top of a 10 mL beaker containing 1 mL of half-mustard (98%, Sigma Aldrich). All AgNRs were facing half-mustard vapor source at a distance of approximately 25 mm. The samples were exposed to CEES vapor for different times starting with 20, 40 and 60 min.

4.2.3 Micro-Raman and SERS measurements

Raman and SERS spectra were obtained using a LabRamHR 800 system (Horiba Jobin Yvon Inc.) and the LabSpec v.5 software. A 632.8 nm HeNe laser was used as the excitation source and the confocal hole was set at 300 μm. The backscattered Raman and

SERS signals were collected using thermo-electric cooled CCD detector. The focused laser beam spot size on the sample surface was about 1 μm in diameter. Under these experimental conditions, the spectral resolution was about 1 cm^{-1}. The optimized parameters were 5 s acquisition time and signal averaging over 3 cycles using Olympus objective (100x). This ensured acquired spectra with adequate signal to noise ratio. SERS spectra at random locations were collected across the AgNRs substrates exposed to 4-ABT vapors for different time periods. Similarly following the vapor deposition of half-mustard, three SERS spectra were collected at random locations on each AgNR substrate and then averaged. The optimized acquisition parameters were as 2 s acquisition time and 3 cycles. The Raman spectra of neat half-mustard was also collected in a quartz cuvette using the same acquisition parameters as for the AgNRs substrates with the exception of laser power (15 mW instead of 0.015 mW) and objective (50x instead of 100x). No ordinary Raman spectra of good signal-to-noise ratio could be recorded from the 10^{-1} M solution of half-mustard. All data was collected using the LabRam HR800 associated LabSpec v.5 software.

4.3 Results and discussion

Figure 25 shows the SERS spectra collected from 100 K and 300 K AgNRs that were incubated with 4-ABT vapor for 5, 20, 30 and 60 minutes.

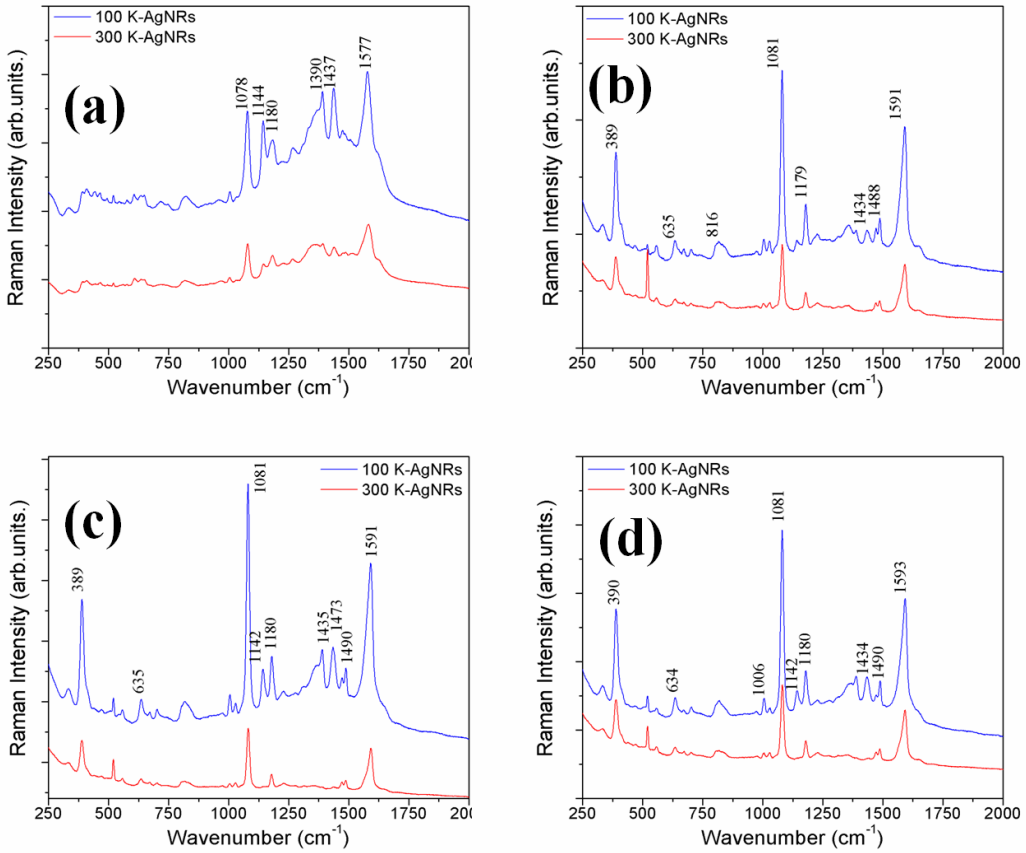

Figure 25 SERS spectrum shows the presence of 4-ABT molecule on 100 K and 300 K AgNRs which were incubated for different exposure times (a) 5 min. (b) 20 min. (c) 30 min. (d) 60 min.

It is clear that 4-ABT vapor was detected for all exposure times and the SERS signal intensities from 100 K AgNRs is significantly larger than 300 K AgNRs. During the sample incubation with 4-ABT vapor, plain silicon substrate was also incubated

concurrently with the AgNRs samples. Raman spectra from the silicon sample showed no presence of 4-ABT molecules. The key difference observed between the AgNRs at 100 K and 300 K is the ability to resolve and detect all representative 4-ABT peaks. For AgNRs samples that were exposed for 30 and 60 minutes, it appears that the SERS spectra from 100 K AgNRs is able to distinctly resolve a higher number of 4-ABT peaks. This behavior may be explained by the difference in morphology of 100 K and 300 K AgNRs. For 100 K AgNRs, the physical structure of the individual high aspect ratio nanocolumns may allow the 4-ABT molecules to adsorb with certain molecular orientation and lead to resolving the molecular bonding more effectively compared to 300 K AgNRs. On the contrary, collapsed structure of 300 K AgNRs may only allow the molecules to adsorb in a fixed orientation and therefore only certain peaks are resolved. The SERS signal for 5 minutes exposed sample appears higher and has shown a different baseline compared to 20, 30, and 60 minutes exposure samples. This is possibly due to the molecule degradation or reactivity with the ambient prior to adsorption on the AgNRs surface. In the current study, samples were exposed for 60 minutes first followed by 30, 20 and 5 minutes exposure period. During this time, 4-ABT powder in the beaker may have reacted with the ambient dry N_2 in the glove box. Based on this observation, it would be best to incubate AgNRs samples concurrently in different beakers with the same amount of 4-ABT powder for different exposure time. Such setup would eliminate the effect of degradation or reactivity of the molecule prior to adsorption on the substrate. Considering the minimal interference of organic impurities on the AgNRs substrates, 1080 SERS peak was chosen as the 4-ABT representative peak to compare the integrated area intensities.

Figure 26 shows the % improvement in 100 K AgNRs over 300 K AgNRs based on the integrated area values of baseline corrected1080 peaks.

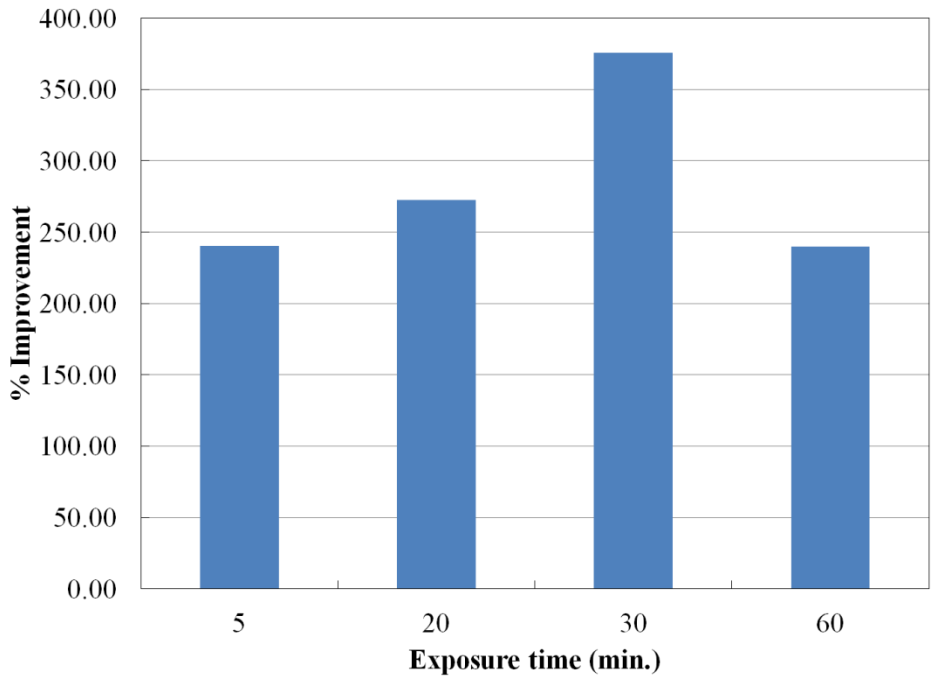

Figure 26 Percentage improvement in SERS signal intensity of 100 K AgNRs over 300 K AgNRs incubated with 4-ABT molecules for different exposure times

An average of 250 % improvement is measured across all AgNRs substrates. We believe these results have shown the potential for using AgNRs based SERS substrates for hazardous gas and chemical agent sensing in vapor phase.

Figure 27 shows the SERS spectra after AgNRs exposure with CEES vapor for varying times.

CEES is considered as the simulant for the mustard gas which is considered as a chemical warfare agent. Ability to detect the presence of this agent at extremely low concentration is beneficial. In the current study we have the shown comparative results of

two AgNRs thin films for CEES vapor sensing. Results indicate superior detection sensitivity of 100 K AgNRs than 300 K AgNRs. Even after 20 min. exposure time, strong spectral response is observed from the 100 K grown SERS substrates. Like observed in 4-ABT response shown in Figure 25, 100 K AgNRs is able to distinctly resolve most peaks representing CEES. Based on these two observations, we believe even 100 K AgNRs substrates may be able to detect CEES presence even after shorter than 20 min. exposure times.

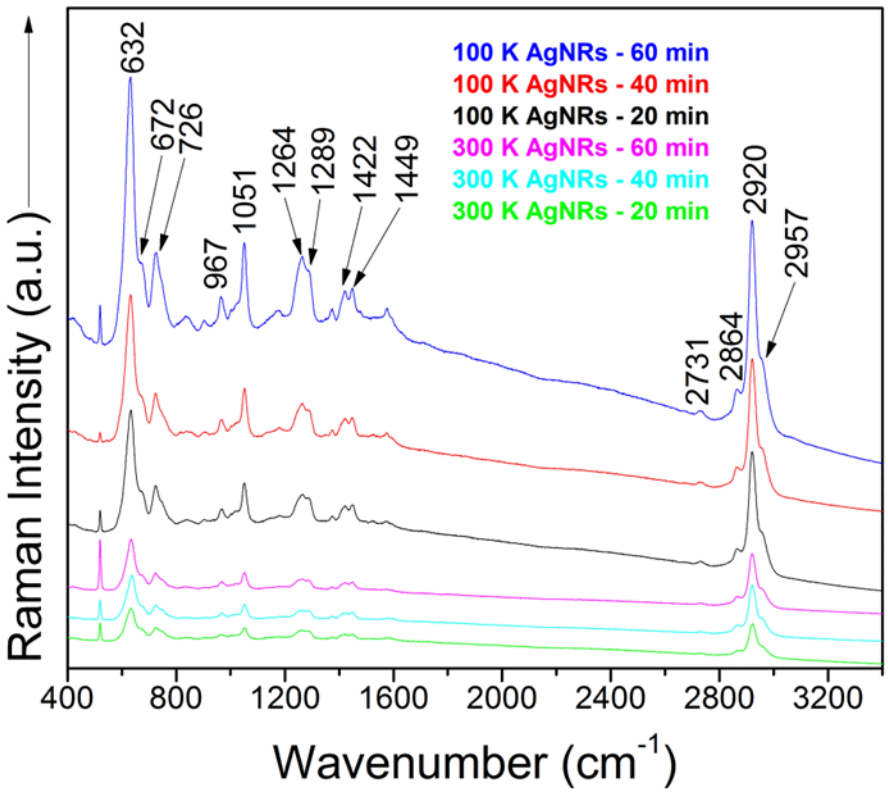

Figure 27 SERS spectra from 100 (blue, red, black) and 300 K (pink, cyan, green) AgNRs thin films after exposure with CEES vapor for varying times

Chapter 5 Effects of liquids exposure on nanorods thin films

5.1 Introduction

Nanostructured thin films with columnar, zig-zag, helical and straight nanorods [3, 5] have been extensively discussed in the literature for their novel electrical [89], magnetic [90], and optical properties [10, 11]. The high surface area of these films provides a conducive platform for chemical, biological and environmental sensing applications including electrodes for fuel cells [45 – 47]. It has, however, been noted that these films, especially high aspect ratio nanocolumns are easily deformed after exposure to liquids or moist environments [48 - 52]. This is due to the high capillary forces acting between neighboring nanocolumns which collapse the structures during the drying process. The capillary pressure acting on the nanorods depends on the surface tension of the fluid and the spacing between the nanorods [48]. However, wet processing is an inevitable step in most lithographic patterning. If STF are to be successfully used in practical devices, techniques need to be developed to allow them to withstand wet processes. This aspect has been previously recognized by several authors [91, 92].

Lau et al. [93] shows that even one drop of DI water permanently alters the structure of carbon nanotube (CNT) arrays. Zhao et al. have studied the effects of DI water on the structure of tilted, straight, helical and zig-zag nanocolumns STFs [48]. Their study found that tilted nanorods were the most stable structure compared to zig-zags and helices, and straight-up vertical nanorods were found to be the most susceptible ranging from complete collapse to small changes in their physical structure. In order to overcome the so called "nanocarpet effect" (film with clusters of nanorods), they recommended depositing an additional thin film of the same material above the STF at close to normal incidence (non-glancing angle) [48]. The idea behind this approach is to limit the spacing between the nanorods to prevent large bending. This method does improve the film's ability to withstand wet processing, but adding an extra layer on top compromises some of the inherent characteristics of the STF such as porosity and anisotropy. Also the use of this method is limited to straight-up/vertical nanorods. With tilted, zig-zags, or helical structures the near normal incident deposition will not reach the cavities near the surface of the substrate. Attempts have also been made to understand the nature of collapse or bundling of straight Si nanorods [51] with respect to their location from the water droplet's center. Kupsta et al., has suggested a completely different approach using a crack free capping layer film to prevent liquid penetration [91]. Again, additional deposition of normal incidence thin films without any known technique to subsequently remove such thin films will over shadow the benefits of anisotropic properties of nanostructured thin films. It has also been shown that ion-milling the STF after liquids exposure will reduce the clustering of columnar thin films [92].

On the other hand, it has been shown that silane treated Si nanorods with induced nanocarpet effect increases the hydrophobicity due to the reduced solid-liquid contact [93]. Tsoi et al. [94] discuss liquid and vapor phase silane functionalization of SiO_2 and TiO_2 spiral STF in dry toluene solution and silane solution followed by immersion in acetone, followed by annealing at room temperature. The results of this study don't seem to affect the physical structure of the STF even after liquid phase functionalization. Overall, most of these techniques do not address or propose engineering solutions to prevent the collapse or bundling of nanorod thin films in liquid environments without permanently modifying the film structure in some way. Detailed understanding of the extent of liquid effects is also important in developing engineering solutions to this problem which has been provided by Fan et al. [48].

In this work we have studied SiO_2 tilted nanorods thin films in two different solvents (ethanol and acetone) for comparing the effect of evaporative room temperature drying and CO_2 critical point drying. Acetone is a common chemical solvent used in photolithography to strip photo resist and also for lift-off processes. Ethanol is another common cleaning solvent and transitional fluids used in critical point dryers. Hence these were chosen as representatives for our study. The results of our study indicate that CO_2 critical point drying can be used to prevent these thin films from permanent collapse after exposure to liquids. Critical point drying was originally developed for drying biological samples but was later successfully adapted for MEMS structures to prevent stiction related issues. Jafri et al. [95] have provided an extensive overview of stiction related issues in MEMS devices and techniques to mitigate them including CO_2 critical point drying. Despite the large number of publications on the subject of STF wet exposure to

the best of our knowledge no one has suggested or demonstrated the use of CPD to overcome this problem. We show that CPD can be a viable alternative to capping or filling protective films on STFs, and could present a step forward to enable conventional photolithographic processing of nanostructured thin films.

5.2 Experimental details

5.2.1 Fabrication of SiO_2 nanorods thin films

All of our depositions were done using an MDC evap-4000 e-beam evaporator in a vacuum chamber designed by Torr International. This is a generic evaporation chamber, and is not equipped with any substrate angle or motion controller. The sample holder consists of pre-calibrated miniature hinges on which the samples are mounted. Figure 28 shows the construction of the sample holder.

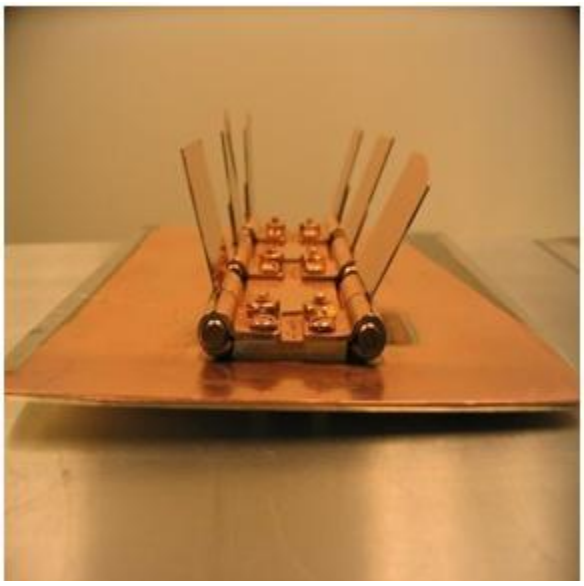

Figure 28 Custom designed sample holder hinge fixture for OAD technique

Different angles can be set by adjusting the hinges using precise angle blocks calibrated to the center of the vapor source from the sample. The e-beam source to the substrate distance is 0.5 meter. Prime grade silicon <100> wafers cleaned with acetone, methanol and IPA were used in all depositions. The SiO_2 evaporation pellets were 99.99 % purity and the chamber base pressure was < 66.10^{-6} Pa (~ $0.5x10^{-6}$ Torr). The deposition angle at the sample was set between 84° to 86° for all samples. After the initial film conditioning

ramp, the deposition rate was maintained at 0.3 nm s^{-1} using the Sigma SQC-310 thin film deposition controller.

5.2.2 Liquids exposure with SiO_2 nanorods thin films

The solvents used in this study were all semiconductor (electronic) grade, and no effort was undertaken to remove the residual moisture contents from the solvents. For studying the effect of ethanol, the SiO_2 STF sample was cleaved into three pieces to compare the original film with room temperature (RT) evaporation dried and critical point dried samples. A few drops of solvent was placed on the sample using a pipette, and allowed to evaporate and dry at room temperature (22°C, 15%-20% RH). Ethanol was used as the transitional fluid in the CO_2 critical point dryer (model # AutoSamdri – 814B from Tousimis Corporation). Conventional CPD processing cycle was followed which included 30 minutes of solvent purge with liquid CO_2 at low temperature and high pressure (< -5°C, 5.51 MPa). Subsequently after the purge cycle, temperature and pressure of the reactor chamber was allowed to exceed the critical point of CO_2 which is 7.38 MPa and 31.1°C. Once the pressure and temperature were above the critical point, the chamber was vented at the rate of 0.68 MPa $minute^{-1}$. Similarly another SiO_2 STF sample was cleaved into three pieces and used with acetone instead of ethanol.

5.2.3 SEM and image analysis

Scanning electron microscope (SEM) images were acquired using a Hitachi S-4800 high resolution SEM for cross sectional and top views. To avoid electron charging effects, the samples were sputter coated with an ultra thin layer of Au before SEM imaging. Subsequently SEM images were subjected to quantitative image processing. Two-dimensional (2D) power spectra of the SEM top view images were studied in order to quantify the clustering effect of the STF samples. Assuming a circular symmetry of the STF texture, radially averaged power spectral density (PSD) can be utilized for quantitatively analyzing the clustering effect. Even though the circular symmetry assumption hides some orientation effects due to the growth direction of the nanorods, the radial average is still sufficient to study the general trends of the topographic changes, which was the main interest in this study. The top view images are first level-set to black and white to separate the lateral information from the height information [10]. After converting the normalized 2D power spectrum from Cartesian coordinate to polar coordinate, radially averaged PSD can be generated as power versus *k*, where

$$k_{max} = 2\pi.R^{-1}$$

R is the resolution of an image which is the dimension of a single pixel. In all these images, *R* equals to 10 nm.

5.3 Results and discussion

Figures 29 and 30 show the effect of ethanol and acetone exposure. The film thickness for the ethanol study was 500 nm, and for acetone it was ~1 μm.

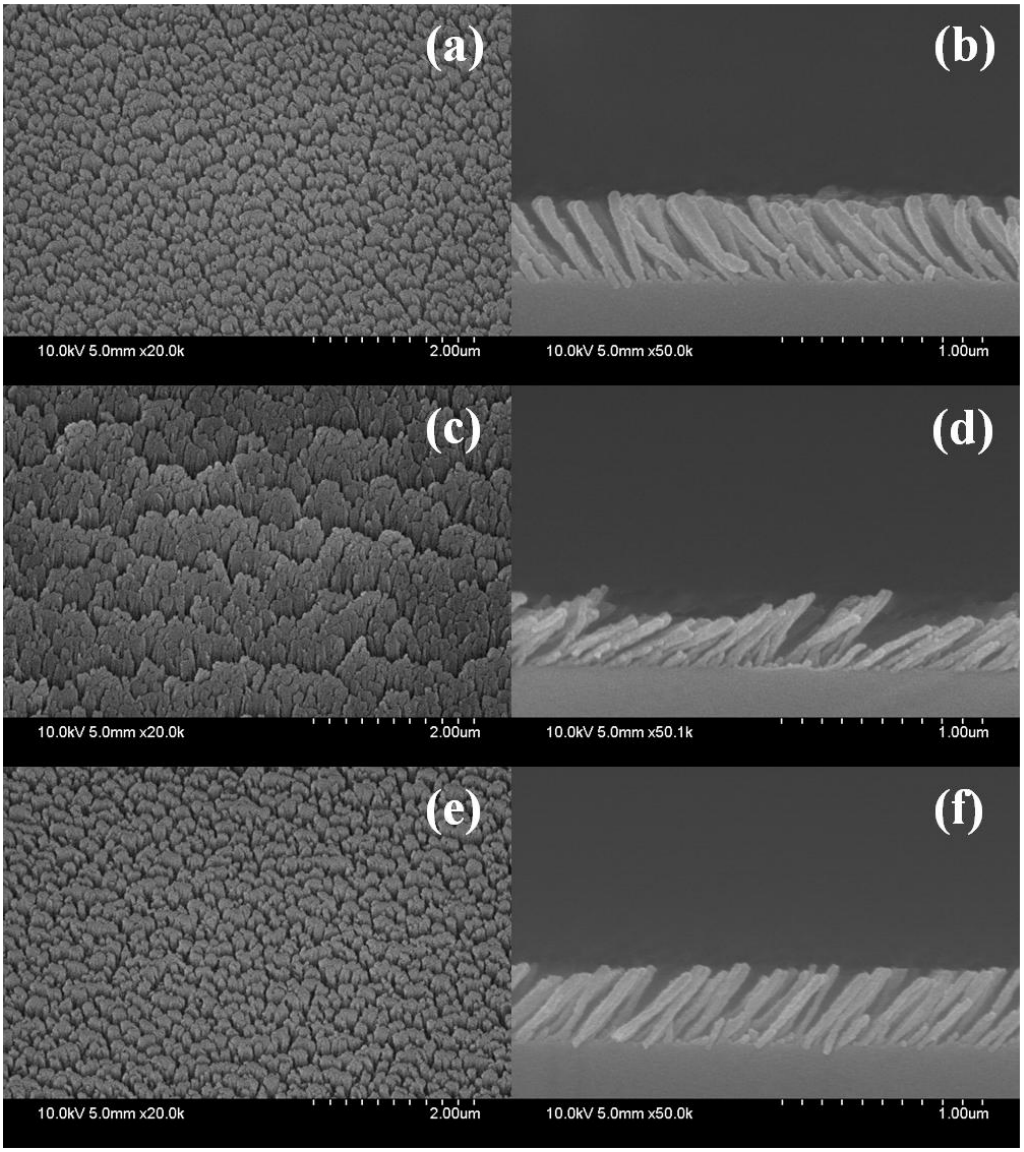

Figure 29 Top view and side view SEM results from ethanol treatment (a) untreated as grown top view (b) untreated as grown side view (c) ethanol treated RT dry top view (d) ethanol treated RT dry side view (e) ethanol treated CO_2 dry top view (f) ethanol treated CO_2 dry side view

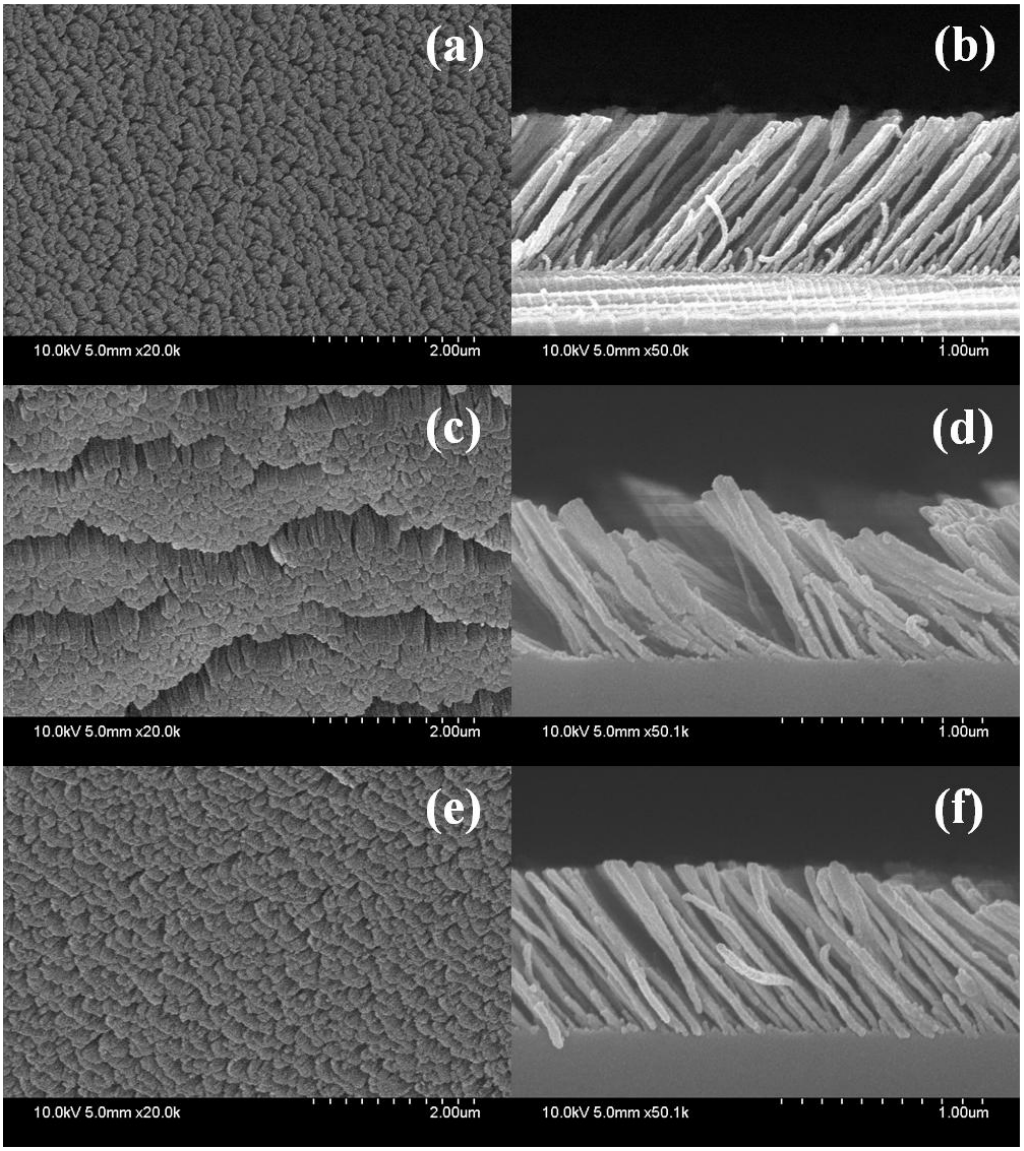

Figure 30 Top view and side view SEM results from acetone treatment (a) untreated as grown top view (b) untreated as grown sideview (c) acetone treated RT dry top view (d) acetone treated RT dry side view (e) acetone treated CO_2 dry top view (f) acetone treated CO_2 dry side view

It is clear from the side view and top view images that evaporative drying at RT causes the STF to collapse permanently. They exhibit bundling or clumping in the lateral axis and a change in the average tilt angle of the nanorods compared to the original samples,

which are consistent with the results reported by others. Table 11 shows the surface tension of fluids commonly used in photo resist based conventional lithographic methods.

Solvent/Liquid	Surface Tension (dynes/cm)
Water	72.8
Acetone	23.32
Methanol	22.55
Ethanol	22.32
Isopropyl Alcohol	21.79

Table 11 Surface tension of commonly used fluids in photo resist based conventional lithographic methods

The nanorods are subjected to considerable forces which are dominant at the phase boundary as the liquid evaporates at room temperature. These effects are more severe in water than in ethanol or acetone since water has the highest surface tensions of the three liquids examined here. Figure 31 shows the effect of a DI water droplet evaporation dried at room temperature. This was taken from the same sample fabricated for the ethanol study. The top and side views in Figure 31 confirm near complete collapse of the nanorod structures compared to the ones treated with ethanol and acetone. The nominal moisture content in the solvent could potentially play a minor role in the nanorods

collapse but the results are still representative of what would be encountered during conventional lithographic processes.

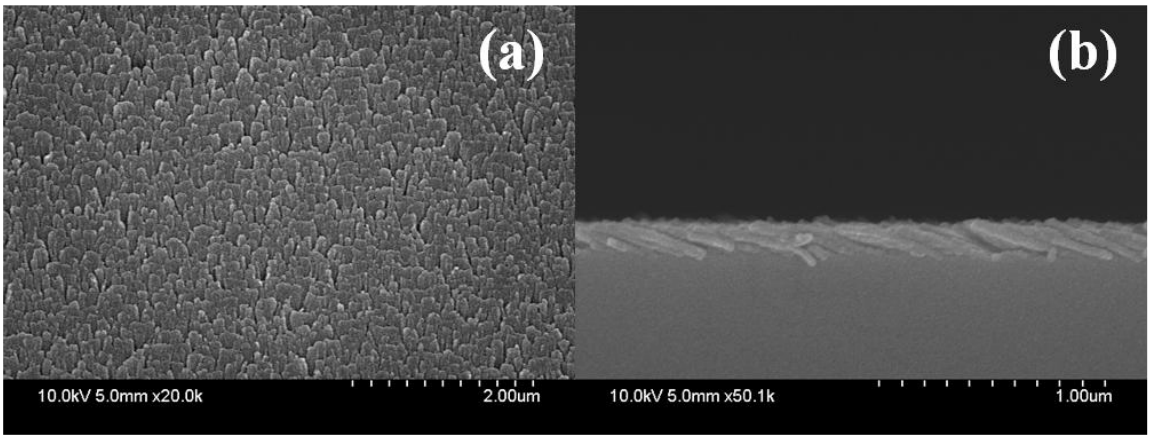

Figure 31 Top view and side view SEM results from water treatment (a) water treated RT dry top view (b) water treated RT dry side view

In critical point drying, as the temperature of the chamber is raised to its critical temperature, the liquefied CO_2's meniscus becomes flatter indicating reduction of its surface tension. At the critical point in temperature and pressure, the liquid will change its state to gas without a change in surface tension, hence eliminating any damage to the sample during the drying process. This is a well understood process, but to the best of our knowledge has never been applied to STFs to overcome the film collapse problem.

Comparing the top and side views of as-grown and CO_2 dried samples individually for ethanol and acetone exposure, it is clear that the CO_2 preserves the physical structure of the STF to a significant extent. The radially averaged PSD of the ethanol treated and acetone treated samples are shown in Figures 32 and 33 respectively.

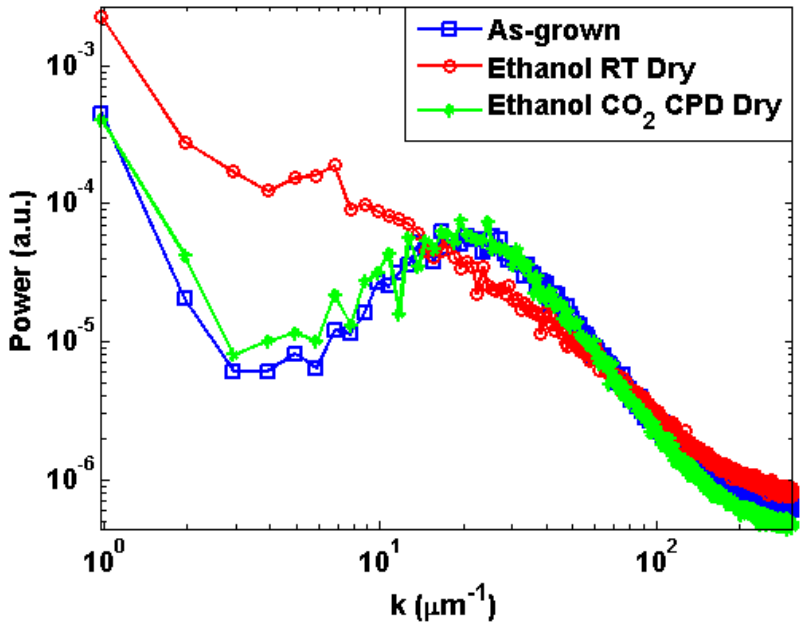

Figure 32 Radially averaged PSD from binary top view SEM image of ethanol series samples.

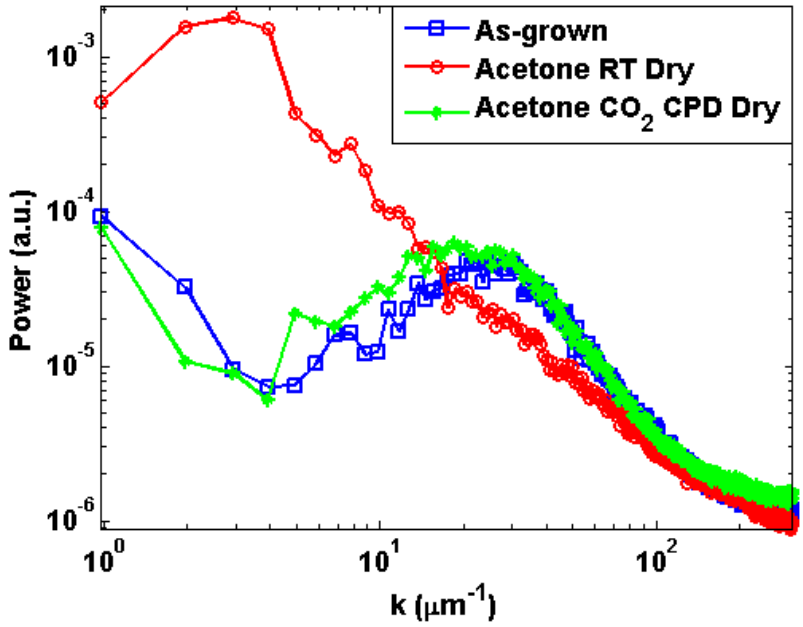

Figure 33 Radially averaged PSD from binary top view SEM image of acetone series samples.

For both sets of samples the radially averaged PSD of the CO_2 dried samples are very similar to the original samples. On the other hand, the RT dried samples show very different results for $k < 100\ \mu m^{-1}$. The major differences occur around $k = 3\ \mu m^{-1}$and around $k = 25\ \mu m^{-1}$. For the original and CO_2 dried samples, a peak appears around $k = 25\ \mu m^{-1}$, which corresponds to a characteristic length of around 250 nm. By examining the higher magnification images, we find that this corresponds well to the dimension of the nanorod clusters. For k around $3\ \mu m^{-1}$ the PSD of RT dried samples are much larger than the as-grown and CO_2 dried samples. This is due to the appearance of clusters of a much larger length scale rather than separated nanorods, which is around a micron in size.

Photolithography is a key process step used in semiconductor and MEMS manufacturing for integrated circuits (IC's) and other electronic devices. In order to establish STF's use in practical devices, ability to lithographically pattern STF would be important. Figure 34 shows the process flow for patterning standard normal incidence thin films. The two common ways to pattern normal incidence thin films are etch down process and the lift off process. As indicated in the process flow schematic, etch down process involves more number of wet processing steps and it is not possible to decouple the thin films exposure with liquids (DI water, solvents, photoresist developer etc.). The steps that involve wet processing includes spin coating photo resist, develop exposed photoresist, wet or drying etching of thin film, removal of photo resist and final rinse with solvents. Typically for a standard normal incidence thin film, liquid exposure will not be an issue. However for STF with delicate physical structure, the properties and morphology of thin film permanently changes after exposure with liquids as shown in Figure 29, 30 and 31. Compared to etch down approach, we believe lift-off process is

best suited for patterning STF, since it has only one processing step that involves exposure of thin film with liquids for the removal of photo resist. In combination with CO_2 CPD technique, wet lift-off process would possibly be one of the potential techniques to pattern nanorods thin film.

In many lithography applications a DI water rinse and drying is the terminal step. In these cases, a special water washout procedure to ensure removal of DI water from the surface could be performed before carrying out the CO_2 dryer with ethanol or acetone as the transitional fluid. The transitional fluid and water should be miscible fluids, and the sample has to be transferred to the transitional fluid without allowing it to dry in air.

Chapter 6 Dry lift-off based nanorods thin films patterning

6.1 Introduction

In the previous section we discussed how the physical structure and morphology of nanorods thin films can be preserved after liquids exposure using CO_2 CPD technique. This essentially is a key requirement for application of conventional lithographic processing techniques to nanorods thin films because it involves exposure of thin films to liquids.

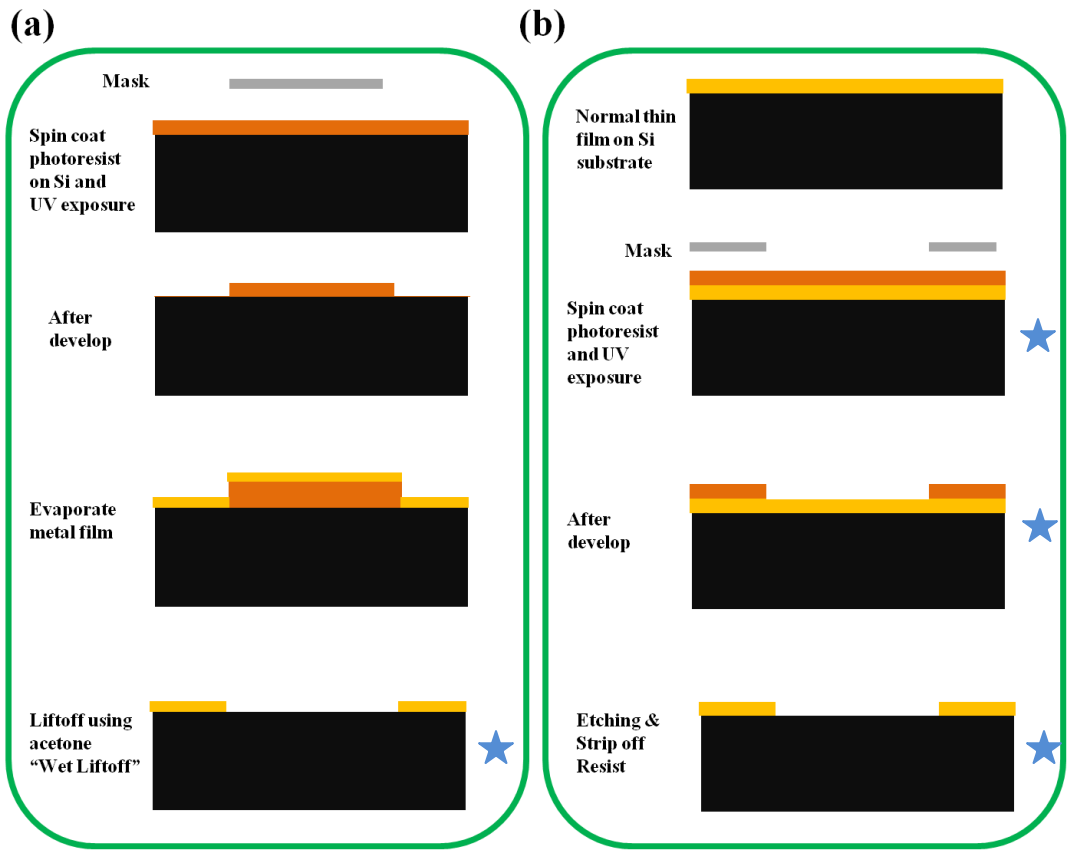

Figure 34 Schematic showing conventional lithographic processing techniques (a) lift-off process (b) etch down process

Photolithography is a key process step used in semiconductor and MEMS manufacturing for most integrated circuits (IC's) and other electronic devices. Figure 34 shows the process flow for patterning standard normal incidence thin films. The two common ways to pattern normal incidence thin films are the etch down process and the lift off process. As shown in the schematic, most steps involve wet processing (★ indicates wet processing step) and it is inevitable to prevent the thin films exposure with liquids (DI water, solvents etc.). Typically for a standard normal incidence thin film, films contact with liquids will not be an issue. However for nanorods thin films the properties and morphology of thin film permanently changes after exposure with liquids as shown and

discussed in Chapter 5. Compared to the etch down approach, lift off process has the least number of steps that involves films contact with liquids. As shown in Figure 34 (a), except for the last liftoff step for the removal of photoresist using acetone, no other step involves wet processing. Therefore for patterning nanorods thin films, lift-off process is more suitable. In combination with CO_2 CPD technique, wet lift-off process could possibly be one of the potential techniques to pattern nanorods thin film. Even though CPD based drying technique have shown to work with such solvents in preserving the physical structure of STF's, it requires an additional processing step which takes approximately 45-60 min. per drying cycle. Alternatively another technique which would be effective for patterning nanorods thin films is based on the dry removal of the sacrificial layer during the lift-off process. This process is called as dry liftoff. Dry liftoff process was earlier reported for patterning biological cells and organisms on substrates [98 - 100]. However its use for patterning thin films has not been discussed in prior literature. Unlike the use of photo resist stripper or acetone solvent that is used in the wet liftoff process, the dry liftoff process doesn't require use of any solvents or liquids for the removal of sacrificial layer. The sacrificial layer would be mechanically peeled off from the substrate, leaving the patterned areas undisturbed. For patterning nanorods thin films using this technique; following requirements on the sacrificial layer would ensure effective patterning of such thin films.

1. Clean removal
    a. Clean removal or peel off of the sacrificial film with minimal or no residue remaining on the substrate
2. Low thickness of spin coated sacrificial layer

a. Figure 35 shows the effect of sacrificial layer thickness on the shadow distance during the deposition of nanorods thin film. To minimize the dead zone in patterning STF's, it is imperative to minimize the thickness of the sacrificial film. Red areas in the figure indicates the areas where nanorods thin films growth is prevented since this area falls in the shadow of sacrificial layer (blue)

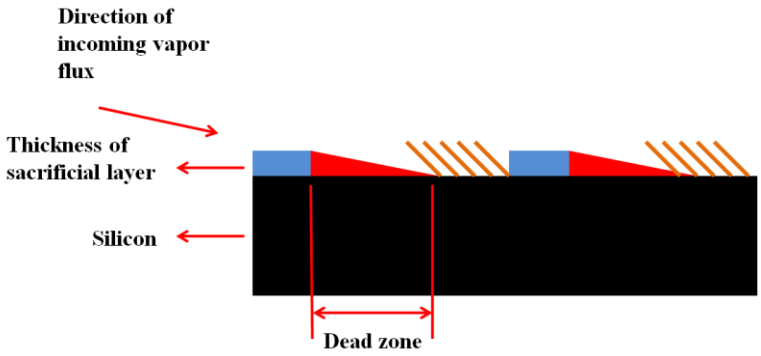

Figure 35 Schematic showing the effect of thickness of peelable polymer on dead zone

3. Mechanical strength
    a. Sacrificial film should offer enough mechanical strength for the film to peel off with ease without breaking and cracking
4. Conformal coating
    a. Uniformity in thickness and conformal coverage is required to ensure repeatable patterning

6.2 Experimental details

A UV curable acrylate based peelable polymer (Deco-Chem D-11843) is used as the sacrificial film for this study. The viscosity of the polymer was reduced by adding 2 % wt. Isopropyl alcohol. The reduced viscosity ensures thinner peelable films. Higher sacrificial layer thickness combined with steeper OAD angle will increase the dead zone area and therefore limit the usable patterned area on the substrate. The polymer is negative acting, which means during the UV exposure through a photo-mask, exposed areas will cross link and remain while the unexposed areas can be rinsed away. Figure 36 shows the process schematic for peelable polymer based dry lift off process for patterning nanorods thin films.

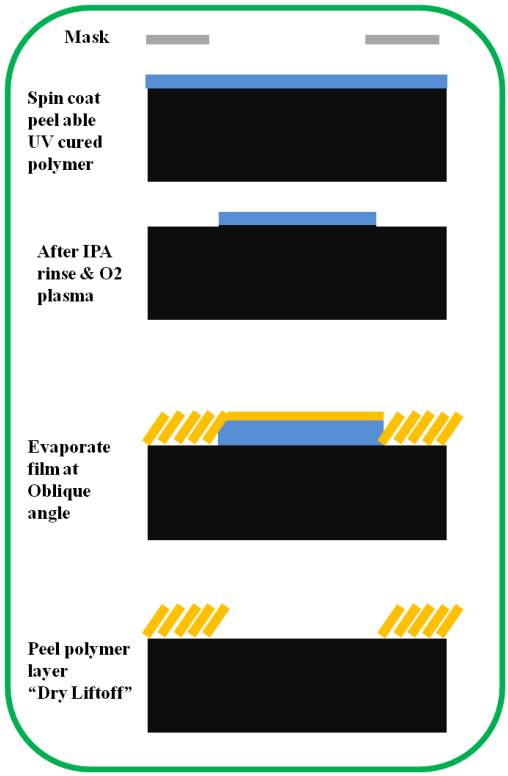

Figure 36 Dry liftoff lithography process

Parameters for spin speed versus ability to peel off the polymer film without breaking and cracking the polymer film were optimized prior to patterning polymer films. The polymer was spin coated on solvent cleaned prime grade silicon <100> wafer at 1000 rpm and allowed idle time for few minutes on a flat surface. The thickness of the cured cross-linked polymer was approximately 30 – 40 μm which was estimated using measurement calipers. Isopropyl alcohol is used as the solvent to rinse off the uncured polymer. Photo mask pattern printed on the mylar sheet were used as the photo mask for this study. A standard UV lamp was used for polymer exposure. In order to prevent the polymer on the substrate from sticking to the mask during UV exposure, proximity type exposure setup was used. The mask to substrate distance was approximately 0.5 mm. A short duration O_2 plasma treatment was conducted on the patterned polymer film to remove polymer residue from the areas where the polymer was rinsed away. Subsequently substrates were mounted on an OAD hinge fixture in the e-beam deposition chamber. SiO_2 evaporation pellets were 99.99 % purity and the chamber base pressure was $< 66.10^{-6}$ Pa ($\sim 0.5x10^{-6}$ Torr). The deposition angle at the sample was set between 84° to 86° for all samples. After the initial film conditioning ramp, the deposition rate was maintained at 0.3 nm s^{-1} using the Sigma SQC-310 thin film deposition controller for final film thickness set at 300 nm. All depositions were done using an MDC evap-4000 e-beam evaporator in a vacuum chamber designed by Torr International. Scanning electron microscope (SEM) images were acquired using a Hitachi S-4800 high resolution SEM for top views.

6.3 Results and discussion

Figure 37 shows the top view SEM imaging results. Vertical lines of different pitch were chosen as the mask pattern to initially prove the feasibility of dry liftoff process. SEM image shows 2 mm pitch lines with patterned SiO_2 in ~ 820 μm wide areas. Figure 37 (b) shows the high magnification physical structure of the SiO_2 STF.

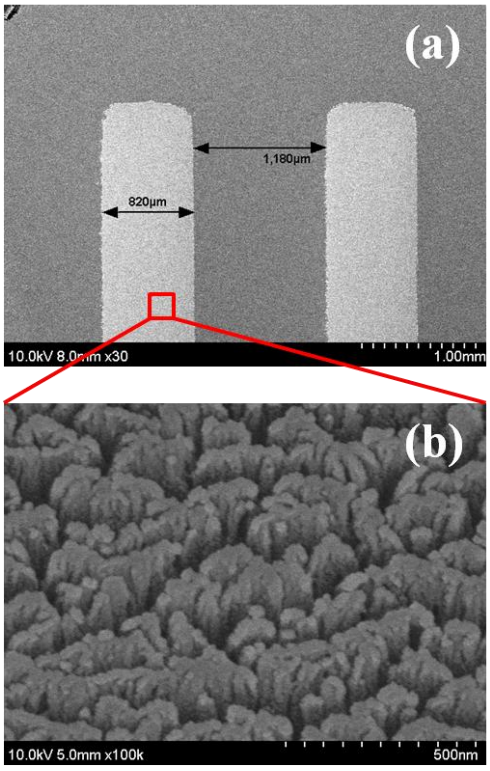

Figure 37 SEM image showing 2 mm pitch patterned SiO2 STF using dry-liftoff process

Figure 38 shows the polymer peeling process. It shows the mechanical strength of the polymer has allowed the cured polymer to be peeled off in one single layer. This is a key requirement, as the patterned feature size decreases with the decrease in polymer layer thickness. Even though the lift-off process shown here was done on small silicon

substrates, the process is scalable for patterning full size wafers. The polymer strength during peel off determines the feasibility of the process for wafer level patterning

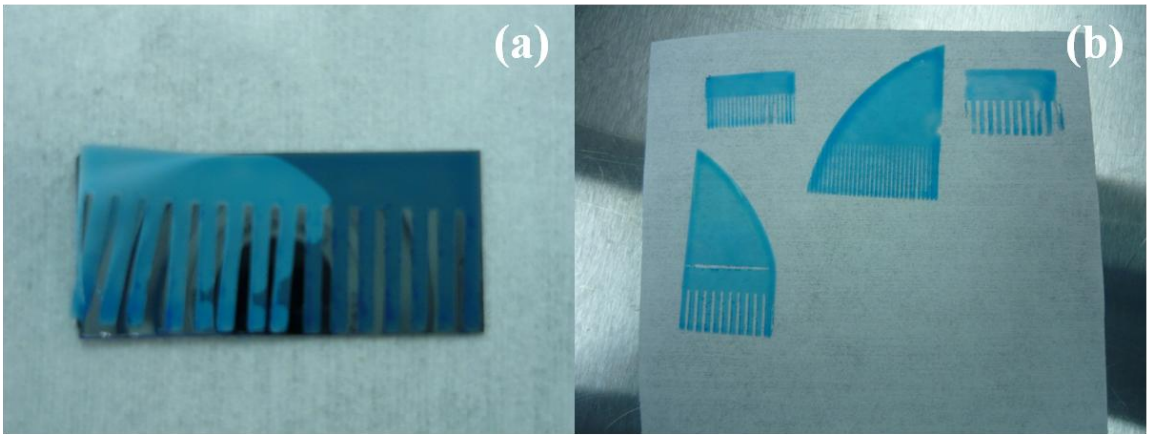

Figure 38 Photograph showing peelable polymer based dry-liftoff process

There are several issues and challenges in the current process which could be further refined for effective use of this technique. The two important issues are –

- Minimizing the polymer thickness layer
- Ability to use conventional mask aligner setup to pattern such thin films

The thickness of the polymer film is directly proportional to the viscosity of the polymer. Higher polymer thickness will result in increased dead zone as shown in Figure 39. But at the same time, thickness of the polymer should be high enough for it to be peel off cleanly in one piece without breaking the film. In this study, isopropyl alcohol was used as the diluting agent to decrease the viscosity. Since it is a volatile organic solvent, it may evaporate during the exposure and post exposure bake process. Ideally a polymer which is designed for low viscosity and high cross-linked strength would be suitable for this application. Figure 39 (b) shows the top view SEM image near the edge of the patterned nanorods thin films after polymer layer peel off. The edge appears jagged with white

residue in the vicinity. The presence of white residue is possibly due to some unknown compound during the exposure process. It appears to be uniform along the edge on several other samples that were fabricated. We believe the non-uniform jagged edge is a result of high proximity distance between the mask and the silicon substrate. Increased mask to substrate distance will results in diffraction causing non-uniform exposure especially on the edge of the mask pattern. One of the possible ways to improve the line fidelity would be to use conventional soft contact or hard contact type exposure setup in a mask aligner system.

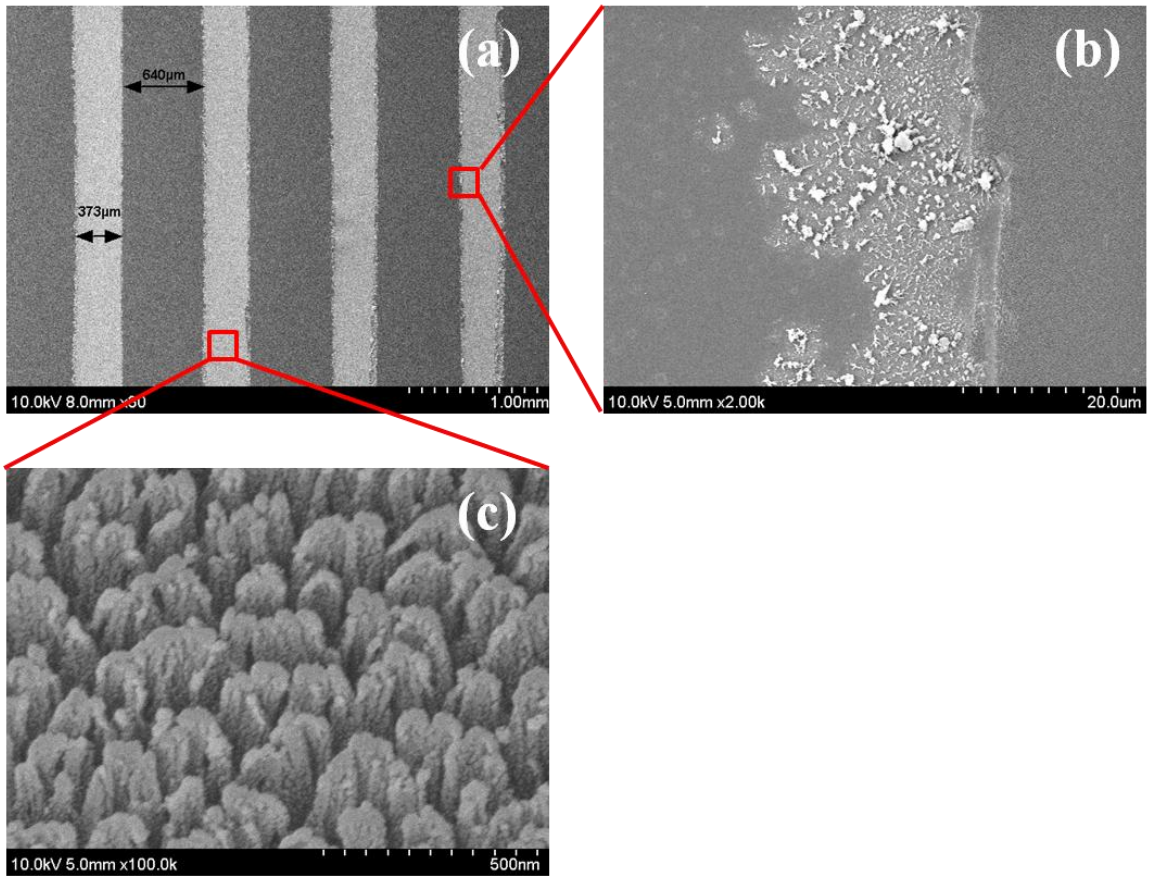

Figure 39 SEM image showing patterned SiO_2 STF using dry-liftoff process (a) 1 mm pitch patterned SiO_2 STF (b) Non-uniform edge with polymer IPA residue (c) High magnification top view SEM image of SiO_2 STF

Polydimethylsiloxane (PDMS) was the other potential polymer that was used for this process. PDMS is a popular polymer used mostly for microfluidic devices using the soft lithography technique. Using polar solvents like benzene or toluene, the thickness of the spin coated PDMS films can be reduced without compromising the mechanical properties. However the difficulty was in patterning PDMS thin films. PDMS dry etch recipes are discussed in literature; however our initial attempts to pattern and dry etch PDMS film were not successful.

Chapter 7 Summary and Conclusions

In this dissertation research we have investigated three aspects of nanorods thin films grown using oblique angle deposition technique namely, growth, SERS characterization and lithographic processing.

In Chapter 2, we have shown the influence of cryogenic substrate temperature on the growth of Ag nanorods thin films using oblique angle deposition. Our results indicate the formation of distinctly separate, high aspect ratio, individual Ag nanorods thin films on Si substrate, which is in contrast to the low aspect ratio and collapsed physical structure of nanorods grown at room temperature. The difference in morphology of Ag nanorods is attributed to the reduction in surface mobility of the incident atoms on the substrate surface. Analytical modeling behavior and the proposed theory was validated by studying the early nucleation stages during the thin films growth. Similar high aspect ratio nanocolumns have been observed in Cu and Au nanorods thin films. We believe these results indicate the potential to engineer nanostructure of thin films made from high conductivity, soft metals such as Ag, Cu and Au which has attractive optical and plasmonic properties.

In Chapter 3 and 4, we have shown the SERS characterization results of 100 K and 300 K grown AgNRs. Our results indicate significantly increased SERS signal intensity from 100 K AgNRs compared to 300 K AgNRs for the analyte molecules incubated in liquid and vapor phase. For AgNRs incubated with R6G at 10^{-6} M, 10^{-7} M, and 10^{-8} M the relative percentage increase in signal was estimated to be 91 %, 445 % and 441 % respectively. This increase in signal intensity is attributed mostly to the increased surface area and enhanced electromagnetic field in 100 K AgNRs. The electromagnetic field enhancement is possibly due to the observed poly dispersity of AgNRs post incubation in the aqueous solution. The uniformity and repeatability of the 100 K AgNRs have shown potential for these substrates for chemical and biological agent detection. Unlike colloidal AgNPs, 100 K grown AgNRs offers the versatility for effective use in liquid and vapor phase chemical sensing applications. Use of fluorescence spectrophotometer measurements for estimation of analyte molecules adsorbed on the AgNRs surface provides more accurate estimation for computing the SERS enhancement factor.

In Chapter 5 & 6, we have demonstrated the effectiveness of CO_2 critical point drying technique for preserving the physical structure of STF's after liquid exposure. When compared with evaporative drying at room temperature, CO_2 drying has shown a remarkable improvement in preserving the nanoscale structures of the film. Quantitative imaging analyses from SEM confirm these findings. Compared to previously suggested techniques, all of which require permanent alteration of the STF's physical structure, CPD could potentially enable lithographic processing of STF with minimal invasiveness. We believe wet-liftoff based lithographic patterning technique combined with CPD will

enable lithographic processing of nanorods thin films for device applications. Also shown is a dry-liftoff based alternative patterning technique for patterning nanorods thin films. We believe this technique requires further investigation for identifying another sacrificial polymer film which has high enough mechanical strength to sustain forces during peel off. The unusable patterned areas (dead zone) can be further minimized for lowering the polymer film thickness. PDMS and parylene-C thin films have the potential to meet these requirements and allow patterning much smaller feature size than shown in this research.

Chapter 8 Future work

- Investigate the difference in optical properties of Ag, Au, and Cu nanorods thin films grown at 100 K and 300 K substrate temperature. Such an investigation would reveal the promising applications of these nanostructured materials for plasmonic and meta materials research
- Even though, aluminum has high heat of formation (which means it reacts readily with the species present on the substrate), Al nanorods grown at 300 K substrate has shown poor columnar morphology. It would be insightful to observe the difference in columnar morphology when grown at 100 K substrate temperature
- The experimental setup used in this study for side by side growth of nanorods thin films at 100 K and 300 K didn't have a closed loop temperature control system. It would be insightful to control the cryogenic substrate temperature and investigate the evolution of nanorods thin films at substrate temperature between 100 K and 300 K.
- Design an experimental setup that measures the analyte concentration being deposited on the SERS substrate in vapor phase.

- Combine wet-liftoff process in combination with CO_2 CPD technique for patterning nanorods thin films. Investigation this subject further will enable the application of these thin films in existing micro/nano devices and could further enhance the functionality of such devices
- Investigate PDMS and Parylene-C based peelable polymer thin films for dry-liftoff based patterning of nanorods thin films.

Appendix A

A.1 Nanorods thin films on Flexible substrate (Polyimide)

Even though nanorods thin films research has been in existence for many years, not many real world applications has been able to adopt the novel properties exhibited by these films. Also most of the published literature on this subject has explored the growth, characterization, and applications on crystalline or polycrystalline rigid substrates. However some applications may require growth of nanorods thin films on flexible substrates. One of such application where we believe it might be beneficial to have nanorods grown on flexible substrates is orthopedic implants. Due to non symmetric and curved surface of many implants, uniform nanorods thin films growth on such surfaces could be a challenging task. Therefore for such substrates, growth on flexible substrates could be beneficial. Flexible substrates with nanorods thin films could hypothetically cover the implant surface area. In this preliminary study, we investigated the growth of Cr nanorods thin films on flexible substrate. Polyimide (Kapton) adhesive tape was chosen the candidate for this preliminary investigation. Kapton adhesive tape was attached to silicon substrate prior to deposition. Concurrently Cr nanorods thin films were also grown on silicon substrate. Figure shows the top view SEM images showing Cr nanorods thin films on silicon and Kapton adhesive tape. Cr nanorods thin films structure on Kapton tape is very identical to the structure of film on silicon substrate.

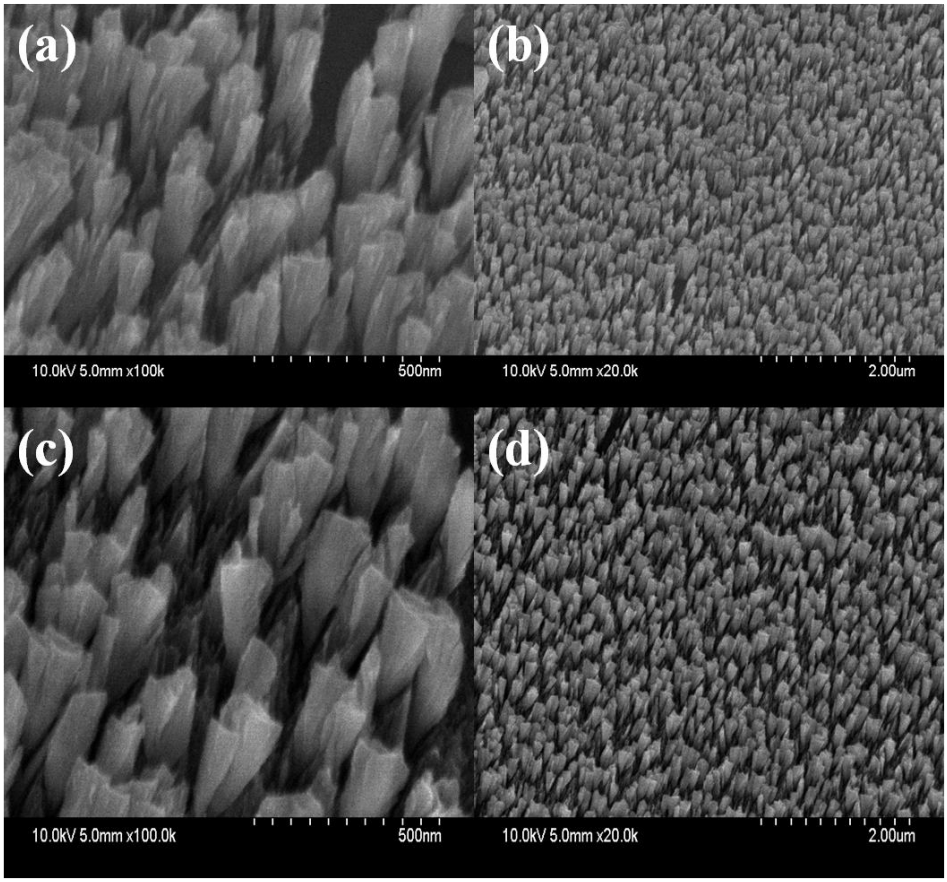
(a)
10.0kV 5.0mm x100k
500nm
(b)
10.0kV 5.0mm x20.0k
2.00um
(c)
10.0kV 5.0mm x100.0k
500nm
(d)
10.0kV 5.0mm x20.0k
2.00um

A.2 Nanorods thin films on 1-D gratings structure

Oblique angle deposition (OAD) technique has shown the ability to fabricate nano structured thin films (STF's) with novel properties for various applications. However some applications like photonic crystals or photonic band gap materials have the need for periodic nucleation. In this short study, we discuss the use of deep UV interference lithography for designing sub-micron one dimensional (1-D) and two dimensional (2-D) seed layers prior to the growth of STF's on seed layers. Ability to design and pattern seed layers on wafer scale is an important attribute in adoption of such methods for commercial application and deep UV lithography has this attribute. Conventionally most published literature on periodic nucleation prior to STF's growth has shown several different expensive and less scalable lithographic methods. Some of the commonly used methods for lithographic patterning of seeds on the substrate are interferometric, e-beam lithography, X-ray lithography, nano-imprint, and colloidal sphere self assembly technique. E-beam lithography with PMMA resist is one of the common methods. However it is an expensive and slow process which is why it has not been accepted for high volume wafer scale operations.

Figure shows the sub-micron 1-D gratings structure used as substrate for deposition of SiO_2 and Cr nanorods thin films. Spin coated PMMA based UVN-30 photoresist was exposed using Lloyd's mirror based interference lithography set up. Figure (a), (b) and (c) shows the SiO_2 nanorods thin films on the grating structure

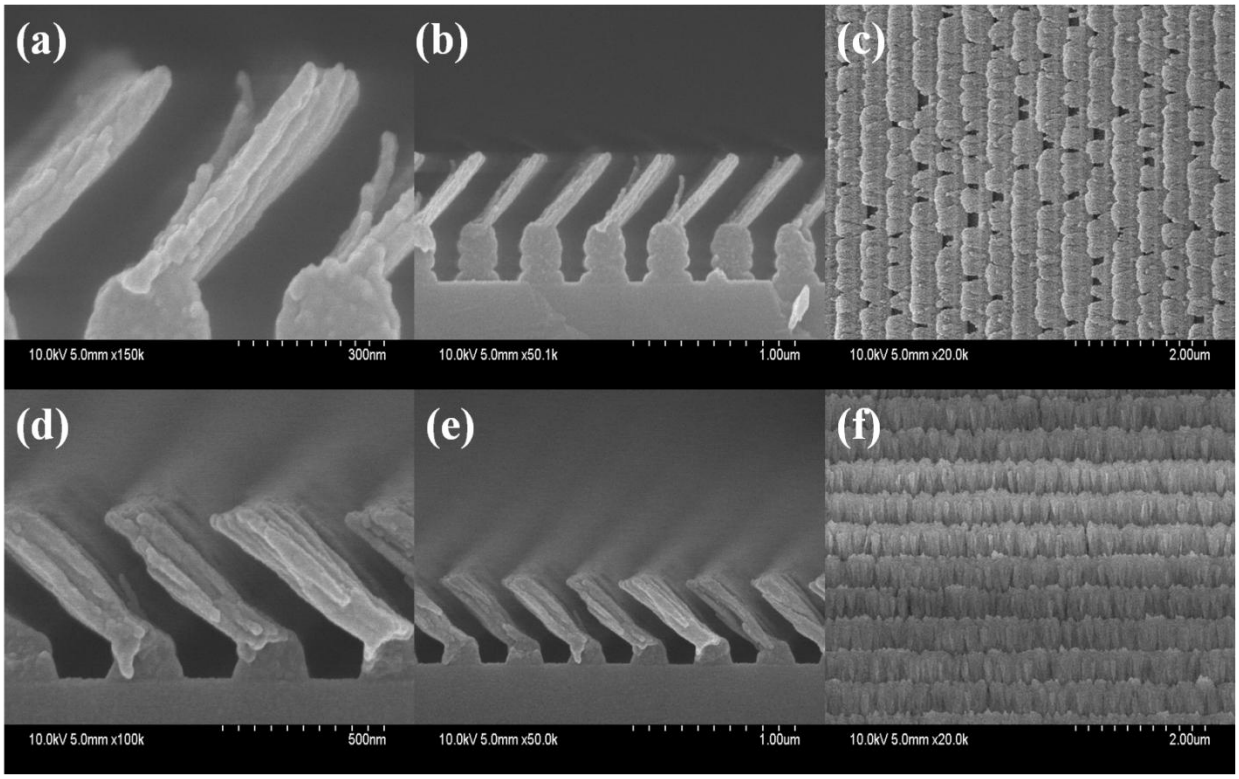
(a)
10.0kV 5.0mm x150k
300nm
(b)
10.0kV 5.0mm x50.1k
1.00um
(c)
10.0kV 5.0mm x20.0k
2.00um
(d)
10.0kV 5.0mm x100k
500nm
(e)
10.0kV 5.0mm x50.0k
1.00um
(f)
10.0kV 5.0mm x20.0k
2.00um

A.3 MEMS Cantilever based volatile organic compound sensing using SiO_2 nanorods thin films

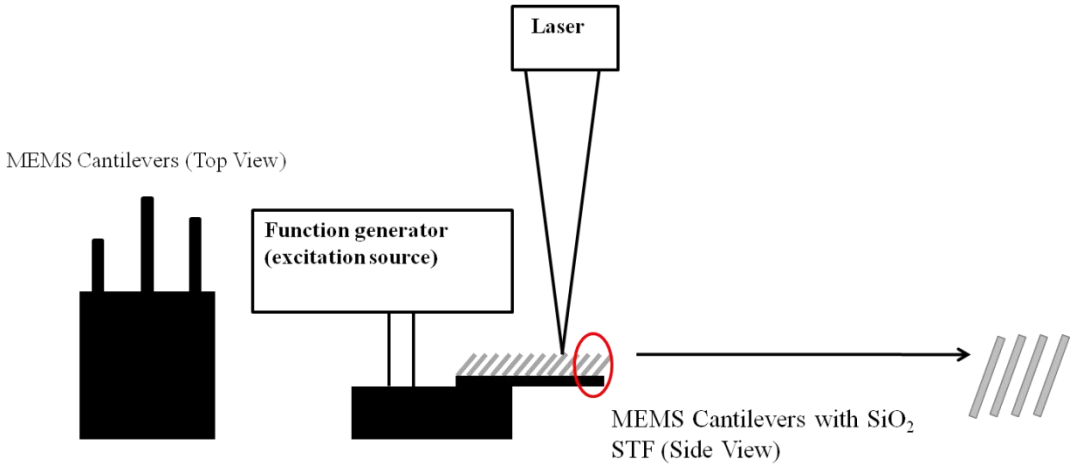

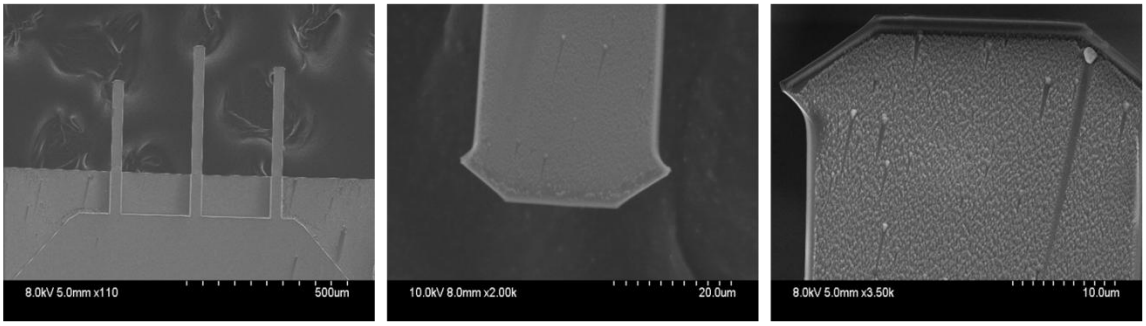

The aim of this project is to use SiO_2 nanorods thin films in conjunction with MEMS based cantilever setup for detecting volatile organic compounds in vapor phase. Nanorods thin film is functionalized with silane vapor. Functionalized silane provides a platform for organic vapor molecules to bind and attach on the thin films surface. Change in resonance frequency of the cantilever is measured using the optical setup. Resonance frequency is inversely proportional to the amount of organic molecules adsorbed on the thin films surface. Figure shows the MEMS cantilevers with SiO_2 nanorods thin films and the measurement setup schematic.

References

[1] K. Robbie and M. Brett, "Sculptured thin films and glancing angle deposition: Growth mechanics and applications," *Journal of Vacuum Science & Technology A: Vacuum, Surfaces, and Films*, vol. 15, pp. 1460-1465, 1997.

[2] A. Dirks and H. Leamy, "Columnar microstructure in vapor-deposited thin films," *Thin Solid Films,* vol. 47, pp. 219-233, 1977.

[3] J. Steele and M. Brett, "Nanostructure engineering in porous columnar thin films: recent advances," *Journal of Material Science: Materials in Electronics*, vol. 18, pp. 367-379, 2007.

[4] T. Hashimoto, K. Okamoto, H. Fujiwara, K. Itoh, K. Hara and M. Kamiya, "Columnar structure of obliquely deposited cobalt films prepared at low substrate temperatures," *Thin Solid Films,* vol. 192, pp. 335-342, 1990.

[5] M. Hawkeye and M. Brett, "Glancing angle deposition: Fabrication, properties, and applications of micro-and nanostructured thin films," *Journal of Vacuum Science & Technology A: Vacuum, Surfaces, and Films,* vol. 25, pp. 1317-1335, 2007.

[6] H. Konig and G. Helwig, "The Structure of Obliquely Evaporated Films and Their Influence on the Formation of Sub-Microscopic Surface Irregularities," *Optik,* vol. 6, pp. 111, 1950.

[7] S. Mukherjee and D. Gall, "Anomalous scaling during glancing angle deposition," *Applied Physics Letters*, vol. 95, pp. 173106, 2009.

[8] C. Zhou and D. Gall, "Competitive growth of Ta nanopillars during glancing angle deposition: Effect of surface diffusion," *Journal of Vacuum Science & Technology A: Vacuum, Surfaces, and Films,* vol. 25, pp. 312-318, 2007.

[9] D. Vick, Y. Tsui, M. Brett and R. Fedosejevs, "Production of porous carbon thin films by pulsed laser deposition," *Thin Solid Films,* vol. 350, pp. 49-52, 1999.

[10] D. Schmidt, B. Booso, T. Hofmann, E. Schubert, A. Sarangan and M. Schubert, "Generalized ellipsometry for monoclinic absorbing materials: determination of optical constants of Cr columnar thin films," *Optics Letters,* vol. 34, pp. 992-994, 2009.

[11] D. Schmidt, B. Booso, T. Hofmann, E. Schubert, A. Sarangan and M. Schubert, "Monoclinic optical constants, birefringence, and dichroism of slanted titanium nanocolumns determined by generalized ellipsometry," *Applied Physics Letters,* vol. 94, pp. 011914-011914-3, 2009.

[12] K. Itoh, F. Ichikawa, Y. Takahashi, K. Tsutsumi, Y. Noguchi, K. Okamoto, T. Uchiyama and I. Iguchi, "Columnar grain structure in cobalt films evaporated obliquely at low substrate temperatures," *Japanese Journal of Applied Physics Part 1-Regular Papers Brief Communications & Review Papers,* vol. 45, pp. 2534-2538, 2006.

[13] B. Dick, M. Brett, T. Smy, M. Freeman, M. Malac and R. Egerton, "Periodic magnetic microstructures by glancing angle deposition," *Journal of Vacuum Science & Technology A: Vacuum, Surfaces, and Films,* vol. 18, pp. 1838, 2000.

[14] D. Gish, M. Summers and M. Brett, "Morphology of periodic nanostructures for photonic crystals grown by glancing angle deposition," *Photonics and Nanostructures-Fundamentals and Applications,* vol. 4, pp. 23-29, 2006.

[15] M. Jensen and M. Brett, "Periodically structured glancing angle deposition thin films," *IEEE Transactions on Nanotechnology,* vol. 4, pp. 269-277, 2005.

[16] M. Jensen and M. Brett, "Porosity engineering in glancing angle deposition thin films," *Applied Physics A-Materials Science & Processing,* vol. 80, pp. 763-768, 2005.

[17] M. Malac, R. Egerton, M. Brett and B. Dick, "Fabrication of submicrometer regular arrays of pillars and helices," *Journal of Vacuum Science & Technology B: Microelectronics and Nanometer Structures,* vol. 17, pp. 2671, 1999.

[18] T. Karabacak, G. C. Wang and T. M. Lu, "Physical self-assembly and the nucleation of three-dimensional nanostructures by oblique angle deposition," *Journal of Vacuum Science & Technology A: Vacuum, Surfaces, and Films,* vol. 22, pp. 1778-1784, 2004.

[19] M. Fleischmann, P. Hendra and A. McQuillan, "Raman spectra of pyridine adsorbed at a silver electrode," *Chemical Physics Letters,* vol. 26, pp. 163-166, 1974.

[20] D. Jeanmaire and R. Van Duyne, "Surface Raman spectroelectrochemistry: Part I. Heterocyclic, aromatic, and aliphatic amines adsorbed on the anodized silver electrode," *Journal of Electroanalytical Chemistry and Interfacial Electrochemistry*, vol. 84, pp. 1-20, 1977.

[21] S. Brueck, "Optical and interferometric lithography-nanotechnology enablers," *Proceedings of IEEE,* vol. 93, pp. 1704-1721, 2005.

[22] B. Chaney, S. Shanmukh, R. A. Dluhy and Y. P. Zhao, "Aligned silver nanorod arrays produce high sensitivity surface-enhanced Raman spectroscopy substrates," *Applied Physics Letters.,* vol. 87, pp. 031908, 2005.

[23] Y. Liu, H. Chu and Y. Zhao, "Silver nanorod array substrates fabricated by oblique angle deposition: morphological, optical, and SERS characterizations," *Journal of Physical Chemistry C,* vol. 114, pp. 8176-8183, 2010.

[24] T. Karabacak, J. DeLuca, P. Wang, G. Ten Eyck, D. Ye, G. Wang and T. Lu, "Low temperature melting of copper nanorod arrays," *Journal of Applied Physics.,* vol. 99, pp. 064304, 2006.

[25] S. Kesapragada and D. Gall, "Anisotropic broadening of Cu nanorods during glancing angle deposition," *Applied Physics Letters,* vol. 89, pp. 203121-203121-3, 2006.

[26] B. Movchan and A. Demchishin, "Study of the structure and properties of thick vacuum condensates of nickel, titanium, tungsten, aluminium oxide and zirconium dioxide," *Physics of Metals and Metallography, (Engl. Transl.)* vol. 28, pp.83 , 1969.

[27] R. Messier, A. Giri and R. Roy, "Revised structure zone model for thin film physical structure," *Journal of Vacuum Science & Technology A: Vacuum, Surfaces, and Films,* vol. 2, pp. 500-503, 1984.

[28] H. Savaloni and M. Shahraki, "A computer model for the growth of thin films in a structure zone model," *Nanotechnology,* vol. 15, pp. 311, 2004.

[29] J. van De Waterbeemd and G. Van Oosterhout, "Effect of the mobility of metal atoms on the structure of thin films deposited at oblique incidence," *Philips Res.Rep,* vol. 22, pp. 375-387, 1967.

[30] K. Biggs, J. Camden, J. Anker and R. Van Duyne, "Surface-Enhanced Raman Spectroscopy of Benzenethiol Adsorbed from the Gas Phase onto Silver Film over Nanosphere Surfaces: Determination of the Sticking Probability and Detection Limit Time†," *Journal of Physical Chemistry A,* vol. 113, pp. 4581-4586, 2009.

[31] H. Chu, Y. Huang and Y. Zhao, "Silver nanorod arrays as a surface-enhanced Raman scattering substrate for foodborne pathogenic bacteria detection," *Applied Spectroscopy,* vol. 62, pp. 922-931, 2008.

[32] H. Chu, Y. Liu, Y. Huang and Y. Zhao, "A high sensitive fiber SERS probe based on silver nanorod arrays," *Optics Express,* vol. 15, pp. 12230-12239, 2007.

[33] J. Driskell, O. Primera-Pedrozo, R. A. Dluhy, Y. Zhao and R. A. Tripp, "Quantitative surface-enhanced raman spectroscopy based analysis of microRNA mixtures," *Applied Spectroscopy,* vol. 63, pp. 1107-1114, 2009.

[34] J. Driskell, S. Shanmukh, Y. Liu, S. Hennigan, L. Jones, Y. Zhao, R. Dluhy, D. Krause and R. Tripp, "Infectious agent detection with SERS-active silver nanorod arrays prepared by oblique angle deposition," *Sensors Journal, IEEE,* vol. 8, pp. 863-870, 2008.

[35] J. Driskell, Y. Zhu, C. Kirkwood, Y. Zhao, R. Dluhy and R. Tripp, "Rapid and sensitive detection of rotavirus molecular signatures using surface enhanced Raman spectroscopy," *PloS One,* vol. 5, pp. e10222, 2010.

[36] J. Driskell, A. Seto, L. Jones, S. Jokela, R. Dluhy, Y. Zhao and R. Tripp, "Rapid microRNA (miRNA) detection and classification via surface-enhanced Raman spectroscopy (SERS)," *Biosensors and Bioelectronics,* vol. 24, pp. 917-922, 2008.

[37] X. Du, H. Chu, Y. Huang and Y. Zhao, "Qualitative and Quantitative Determination of Melamine by Surface-Enhanced Raman Spectroscopy Using Silver Nanorod Array Substrates," *Applied Spectroscopy,* vol. 64, pp. 781-785, 2010.

[38] J. Fu, Z. Cao and L. Yobas, "Localized oblique-angle deposition: Ag nanorods on microstructured surfaces and their SERS characteristics," *Nanotechnology,* vol. 22, pp. 505302, 2011.

[39] C. Leverette, S. Jacobs, S. Shanmukh, S. Chaney, R. Dluhy and Y. Zhao, "Aligned silver nanorod arrays as substrates for surface-enhanced infrared absorption spectroscopy," *Applied Spectroscopy,* vol. 60, pp. 906-913, 2006.

[40] Y. Liu, Z. Zhang, R. Dluhy and Y. Zhao, "The SERS response of semiordered Ag nanorod arrays fabricated by template oblique angle deposition," *Journal of Raman Spectroscopy,* vol. 41, pp. 1112-1118, 2010.

[41] K. Norrod, L. Sudnik, D. Rousell and K. Rowlen, "Quantitative comparison of five SERS substrates: sensitivity and limit of detection," *Applied. Spectroscopy,* vol. 51, pp. 994-1001, 1997.

[42] S. Shanmukh, Les Jones, J. Driskell, Y. Zhao, R. Dluhy and R. Tripp, "Rapid and sensitive detection of respiratory virus molecular signatures using a silver nanorod array SERS substrate," *Nano Letters,* vol. 6, pp. 2630-2636, 2006.

[43] R. Tripp, R. Dluhy and Y. Zhao, "Novel nanostructures for SERS biosensing," *Nano Today,* vol. 3, pp. 31-37, 2008.

[44] Q. Zhou, Z. Li, Y. Yang and Z. Zhang, "Arrays of aligned, single crystalline silver nanorods for trace amount detection," *Journal of Physics D,* vol. 41, pp. 152007, 2008.

[45] Y. Zhao, S. H. Li, S. Chaney, S. Shanmukh, J. Fan, R. Dluhy and W. Kisaalita, "Designing nanostructures for sensor applications," *Journal of Electronic Materials,* vol. 35, pp. 846-851, 2006.

[46] J. Steele, J. Gospodyn, J. Sit and M. Brett, "Impact of morphology on high-speed humidity sensor performance," *Sensors Journal, IEEE,* vol. 6, pp. 24-27, 2006.

[47] M. Gasda, G. Eisman and D. Gall, "Nanorod PEM Fuel Cell Cathodes with Controlled Porosity," *Journal of Electrochemical Society,* vol. 157, pp. B437, 2010.

[48] J. Fan, J. Fu, A. Collins and Y. Zhao, "The effect of the shape of nanorod arrays on the nanocarpet effect," *Nanotechnology,* vol. 19, pp. 045713, 2008.

[49] Y. Zhao and J. Fan, "Clusters of bundled nanorods in nanocarpet effect," *Applied Physics Letters,* vol. 88, pp. 103123-103123-3, 2006.

[50] J. Fan and Y. Zhao, "Nanocarpet effect induced superhydrophobicity," *Langmuir,* vol. 26, pp. 8245-8250, 2010.

[51] J. G. Fan, D. Dyer, G. Zhang and Y. Zhao, "Nanocarpet effect: Pattern formation during the wetting of vertically aligned nanorod arrays," *Nano Letters,* vol. 4, pp. 2133-2138, 2004.

[52] J. Fan and Y. Zhao, "Characterization of watermarks formed in nano-carpet effect," *Langmuir,* vol. 22, pp. 3662-3671, 2006.

[53] P. Shah, X. Niu and A. Sarangan, “Effect of substrate temperature on the growth of silver nanorod thin films using oblique angle deposition” *(after first revision), Journal of Vacuum Science & Technology B,*2012

[54] P. Shah, X. Niu and A. Sarangan, “Effect of cryogenic substrate temperature on the growth of Ag and Cu nanostructured optical metamaterials” *Symposium of Photonics and Optoelectronics 2012, China,* May 2012

[55] P. Shah, A. Stahler, A. Sarangan and I. Pavel, “Comparative SERS response of silver nanorods thin films fabricated at room and cryogenic temperature with Rhodamine 6G molecules” *(submitted) Journal of American Chemical Society Communications,* June 2012

[56] P. Shah, X. Niu, D. Ju and A. Sarangan, “Vapor phase sensing using metal nanorods thin films grown using oblique angle deposition” *(to be submitted), Journal of Vacuum Science & Technology B,*2012

[57] P. Shah, Z. Wu and A. Sarangan, “Effect of CO_2 critical point drying on nanostructured thin films after liquids exposure” *(accepted) Thin Solid Films,* Nov 2011

[58] C. Zhou, H. Li and D. Gall, "Multi-component nanostructure design by atomic shadowing," *Thin Solid Films,* vol. 517, pp. 1214-1218, 2008.

[59] L. Abelmann and C. Lodder, "Oblique evaporation and surface diffusion," *Thin Solid Films,* vol. 305, pp. 1-21, 1997.

[60] S. Mukherjee, C. M. Zhou and D. Gall, "Temperature-induced chaos during nanorod growth by physical vapor deposition," *Journal of Applied Physics,* vol. 105, 2009.

[61] D. Deniz and R. J. Lad, "Temperature threshold for nanorod structuring of metal and oxide films grown by glancing angle deposition," *Journal of Vacuum Science & Technology A: Vacuum, Surfaces, and Films*, vol. 29, pp. 011020, 2011.

[62] R. Messier, V. C. Venugopal and P. D. Sunal, "Origin and evolution of sculptured thin films," *Journal of Vacuum Science & Technology a*, vol. 18, pp. 1538-1545, 2000.

[63] J. A.Thornton, "High-Rate Thick-Film Growth," *Annual Review of Materials Science*, vol. 7, pp. 239-260, 1977.

[64] K. Hara, M. Kamiya, T. Hashimoto, K. Okamoto and H. Fujiwara, "Oblique-incidence anisotropy of the iron films evaporated at low substrate temperatures," *Journal of Magnetism and Magnetic Materials*, vol. 73, pp. 161-166, 1988.

[65] C. L. Liu *et al.*, "EAM study of surface self-diffusion of single adatoms of fcc metals Ni, Cu, Al, Ag, Au, Pd, and Pt," *Surface Science*. 253 (1-3), 334 (1991).

[66] G. Antczak, "Kinetics of atom rebounding in surface self-diffusion," *Physics Review B* 74 (15), 153406 (2006).

[67] A. Gorshkov, "Empirical relation for the activation energy of diffusion in elemental substances," *Inorganic Materials*, vol. 36, pp. 22-23, 2000.

[68] M. Burger, "Surface diffusion including adatoms," *Communications in Mathematical Sciences*, vol. 4, pp. 1-51, 2006.

[69] D. M. Mattox, *Handbook of physical vapor deposition (PVD) processing*, 2nd ed. (William Andrew, Oxford, UK, 2010), pp. 746.

[70] D. M. Mattox, "Thin film metallization of oxides in microelectronics," *Thin Solid Films* 18 (2), 173-186 (1973).

[71] R. Pretorius, J. Harris and M. Nicolet, "Reaction of thin metal films with SiO2 substrates," *Solid-State Electronics,* vol. 21, pp. 667-675, 1978.

[72] J. Baglin, "Thin film adhesion: new possibilities for interface engineering," *Materials Science and Engineering: B,* vol. 1, pp. 1-7, 1988.

[73] Ujjal Kumar Sur, Surface-enhanced Raman spectroscopy: Recent advancement of Raman spectroscopy, *Resonace* pp.1 - 11, 2010.

[74] J. A. Creighton, C. G. Blatchford and M. G. Albrecht, "Plasma resonance enhancement of Raman scattering by pyridine adsorbed on silver or gold sol particles of size comparable to the excitation wavelength," *Journal of Chemical Society, Faraday Transactions.2,* vol. 75, pp. 790-798, 1979.

[75] S. Xu, X. Ju, W. Xu, X. Li, L. Wang, Y. Bai, B. Zhao and Y. Ozaki, "Immunoassay using probe-labeling immunogold nanoparticles with silver staining enhancement *via* surface-enhanced Raman scattering" *Analyst* vol. 129, pp. 63–68, 2004.

[76] K. Kneipp, Y. Wang, H. Kneipp, L. T. Perelman, I. Itzkan, R. R. Dasari and M. S. Feld, "Single molecule detection using surface-enhanced Raman scattering (SERS)," *Physics Review Letters,* vol. 78, pp. 1667-1670, 1997.

[77] E. Fazio, F. Neri, C. D'Andrea, P. Ossi, N. Santo and S. Trusso, "SERS activity of pulsed laser ablated silver thin films with controlled nanostructure," *Journal of Raman Spectroscopy,* vol. 42, pp. 1298-1304, 2011.

[78] Y. Zhu, R. Dluhy and Y. Zhao, "Development of silver nanorod array based fiber optic probes for SERS detection", *Sensors and Acutators B: Chemical*, vol. 157, 1, pp. 42-50, 2011.

[79] I. Pavel, K. Alnajjar, J. Monahan,A. Stahler, N. Hunter, K. Weaver, J. Baker, A. Meyerhoefer, D. Dolson, “Estimating the analytical and surface enhancement factors in Surface enhanced Raman scattering (SERS): A novel physical chemistry and nanotechnology laboratory experiment” *Journal of Chemical Education*, vol. 89, pp. 286 – 290, 2012.

[80] Y. Wu, T. Livneh, Y. X. Zhang, G. Cheng, J. Wang, J. Tang, M. Moskovits and G. D. Stucky, "Templated synthesis of highly ordered mesostructured nanowires and nanowire arrays," *Nano Letters,* vol. 4, pp. 2337-2342, 2004.

[81] N. Felidj, J. Aubard, G. Levi, J. Krenn, A. Hohenau, G. Schider, A. Leitner and F. Aussenegg, "Optimized surface-enhanced Raman scattering on gold nanoparticle arrays," *Applied Physics Letters,* vol. 82, pp. 3095, 2003.

[82] V. L. Schlegel and T. M. Cotton, "Silver-island films as substrates for enhanced Raman scattering: effect of deposition rate on intensity," *Analytical Chemistry*, vol. 63, pp. 241-247, 1991.

[83] M. D. Abràmoff, P. J. Magalhães and S. J. Ram, "Image processing with ImageJ," *Biophotonics International*, vol. 11, pp. 36-42, 2004.

[84] The Mathworks, Inc, Natick, MA, USA

[85] S. H. Ciou, Y. W. Cao, H. C. Huang, D. Y. Su and C. L. Huang, "SERS enhancement factors studies of silver nanoprism and spherical nanoparticle colloids in the presence of Bromide ions," *Journal of Physical Chemistry C*, vol. 113, pp. 9520-9525, 2009.

[86] P. A. Smith, D. Koch, G. L. Hook, R. P. Erickson, C. R. Jackson Lepage, H. D. M. Wyatt, G. Betsinger and B. A. Eckenrode, "Detection of gas-phase chemical

warfare agents using field-portable gas chromatography–mass spectrometry systems: instrument and sampling strategy considerations," *TrAC Trends in Analytical Chemistry,* vol. 23, pp. 296-306, 2004.

[87] D. Collins and M. Lee, "Developments in ion mobility spectrometry-mass spectrometry," *Analytical and Bioanalytical Chemistry,* vol. 372, pp. 66-73, 2002.

[88] D. A. Stuart, K. B. Biggs and R. P. Van Duyne, "Surface-enhanced Raman spectroscopy of half-mustard agent," *Analyst,* vol. 131, pp. 568-572, 2006.

[89] K. Kuwahara and H. Hirota, "Resistivity Anisotropy in Oblique-Incidence Evaporated-Films," *Japanese Journal of Applied Physics,* vol. 13, pp. 1093-1095, 1974.

[90] F. Liu, C. Yu, L. Shen, J. Barnard and G. Mankey, "The magnetic properties of cobalt films produced by glancing angle deposition," *Magnetics, IEEE Transactions,* vol. 36, pp. 2939-2941, 2002.

[91] M. Kupsta, M Taschuk, M Brett and J Sit, *Thin Solid Films* 519, (2011) 1923

[92] J. K. Kwan and J. C. Sit, "The use of ion-milling to control clustering of nanostructured, columnar thin films," *Nanotechnology*, vol. 21, pp. 295301, 2010.

[93] K. K. S. Lau, J. Bico, K. B. K. Teo, M. Chhowalla, G. A. J. Amaratunga, W. I. Milne, G. H. McKinley and K. K. Gleason, "Superhydrophobic carbon nanotube forests," *Nano Letters,* vol. 3, pp. 1701-1705, 2003.

[94] S. Tsoi, E. Fok, J. G. C. Veinot and J. C. Sit, "Vapor-Phase Chemical Functionalization of High Porosity, Nanostructured Thin Films," *International Journal of Nanoscience,* vol. 6, pp. 103-108, 2007.

[95] I. H. Jafri, H. Busta and S. T. Walsh, "Critical point drying and cleaning for MEMS technology," in *Proceedings of SPIE*, 1999, pp. 51.

[96] I. Pavel, E. McCarney, A. Elkhaled, A. Morrill, K. Plaxco and M. Moskovits, "Label-free SERS detection of small proteins modified to act as bifunctional linkers," *Journal of Physical Chemistry C*, vol. 112, pp. 4880-4883, 2008.

[97] R. Gupta and W. Weimer, "High enhancement factor gold films for surface enhanced Raman spectroscopy," *Chemical Physics Letters*, vol. 374, pp. 302-306, 2003.

[98] C. P. Tan and H. G. Craighead, "Surface engineering and patterning using parylene for biological applications," *Materials*, vol. 3, pp. 1803-1832, 2010.

[99] C. P. Tan, B. R. Seo, D. J. Brooks, E. M. Chandler, H. G. Craighead and C. Fischbach, "Parylene peel-off arrays to probe the role of cell–cell interactions in tumour angiogenesis," *Integrative Biology*, vol. 1, pp. 587-594, 2009.

[100] J. M. Moran-Mirabal, C. P. Tan, R. N. Orth, E. O. Williams, H. G. Craighead and D. M. Lin, "Controlling microarray spot morphology with polymer liftoff arrays," *Analytical Chemistry*, vol. 79, pp. 1109-1114, 2007.

[101] Y. P. Zhao, S. Chaney and Z. Y. Zhang, "Absorbance spectra of aligned Ag nanorod arrays prepared by oblique angle deposition," *Journal of Applied Physics*, vol. 100, pp. 063527, 2006.

[102] A. Lakhtakia and Y. J. Jen, "Simple optical technology for negative real refractive index," *Proceedings of SPIE*.

[103] J. G. Fan and Y. P. Zhao, "Direct deposition of aligned nanorod array onto cylindrical objects," *Journal of Vacuum Science & Technology B: Microelectronics and Nanometer Structures*, vol. 23, pp. 947, 2005.

[104] J. D. Driskell, S. Shanmukh, Y. Liu, S. B. Chaney, X. J. Tang, Y. P. Zhao and R. A. Dluhy, "The use of aligned silver nanorod arrays prepared by oblique angle deposition as surface enhanced Raman scattering substrates," *Journal of Physical Chemistry C*, vol. 112, pp. 895-901, 2008.

[105] K. R. Beavers, N. E. Marotta and L. A. Bottomley, "Thermal Stability of Silver Nanorod Arrays," *Chemistry of Materials*, vol. 22, pp. 2184-2189, 2010.